Nanophotonics for Tailoring Light-Matter Interaction

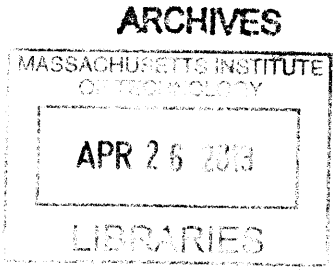

by

Wenjun Qiu

Submitted to the Department of Physics
in partial fulfillment of the requirements for the degree of

Doctor of Philosophy

at the

MASSACHUSETTS INSTITUTE OF TECHNOLOGY

February 2013

Author .....
Department of Physics
October 4th, 2012

Certified by .....
Marin Soljačić
Professor of Physics and MacArthur Fellow
Thesis Supervisor

Accepted by .....
Professor John W. Belcher
Chairman, Associate Department Head for Education

Nanophotonics for Tailoring Light-Matter Interaction

by

Wenjun Qiu

Submitted to the Department of Physics
on October 4th, 2012, in partial fulfillment of the
requirements for the degree of
Doctor of Philosophy

Abstract

In this thesis, we will theoretically explore three nanophotonics phenomena which enable strong light-matter interaction.

The first phenomenon is plasmonic resonance, where the surface plasmon mode at metal and dielectric boundaries significantly enhances the optical response of nanoparticles. We propose an optimization-based theoretical approach to tailor the optical response of silver/silica multilayer nanospheres over the visible spectrum. We show that the structure that provides the largest cross-section per volume/mass, averaged over a wide frequency range, is the silver coated silica sphere. We also show how properly chosen mixture of several species of different nanospheres can have an even larger minimal cross-section per volume/mass over the entire visible spectrum.

The second phenomenon is photonic chiral edge state, where the breaking of time-reversal symmetry forces light to travel in only one direction. Based on the directional coupling between one-way waveguide and conventional two-waveguide, we propose a new type of optical circulators, which has the potential for simultaneous broadband operation and small device footprint.

The third phenomenon is Stimulated Brillouin Scattering (SBS), where photon and phonon are coupled through optical forces such as electrostriction force and radiation pressure. We develop a general method of calculating SBS gain via the overlap integral between optical and elastic modes. Applying this method to a rectangular waveguide, we demonstrate that the distribution of optical force and elastic modal profile jointly determine the magnitude and scaling of SBS gains. Applying this method to a periodic waveguide, we demonstrate that SBS gain can be further enhanced in the slow light regime. Based on this framework, we theoretically characterize a novel class of hybrid photon-phonon waveguides. Our analysis reveals that photon-phonon coupling via SBS can be directed and tailored over an exceptionally wide frequency range, enabling a host of chip-scale filtering, delay, and signal processing schemes.

Thesis Supervisor: Marin Soljačić
Title: Professor of Physics and MacArthur Fellow

Acknowledgments

I would like to express my deepest gratitude to my thesis supervisor Prof. Marin Soljačić for his invaluable guidance, consistent support and considerable patience throughout the past four years. It has always been a privilege and a pleasure to learn from Marin's insightful intuition as a theorist and creative ideas as an inventor. I would also like to thank Marin for his sincere care of my personal life and tremendous help on my career development.

I am deeply grateful to Prof. Zheng Wang at UT Austin. I have been working with Zheng on many exciting projects since I joined Marin's group. Zheng offered me tremendous help in so many aspects, from project initiations to hands-on simulations, from writing papers to career development.

I would like to thank Prof. John Joannopoulos for his insightful advice and inspiring discussions. I would also like to thank Prof. Steven Johnson for his great help in computational issues and wonderful instructions in photonic crystals and numerical methods. In addition, I would like to thank Prof. Vladan Vuletić for serving on my thesis committee and Prof. Xiao-Gang Wen for advising my academic progress.

I would like to thank Prof. Peter Rakich at Yale and Dr. Heedeuk Shin at Sandia for providing me the opportunity to join in the cutting edge research of traveling wave optomechanics. I would also like to thank Dr. Brendan DeLacy in Edgewood Chemical Biological Center for his great effort in our collaboration on obscurant nanoparticles.

I wish to express my warm thanks to all the members in Marin's group for their sincere friendship and fruitful discussions. Special thanks goes to Bo Zhen, Song-Liang Chua, and Dr. Ling Lu. The great time that we spent together in discussing physics and watching basketball made a big difference to my life at MIT.

Finally, I dedicate this thesis to my parents Shou-Xiong Qiu and Wan-Ping Zhou, and my wife Qing Xia. Despite the radius of earth, we share every moment of struggling and every step of achievement. This thesis would have not been possible without their unconditional and unparalleled love.

Contents

List of Figures

Chapter 1

Overview

Technology advancement in the past decades has enabled the design and fabrication of structures at length scales comparable to, or even smaller than the wavelength of light. The interaction of light with these nanoscale features leads to the tight confinement of light and significantly enhanced light-matter interactions. For instance, photonic crystal cavities have been used to enhance a variety of nonlinear optical processes [1], such as optical switching, second harmonic generation, and spontaneous emission; Meanwhile, surface plasmon resonance has been applied to enhance Raman scattering signals, enabling the optical detection and spectroscopy of single molecules [2]. In general, nanophotonic structures can enhance light-matter interactions by orders of magnitude, providing numerous opportunities in realizing high bandwidth, high speed, ultra-compact, and low power optical components. In this thesis, we will explore three nanophotonics phenomena which enable strong light-matter interaction.

The first phenomenon that we explore (in Chapter 2) is plasmonic resonance. The surface plasmon mode at metal/dielectric boundaries can confine light at sub-wavelength scale, and significantly enhance the scattering and absorption of nanoparticles with metal/dielectric shells [3]. While at resonance, the scattering and absorption cross-sections of such nanoparticles are on the order of wavelength squared, which can be much larger than their physical cross-sections, making these nanoparticles super-scatters and/or super-absorbers. Nanoparticles have wide applications in biomedical imaging, photothermal therapy and optical obscurance. Because dif-

ferent applications have different requirements, a systematic approach to tailor the optical response of such nanoparticles is highly valuable. Here, we propose an optimization based theoretical approach to tailor the optical response of silver/silica multilayer nanospheres over the visible spectrum. Our results show that the structure that provides the largest cross-sections per volume/mass, averaged over a wide frequency range is always the silver-shell silica-core bilayer structure. We also show that the minimal cross-sections per volume/mass over the entire visible spectrum can be enhanced by using a properly chosen mixture of several species of different nanoparticles.

The second phenomenon that we studied (in Chapter 3) is photonic chiral edge state (PCES) [4]. PCES are a novel class of electromagnetic modes that propagate in only one direction. Based on the directional coupling between PCES and ordinary two-way waveguide, we propose a new type of optical circulators. Unlike cavity based optical circulators whose operating bandwidths are limited by the quality factor of the nonreciprocal cavity, the operating bandwidth of the new circulators is tied to the bandwidth of the directional waveguide coupler, and has the potential of simultaneous broadband operation and small device footprint. By interfacing gyromagnetic photonic crystals with magneto-optical bandgaps and ordinary photonic crystals with overlapping bandgaps, we design concrete examples of three-port and four-port optical circulators. The performance of such circulators are then analyzed using full structure finite element simulations and scattering matrix method.

The third phenomenon that we investigated (in Chapter 4) is Stimulated Brillouin Scattering (SBS) [5,6]. SBS is a third order nonlinear process where two optical modes are coupled through an elastic mode. Specifically, the interference of pump and Stokes waves generates a time-varying optical force at the beat frequency. This optical force, while at resonance with an elastic mode, can excite the mechanical vibration of the structure, which in turn scatter light between pump and Stokes waves through index modulations and shifting boundaries. SBS has wide applications in efficient phonon generations, optical frequency conversion, slow light, and signal processing scheme. Just as other nonlinear processes, SBS can be greatly enhanced for

nanoscale waveguides. The strong confinement of light and sound in nanoscale waveguides also brings up two new features. First, the interaction of light with waveguide boundaries is significantly enhanced, creating a new form of SBS nonlinearity through optical pressure. Second, the optical and elastic modes in nanoscale waveguides cannot be approximated as plane-waves. The vector nature of both fields and the tensor nature of dielectric/elastic constants have to be fully appreciated. Since the conventional treatment of SBS gains for microscale waveguides doesn't capture these two features, we develop a general framework of calculating SBS gains via the overlap integral between optical and elastic eigen-modes. Applying this method to a silicon rectangular waveguide, we demonstrate that the optical force distributions and elastic modes jointly determine the magnitude and scaling of both forward and backward SBS gains. In addition, we find that it is the coupling to the leaky channels in the substrate that stifles the forward SBS gains in a standard SOI waveguide. Applying this method to a silicon periodic waveguide, we show that SBS nonlinearity can be further enhanced in the slow light regime.

From the theoretical analysis of SBS processes in simple waveguide structures, we can see that SBS can create highly efficient photon-phonon coupling over a wide frequency range. Taking this idea further, we collaborated with researchers in Sandia to propose (in Chapter 5) a novel class of hybrid photon-phonon waveguides. In this suspended membrane-waveguide structure, optical modes and elastic modes can be tuned nearly independently. Our numerical calculation shows that the optical mode can be efficiently coupled to a series of approximately equally spaced elastic modes through a constructive combination of electrostriction force and radiation pressure. In addition, we develop a set of coupled amplitude equations to quantitatively describe the Fano-like nonlinear response of the real structures fabricated by our collaborators in Sandia. By fitting the measured nonlinear response to the coupled amplitude equations, we can extract the resonant frequencies and SBS gains of the real structure, which shows excellent agreement with the numerical calculation. The realized SBS gain is more than 1000 times larger than the recent demonstration in silica fibers.

Throughout the study, we combine semi-analytical approaches and full numeri-

cal calculations to model various nanophotonic structures. The semi-analytical approaches we used include spatial coupled mode theory and scattering matrix method. Spatial coupled mode theory captures the interaction between traveling optical waves, which is suitable for the analysis of waveguide couplers (Chapter 3) and hybrid photon-phonon waveguides (Chapter 5). Scattering matrix method decomposes a complicated structure into simple elements connected with each other through ports, which is suitable for the analysis of optical circulators (Chapter 3). For full numerical calculations, we used finite element method. Finite element method can calculate the frequency response of an extended structure. It can also calculate the eigen-modes of a finite or period structure. Finite element method has two additional features. First, variables can be defined over geometries of different dimensions. For instance, optical body forces can be defined over volumes, while optical pressures can be defined over boundaries. Second, multiple physical fields such as electromagnetic field and mechanical displacement field can be defined over the same set of geometry and meshes. It allows for the direct calculation of the coupling between different fields without interpolating the solution at grid points. These two features turn out to be very useful in optomechanical calculations (Chapter 4 and 5).

Chapter 2

Optimization of Optical Response of Multilayer Nanospheres

2.1 Introduction

Nanoparticles with strong optical response, characterized by scattering, absorption and total cross-sections, have wide applications in biomedical imaging, photothermal therapy, and optical obscurance [7–9]. Different applications require different optical response properties. For instance, real-time biomedical imaging is based on large scattering cross-sections, while photothermal therapy requires nanoparticles with large absorption cross-sections and small scattering cross-sections. For obscurance applications [10, 11], the ideal nanoparticle should typically have large total cross-sections over the whole visible spectrum while keeping the volume or mass of nanoparticles as small as possible. The diversity and complexity of these requirements necessitate an engineering approach of nanoparticle design.

Previous studies on the optical response of nanoparticles are mainly based on parametric approach [3,12,13], which works well for simple structures. However, when the structure becomes complicated and the number of design parameters increases, optimization becomes the preferable approach because it can efficiently explore the whole parameter space. Furthermore, because the optimization objective function can be an arbitrary transformation of the frequency-dependent cross-sections, this

approach is very powerful in tailoring the optical response of nanoparticles over a wide frequency range.

For example, some applications may require that the optical resonance has both a strong peak value and a wide bandwidth. This can be achieved by maximizing the average cross-section over the bandwidth of interest. For another example, some applications may want the nanoparticle has strong absorption and minimal scattering. This can be achieved by setting the objective function as the difference between absorption and scattering cross-sections. For obscurance applications, we want the total cross-section to be consistently large over the whole visible spectrum. This is equivalent to maximizing the minimal cross-section over this spectrum. In this chapter, we will use an optimization tool to tailor the optical response of multilayer nanospheres over wide frequency range of interest.

Before we start, we need to select the material system. Nanoparticles composed of metal and dielectric materials support surface plasmons on the metal/dielectric interfaces and can strongly interact with light in the visible range [14–18]. At resonance, the cross-sections of these nanoparticles are proportional to wavelength square and independent of their physical size. Therefore, the cross-sections of these nanoparticles can be much larger than their physical cross-sections, which makes them super-scatterers and super-absorbers [19–22]. Furthermore, the plasmon resonance frequency can be tuned by varying the physical structure of the nanoparticles. In order to be able to tailor the optical response of nanoparticles over a wide frequency range, we choose the metal/dielectric material system. For concreteness, we will focus on the silver/silica material system.

In this chapter, we first formulate the Transfer Matrix Method to calculate the optical response of multilayer nanospheres. After briefly reviewing the optical response of bilayer silver/silica nanospheres, we proceed to optimize the average cross-section of various silver/silica multilayer nanospheres. Our results show that the structure with the maximal average cross-section is the bilayer silver/silica structure with silver as the shell. Finally, we investigate using a mixture of several species of bilayer nanospheres to enhance the minimal cross-sections over the entire visible range.

2.2 Transfer matrix calculation of optical response

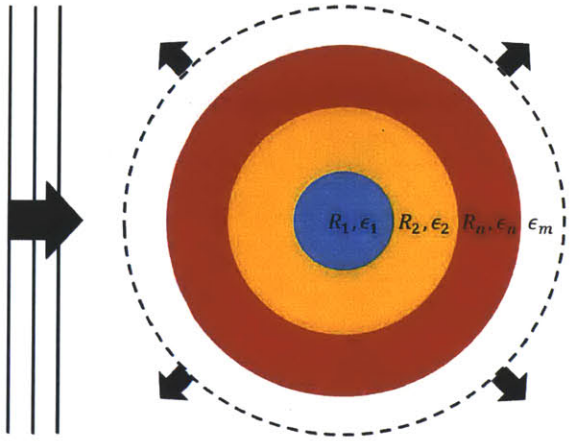

Figure 2-1: Schematic of an n layer nanosphere embedded in infinite dielectric medium. The outer radius and dielectric function of individual layers are $(R_i, \epsilon_i), i = 1, 2, ..., n$. The dielectric function of the medium is ϵ_m. The solid lines represent an incident plane wave which contains incoming and outgoing waves. The dashed line represents the scattered wave which only contains outgoing wave.

We start by formulating the Transfer Matrix Method for multilayer nanosphere [23, 24]. Consider a multilayer nanosphere shown in Fig. 2-1. Because of the spherical symmetry, the fields at a given incident frequency can be decomposed into two orthogonal polarizations: transverse electric (TE) and transverse magnetic (TM). For TE polarization, the electric fields can be written as $\mathbf{E}_{TE} = \nabla \times \mathbf{r}\phi_{TE}$. For TM polarization, the magnetic fields can be written as $\mathbf{H}_{TM} = \nabla \times \mathbf{r}\phi_{TM}$. The scalar potential ϕ_{TE} and ϕ_{TM} satisfy the scalar Helmholtz equation $\nabla^2\phi + k^2\phi = 0$ where $k^2 = \omega^2\epsilon(\mathbf{r})$. Due to the spherical symmetry, ϕ can be decomposed into a discrete set of spherical modes: $\phi_{lm} = R_l(r)P_l^{|m|}(\cos\theta)\exp(im\varphi)$ with $l = 0, 1, 2, ...$ and $m = -l, ..., l$. Since $\epsilon(\mathbf{r})$ is a constant ϵ_i inside the i^{th} shell, $R_l(r)$ is a linear combination of the first and second kind spherical Bessel functions within the individual shells:

$$R_l(r)|_i = A_i j_l(k_i r) + B_i y_l(k_i r) \tag{2.1}$$

The coefficients (A_i, B_i) of adjacent shells are linked by the transfer matrix of the

interface:

$$\begin{bmatrix} A_{i+1} \\ B_{i+1} \end{bmatrix} = M_{i+1,i} \begin{bmatrix} A_i \\ B_i \end{bmatrix} \tag{2.2}$$

The matrix element is determined by the boundary condition satisfied by $R_l(r)$, which comes from the continuity of the tangent components of $\mathbf{E}$ and $\mathbf{H}$ across the boundary. For TE polarization, $rR_l(r)$ and $(rR_l(r))'$ are continuous across the boundary. By writing the continuity conditions in matrix form, we get:

$$\begin{aligned} M_{i+1,i} = & \begin{bmatrix} j_l(k_{i+1}R_i) & y_l(k_{i+1}R_i) \\ j_l'(k_{i+1}R_i)k_{i+1}R_i + j_l(k_{i+1}R_i) & y_l'(k_{i+1}R_i)k_{i+1}R_i + y_l(k_{i+1}R_i) \end{bmatrix}^{-1} \times \\ & \begin{bmatrix} j_l(k_iR_i) & y_l(k_iR_i) \\ j_l'(k_iR_i)k_iR_i + j_l(k_iR_i) & y_l'(k_iR_i)k_iR_i + y_l(k_iR_i) \end{bmatrix} \end{aligned} \tag{2.3}$$

For TM polarization, $rR_l(r)$ and $(\epsilon^{-1}rR_l(r))'$ are continuous across the boundary. By writing the continuity conditions in matrix form, we get:

$$\begin{aligned} M_{i+1,i} = & \begin{bmatrix} j_l(k_{i+1}R_i) & y_l(k_{i+1}R_i) \\ j_l'(k_{i+1}R_i)k_{i+1}R_i + j_l(k_{i+1}R_i) & y_l'(k_{i+1}R_i)k_{i+1}R_i + y_l(k_{i+1}R_i) \end{bmatrix}^{-1} \times \\ & \begin{bmatrix} j_l(k_iR_i) & y_l(k_iR_i) \\ \frac{\epsilon_{i+1}}{\epsilon_i}(j_l'(k_iR_i)k_iR_i + j_l(k_iR_i)) & \frac{\epsilon_{i+1}}{\epsilon_i}(y_l'(k_iR_i)k_iR_i + y_l(k_iR_i)) \end{bmatrix} \end{aligned} \tag{2.4}$$

The transfer matrix of the whole system can be calculated by cascading the transfer matrices of individual interfaces.

$$\begin{bmatrix} A_{n+1} \\ B_{n+1} \end{bmatrix} = M_{n+1,n}M_{n,n-1}...M_{3,2}M_{2,1} \begin{bmatrix} A_1 \\ B_1 \end{bmatrix} = M \begin{bmatrix} A_1 \\ B_1 \end{bmatrix} \tag{2.5}$$

Since the second kind of Bessel function is singular at the origin, we can set $A_1 = 1$ and $B_1 = 0$. So the coefficients of Bessel functions in the surrounding medium are directly given by the transfer matrix element, $A_{n+1} = M_{11}$ and $B_{n+1} = M_{21}$. Within the surrounding medium, it is convenient to write the radical function as a linear

combination of the spherical Hankel functions:

$$R_l(r)|_{n+1} = C_{n+1}h_l^1(k_{n+1}r) + D_{n+1}h_l^2(k_{n+1}r) \tag{2.6}$$

where coefficients C_{n+1} and D_{n+1} are related to A_{n+1} and B_{n+1} through:

$$\begin{aligned} C_{n+1} &= \frac{A_{n+1} - iB_{n+1}}{2} \\ D_{n+1} &= \frac{A_{n+1} + iB_{n+1}}{2} \end{aligned}$$

Taking the convention that the fields vary in time as $e^{-i\omega t}$, $h_l^1(k_{n+1}r)$ and $h_l^2(k_{n+1}r)$ correspond to outgoing and incoming waves respectively. The reflection coefficient of the whole system is given by

$$r_l = \frac{C_{n+1}}{D_{n+1}} = \frac{M_{11} - iM_{21}}{M_{11} + iM_{21}} \tag{2.7}$$

The reflection coefficient as a function of frequency determines the optical response of the nanoparticle under all possible illumination conditions. Specifically, when the nanoparticle is illuminated by a linearly polarized plane wave, the incident field can be decomposed into both TE and TM channels (l, m) with $l = 1, 2, ...$ and $m = -1, 1$. For each channel, the incident field contains both incoming and outgoing waves carrying the same power [19–22]

$$P_{l,m=\pm1} = \frac{\lambda^2}{16\pi}(2l+1)I_0 \tag{2.8}$$

where I_0 is the incident intensity, and λ is the wavelength in the surrounding medium. The scattered field is a purely outgoing wave characterized by the scattering coefficient S_l which is related to the reflection coefficient through $S_l = (r_l - 1)/2$. The scattered and absorbed power in this channel is given by:

$$P_{l,m=\pm1}^{sca} = \frac{\lambda^2}{16\pi}(2l+1)I_0|1 - r_l|^2 \tag{2.9}$$

$$P_{l,m=\pm1}^{abs} = \frac{\lambda^2}{16\pi}(2l+1)I_0(1 - |r_l|^2) \tag{2.10}$$

By summing over the contribution from all channels of TE and TM polarization, we get the scattering and absorption cross-sections:

$$\sigma_{sca} = \sum_{\sigma}\sum_{l=1}^{\infty}\frac{\lambda^2}{8\pi}(2l+1)|1-r_{\sigma,l}|^2 \tag{2.11}$$

$$\sigma_{abs} = \sum_{\sigma}\sum_{l=1}^{\infty}\frac{\lambda^2}{8\pi}(2l+1)(1-|r_{\sigma,l}|^2) \tag{2.12}$$

where σ is TE or TM. The total cross-section is the sum of the scattering and absorption cross-sections. $\sigma_{tot} = \sigma_{sca} + \sigma_{abs}$.

2.3 Silver/silica bilayer nanospheres

In this section, we analyze the optical response of silver/silica bilayer nanospheres as the building elements of multilayer structures. For silver, the complex dielectric function as a function of frequency is generated by linearly interpolating the experimental data [25]. For simplicity, the size dependence of Ag's dielectric function is not taken into account. For silica, the dielectric function is taken as a constant $\epsilon = 2.1$. There are two configurations of silver/silica bilayer nanoparticle depending on the core material.

First, we consider silica coated silver spheres. Colloidal suspensions of such nanoparticles were obtained from Nanocomposix (Nanocomposix Inc., San Diego, CA). Figure 2-2 shows the measured and calculated total cross-sections of the fabricated nanoparticles. The calculation agrees quite well with the measurement. The total cross-section peaks around 455nm. This peak comes from the $l = 1$ surface plasmon mode at the silver/silica boundary. The peak wavelength only varies slightly when the inner and outer radius change. For instance, consider a silica coated silver sphere suspended in air. Fixing the outer radius at 50nm, the peak wavelength varies from 410nm to 415nm when the inner radius varies from 5nm to 45nm. Fixing the aspect ratio R_1/R_2 at 0.8, the peak wavelength varies from 390nm to 480nm when the outer radius varies from 25nm to 75nm.

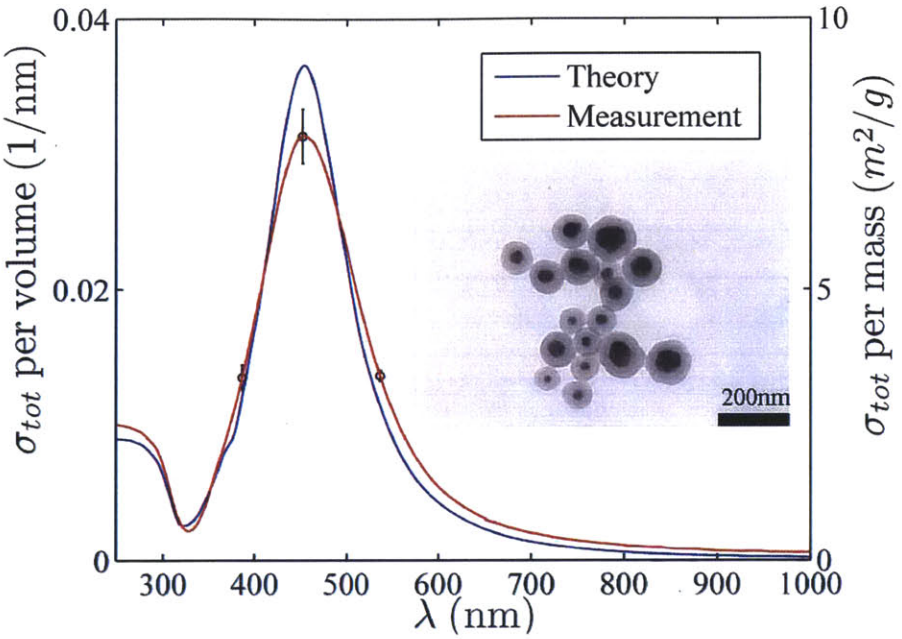

Figure 2-2: The total cross-section of silica coated silver spheres suspended in ethanol. The cross-section is normalized by volume (the left axis) and mass (the right axis). The insert is a TEM image of the fabricated nanoparticles. The radius of the silver core has a distribution with mean 26.3nm and standard deviation 9.3nm. The thickness of the silica shell is around 25.3nm. The red line is the measured total cross-section. The black bar represents the standard deviations from eight transmission measurement on eight samples. The blue line is the Transfer Matrix calculation of the total cross-section with the radius of the silver core sampled from the measured distribution and the thickness of the silica shell fixed at 25.3nm. The dielectric function of ethanol is taken as $\epsilon_m = 1.85$.

In contrast, the surface plasmon resonance of the reverse configuration has great tunability over the visible range [14–18]. Consider a silver coated silica sphere suspended in air. Fixing the outer radius at 50nm, the peak wavelength varies from 405nm to 720nm when the inner radius varies from 5nm to 45nm. Besides the peak wavelength, the relative strength of scattering and absorption cross-sections in the total cross-section also vary. For $[R_1, R_2] = [5\text{nm}, 50\text{nm}]$, the absorption cross-section accounts for 25% of the total cross-section at resonance. For $[R_1, R_2] = [45\text{nm}, 50\text{nm}]$, this percentage rises to 60%. The tunability of the resonance wavelength and the tunability of the total cross-section composition makes silver coated silica sphere a good candidate for achieving broadband optical response.

2.4 Optimization of average cross-sections over wide frequency range

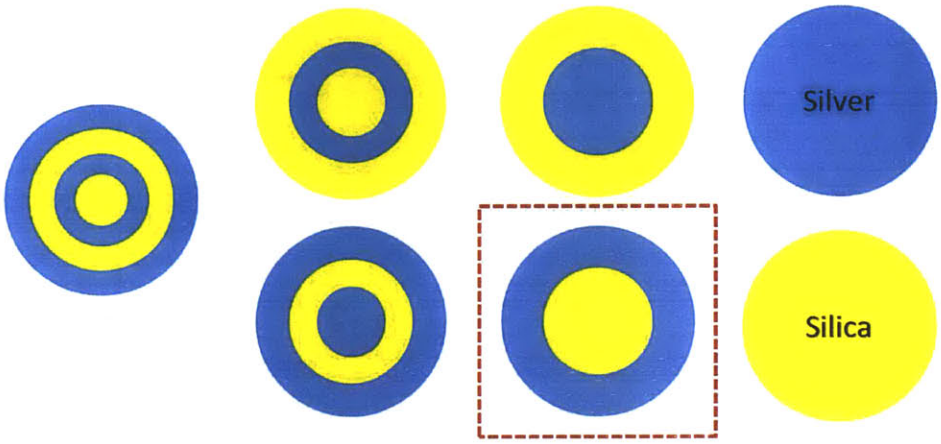

Figure 2-3: A schematic of a four layer nanosphere. This structure includes nanospheres with one through three layers as boundary points. The structure enclosed in red square is the optimal structure found by the optimization engine.

The optical response of silver/silica bilayer nanosphere indicates that increasing the number of metal/dielectric interfaces can provide additional tunability in the optical response. Using this insight, we aim to design silver/silica multilayer nanosphere with a large average cross-section over wide frequency range. The figure of merit (FOM) is the scattering, absorption, and total cross-section averaged over the target frequency range, normalized by volume or mass.

$$FOM = \frac{1}{\omega_{max} - \omega_{min}} \int_{\omega_{min}}^{\omega_{max}} \sigma_{normalized} d\omega \tag{2.13}$$

For concreteness, we take 400-600nm and 600-800nm as the target frequency range of interest. The structure under consideration is a multilayer nanosphere with alternating silver and silica layers (four layers in total). The design parameters are the thicknesses of individual layers. The upper bound of the allowed thickness is set to be a large value (1μm). The lower bounds of the thicknesses are set to be zero. If the thickness of some layers hit zero, the number of layers in the whole system decreases.

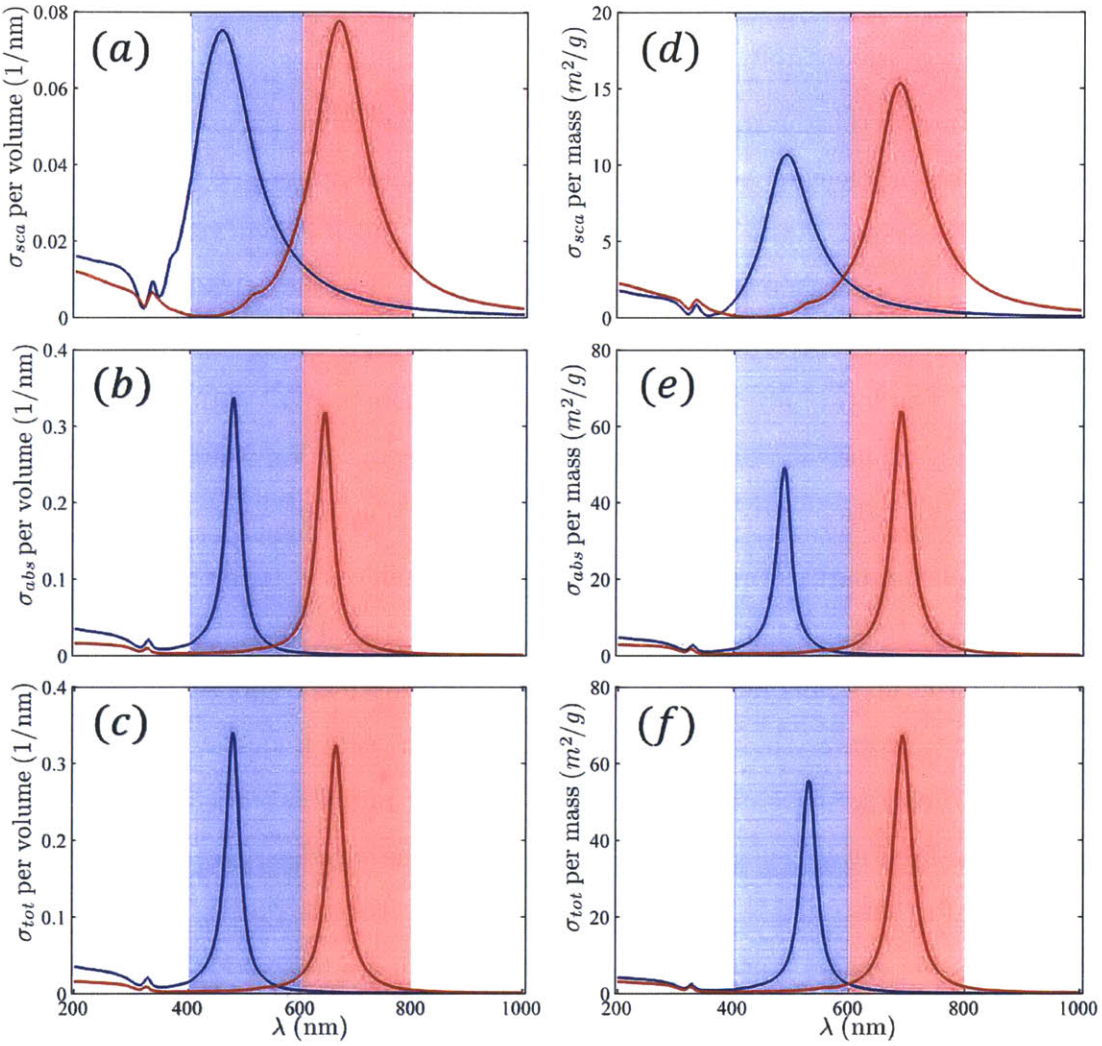

Figure 2-4: Optimization of average cross-sections over wide frequency range. The structure under consideration is a silver/silica multilayer nanosphere. The optimal structure found by the optimization engine is always silver coated silica sphere. For all subfigures, blue (red) lines show the optimized average cross-sections over the blue (red) shaded frequency range. (a)(b)(c) correspond to scattering, absorption and total cross-sections per volume respectively. (d)(e)(f) correspond to scattering, absorption and total cross-sections per mass respectively. The radius of the silica cores and the thickness of silver shells exhibiting the cross-sections shown above are given in Table 2.1.

Therefore, this general structure includes structures with fewer layers (one through five layers) as boundary points (Fig. 2-3). If a simpler structure turns out to be the optimal structure, the optimization engine will find this structure by converging to the boundary of the feasible region.

We performed the optimization using numerical optimization package NLOPT [26]. Since this problem is nonconvex, there are many local optima. To find the global optima in the design parameter space, we used Multi-Level-Single-Linkage (MLSL) algorithm. This algorithm performs a sequence of local optimization from random points by a clustering heuristic that helps it to avoid repeated searches of the same optima [27]. The local optimization algorithm used here is BOBYQA [28]. This algorithm performs derivative-free bound-constrained optimization using an iteratively constructed quadratic approximation of the objective function.

Figure 2-4 summarizes the optimization results. In all cases, the optimal structure returned by the optimization engine is always a silver coated silica sphere. Although multilayer structures can offer greater tunability of the optical response, bilayer structures already maximize the average cross-section over wide frequency range. From Table 2.1, we can see that nanospheres with an outer radius around 70nm have the largest normalized average scattering cross-section. The wavelength of the scattering peak can be further tuned by varying the aspect ratio. For absorption cross-sections, our optimization engine found many local optima with approximately equal FOM's. These local optima have the same aspect ratio, and the thickness of the silver layer varies from zero to several nanometers. This can be explained by the quasi-static approximation. The absorption cross-section of a nanoparticle can be written as $\sigma_{abs}(\omega) = \omega Im[\alpha(\omega)]$, where $\alpha(\omega)$ is the polarizability [29–31]. When the nanoparticle diameter is much smaller than the wavelength, the quasi-static approximation is valid, under which the polarizability is proportional to the volume of the nanoparticle with the proportionality coefficient dependent on frequency and aspect ratio [29]. Therefore, the normalized absorption cross-section averaged over a frequency range is only determined by the aspect ratio and independent of the nanoparticle diameter as long as the nanoparticle diameter is much smaller than the wavelength. In Table

2.2, the thickness of the silver layer is set to be $\geq$ 2nm. Nanospheres with thinner silver layers have approximately the same normalized average absorption cross-section but are difficult to fabricate. The structures that give the largest average scattering and absorption cross-sections are quite different. Since the FOM of the absorption cross-section is about twice as large as the FOM of the scattering cross-section, the structure that gives the largest average total cross-section is essentially identical to the structure providing the largest average absorption cross-section. The structures given in Table 2.1 are super-scatters and super-absorbers. For instance, the structure with $[R, T]$ = [60.40nm, 8.68nm] has an average scattering cross-section of 8.65m^2/g over 600-800nm, while its physical cross-section is only 2.07m^2/g. The structure with $[R, T]$ = [18.09nm, 2.00nm] provides an average total cross-section of 17.52m^2/g over 600-800nm, which means that only 1g of such nanoparticles, when fully dispersed, can obscure an area as large as 17.52m^2.

2.5 Optimization of the minimal cross-sections over wide frequency range

In this section, we aim to design nanoparticles with consistently large cross-sections over a wide frequency range. This is equivalent to maximizing the minimal cross-section over the target frequency range. From the previous section, we see that silver coated silica spheres have strong surface plasmon resonances, and the peaks of their resonances are highly tunable. Therefore, we expect that a mixture of several species of silver coated silica spheres with different resonance frequencies can effectively cover a wide frequency range.

This intuition can be formalized by optimization language. We take the target wavelength range to be 400-800nm. The FOM is the minimal cross-section over this range, normalized by either volume or mass.

$$FOM = \min_{\omega} \sigma_{normalized} \tag{2.14}$$

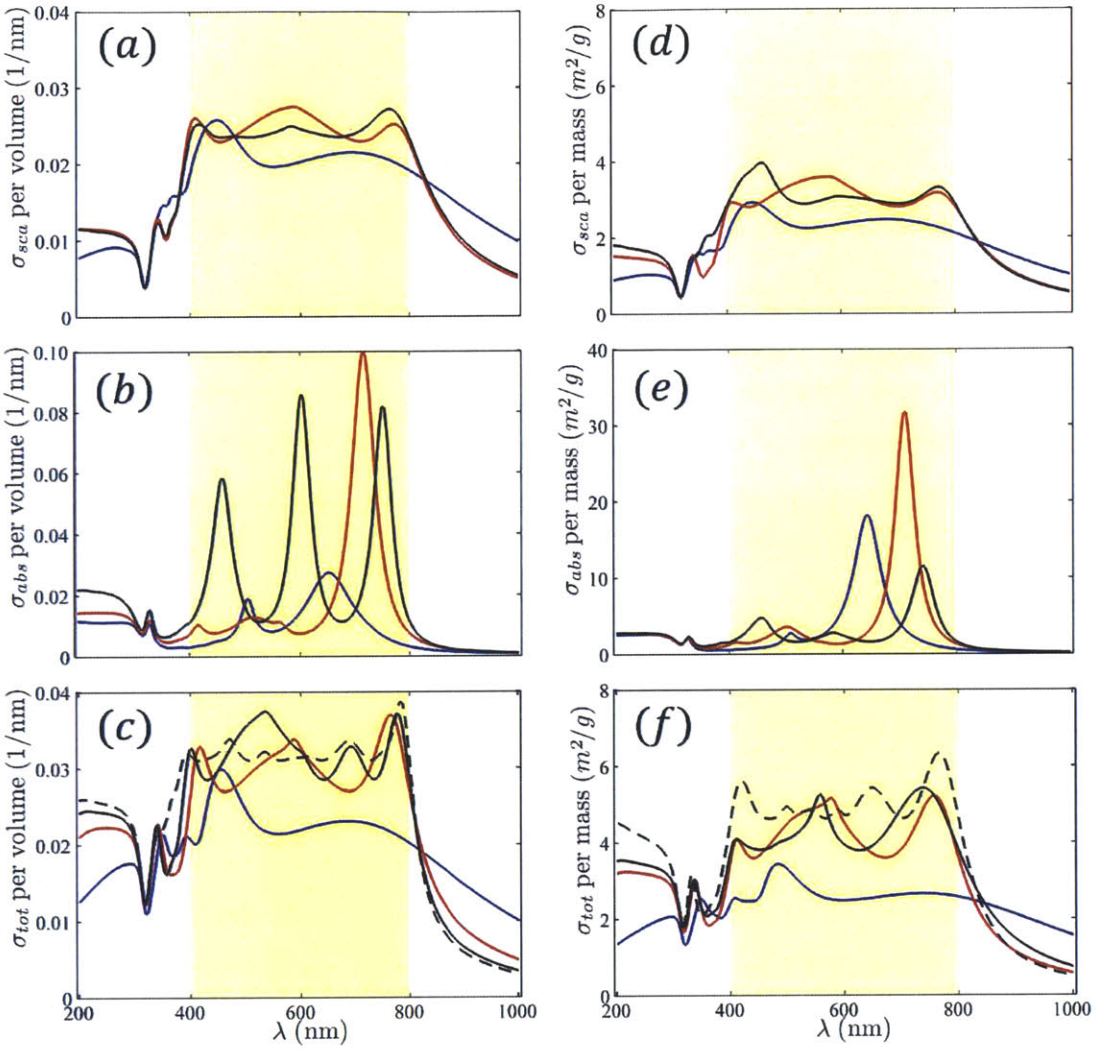

Figure 2-5: Optimization of minimal cross-sections over a wide frequency range. The structure under consideration is a mixture of several species of silver coated silica spheres. The target frequency range is shaded in yellow. For all subfigures, blue, red, black lines corresponds to one, two, and three species of nanospheres. The black dashed lines in (c) and (f) correspond to ten species of nanospheres. (a)(b)(c) correspond to scattering, absorption, and total cross-sections per volume respectively. (d)(e)(f) correspond to scattering, absorption and total cross-sections per mass respectively. The radius of the silica cores and the thickness of silver shells corresponding to these cross-sections are given in Table 2.2.

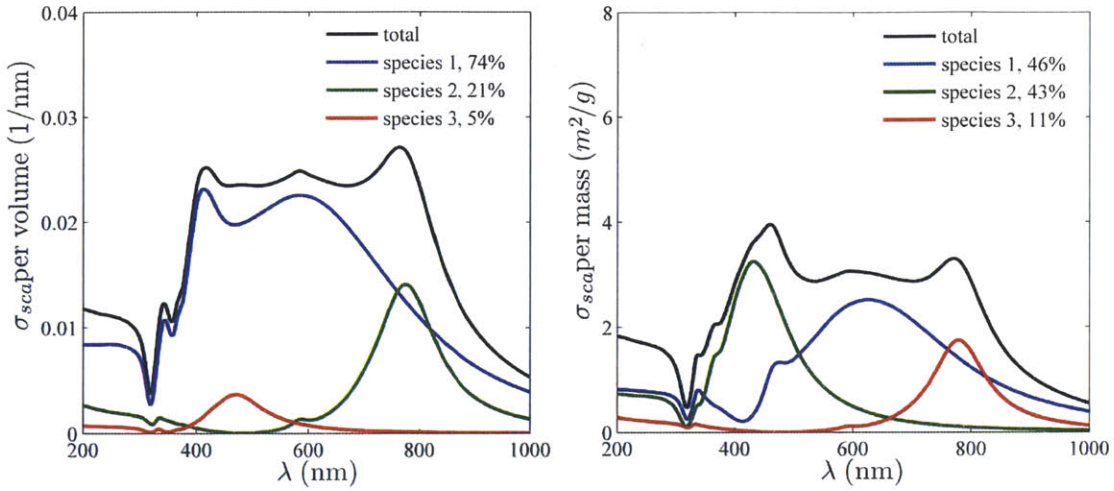

Figure 2-6: A detailed plot of Fig. 2-5(a)(d). The black line corresponds to the optimal mixture of three species. Colored lines correspond to the contributions from individual species.

The structure under consideration is a mixture of N species of silver coated silica spheres where $N = 1, 2, 3, ...$ The design parameters are the size parameters of individual species and relative weights (i.e. proportions) of each species in the mixture. The weights represent the relative weights in volume (mass) when the normalization is over volume (mass).

$$\sigma_{normalized} = \sum_{i=1}^{N} w_i \sigma_{i,normalized} \tag{2.15}$$

When the size parameters of individual species are fixed, the problem of finding the optimal weights turns out to be a Linear Programming (LP) program, which can be efficiently solved by standard LP packages. Therefore, we employed a two-level optimization structure. In the lower level, we used a standard LP solver to find out the optimal weights given the current size parameters. The resulting FOM as a function of size parameters is further optimized in the upper level with the same nonlinear method we used in the previous section. This separation into linear and nonlinear parts of the original optimization problem reduces the dimension of the parameter space and helps MLSL algorithm to find the global optimal in less iterations.

Figure 2-5 summarizes the results. We can see that the optimization engine tries to build a plateau over the target range to maximize the minimal cross-section. For

scattering cross-sections, it is relatively easy to build such a plateau since the scattering peaks have wide bandwidth. When there is only one species (the blue lines in Fig. 2-5(a)(d)), the nanoparticle has a large size so that its $l = 1$ resonance can cover the large wavelength region and its $l = 2$ resonance can cover the small wavelength region. When the number of species increases, the new species try to cover the dips in the previous scattering spectra with their resonant peaks (Fig. 2-6). On the other hand, it is relatively difficult to build an absorption plateau because absorption peaks have narrow bandwidth. The FOM of the scattering cross-section is about twice as large as that of the absorption cross-section. The total cross-section can be enhanced significantly (35% for volume normalization and 46% for mass normalization) when N increases from 1 to 2. The enhancement when N increases from 2 to 3 is only moderate. The benefit of adding more species gradually saturates.

2.6 Concluding remarks

In this chapter, we used optimization tools to tailor the optical response of silver/silica multilayer spheres. We showed that the structure that gives the largest average cross-section over wide frequency range is the bilayer structure with a silver shell. We also showed that using several species of nanoparticles can significantly enhance the minimal cross-section over the whole visible range although this enhancement saturates when the number of species increase. Because the FOM can be an arbitrary function of the frequency dependent cross-sections, the optimization approach described here can be used to design nanoparticles with more complicated optical response.

Table 2.1: Optimization of average cross-sections

Normalized by volume

cross-section	range (nm)	silica (nm)	silver (nm)	FOM (1/nm)
σ_{sca}	400-600	31.25	26.65	0.0486
	600-800	60.32	9.65	0.0464
σ_{abs}	400-600	6.07	2.00	0.0767
	600-800	14.80	2.00	0.0817
σ_{tot}	400-600	6.09	2.00	0.0773
	600-800	16.12	2.00	0.0846

Normalized by mass

cross-section	range (nm)	silica (nm)	silver (nm)	FOM (m^2/g)
σ_{sca}	400-600	38.53	17.88	5.64
	600-800	60.40	8.68	8.65
σ_{abs}	400-600	6.54	2.00	10.87
	600-800	17.89	2.00	16.71
σ_{tot}	400-600	8.71	2.00	10.93
	600-800	18.09	2.00	17.52

Table 2.2: Optimization of minimal cross-sections

Normalized by volume

cross-section	# of species	silica (nm)	silver (nm)	weights (%)	FOM (1/nm)
σ_{sca}	1	68.09	55.44	100	0.0192
	2	52.54	44.21	82.8	0.0229
		73.41	7.63	17.2	
	3	52.85	47.27	74.4	0.0235
		75.61	8.31	20.8	
		35.55	23.21	4.8	
σ_{abs}	1	60.14	10.00	100	0.0032
	2	37.03	4.00	57.5	0.0075
		44.02	15.99	42.5	
	3	22.95	10.26	37.4	0.0114
		26.08	4.39	34.3	
		21.96	2.00	28.3	
σ_{tot}	1	80.15	41.87	100	0.0201
	2	59.96	34.12	82.8	0.0270
		61.96	6.29	17.2	
	3	50.21	32.98	75.2	0.0285
		52.97	4.90	14.4	
		55.76	7.32	10.4	
	10	...	...	...	0.0310

Normalized by mass

cross-section	# of species	silica (nm)	silver (nm)	weights (%)	FOM (m^2/g)
σ_{sca}	1	67.95	52.38	100	2.10
	2	52.77	38.70	87.4	2.80
		75.72	8.17	12.6	
	3	76.71	21.93	46.1	2.88
		21.96	34.54	43.2	
		70.45	7.31	10.7	
σ_{abs}	1	42.80	6.55	100	0.58
	2	20.56	2.15	51.3	1.31
		37.16	13.61	48.7	
	3	27.43	14.22	36.9	1.59
		49.06	11.02	34.9	
		36.66	3.66	28.2	
σ_{tot}	1	92.95	39.04	100	2.46
	2	55.54	29.60	83.5	3.59
		67.77	7.39	16.5	
	3	53.36	29.01	60.1	3.79
		79.49	10.25	31.1	
		24.64	25.04	8.8	
	10	...	...	...	4.62

Chapter 3

Broadband Optical Circulator based on One-Way Waveguide

3.1 Introduction

Nonreciprocal optical devices, such as circulators and isolators, are essential components in large-scale integrated photonic circuits, due to their ability to suppress crosstalk and fringes among constituent stages [32–36]. Circulators are widely used in fiber-optic interferometries to suppress laser noise and can be integrated with channel add/drop filters in switching applications [37]. In the past decade, the efforts to miniaturize nonreciprocal devices have been focusing on enhanced magneto-optical response in resonators and guided-wave structures [38, 39]. Particularly, on-chip optical circulators have been proposed using photonic crystal resonators with overall dimensions at few-wavelength scale [40–47] and nonreciprocal waveguides at hundreds of wavelengths [48–51]. Resonator-based circulators rely on nonreciprocal coupling between waveguides and two counter-rotating resonant modes, where the resonant frequencies are split by magneto-optical effects [41, 52]. As a consequence, resonant circulators are inherently narrow-band, with the operational bandwidth limited by the magneto-optical constants [41], irrespective of three-port or four-port configurations [40–42]. However, this inherent limit cannot be solved with very strong magneto-optical material alone, because reciprocal coupling directly occurs between the waveguides when

they are closely placed to the resonator to lower quality factor.

To reconcile the needs for both large bandwidth and small device footprint, we propose to use recently-discovered one-way waveguides [4,53–55] to create broadband optical circulators with a device dimension on the order of tens of wavelengths. These photonic one-way modes are highly nonreciprocal: they propagate only along a single direction, while the backward modes are completely evanescent. In this chapter, we use these fundamentally new states of light to create circulators that have the bandwidth potential to span an entire photonic bandgap. The circulators are based on directional couplers between a one-way edge waveguide and a conventional two-way waveguide. As a result, the operational bandwidth is determined by that of a waveguide coupler, without the inherent limit of a resonance. In this chapter, we employ both analytical spatial coupled mode theory and finite-element simulation to analyze the performance of directional couplers. Based on such directional couplers, we present the design and finite element simulation of a three-port and a four-port circulator. Scattering matrix analysis of these devices are also presented to elucidate the directions for further improvement in bandwidth.

3.2 Basic idea

Generally speaking, an optical circulator is a nonreciprocal multi-port device in which, under ideal conditions, light entering any given port is transmitted completely to the subsequent port. Reflected waves not only are blocked from entering upstream stages, but are also separated and can be analyzed using additional optics. Optical circulators require a minimum of three ports, and more ports can be added by cascading multiple three-port circulators [47, 56]. For this reason, we focus on the simplest three-port and four-port configurations in this chapter.

Starting with a three-port circulator, we consider a one-way waveguide where light propagates in a single spatial mode along the forward direction, but is evanescent along the backward direction. A section of the one-way waveguide is placed in the vicinity of a two-way waveguide, in parallel, to form a waveguide coupler as shown in

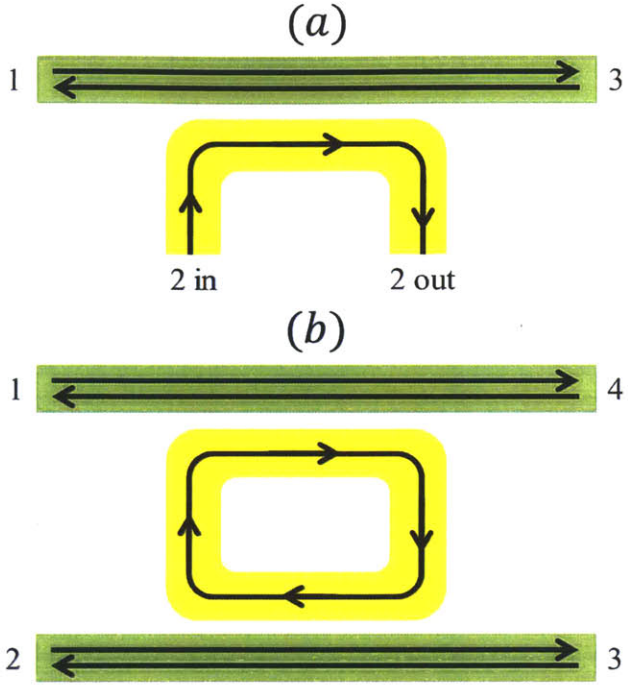

Figure 3-1: Schematics of optical circulators based on one-way waveguides, with the port number illustrated. (a) A three-port circulator constructed from a directional coupler between a one-way waveguide (yellow) and a two-way waveguide (green). The arrows indicate the allowed propagation directions in each individual waveguide, in the absence of other waveguides. Coupling between adjacent waveguides alters the power flow and creates a circulator. (b) A four-port circulator created by cascading two three-port circulators.

Fig. 3-1(a). The optical power will be transferred between the forward modes of the two waveguides periodically. Under a certain set of conditions which will be discussed in detail in the next section, complete energy transfer can occur at certain interaction lengths, and a three-port circulator is created. As illustrated in Fig. 3-1(a), the left and right ends of the two-way waveguide serve as Ports 1 and 3 respectively, while the input and output of Port 2 locate at the two ends of the one-way waveguide. Light entering Port 1 is completely transferred to the one-way waveguide through the directional waveguide coupler and is therefore transmitted to Port 2. In a similar fashion, light entering Port 2 is transmitted to Port 3. In contrast, the backward propagating mode remains in the two-way waveguide and consequently incident light to Port 3 travels to Port 1.

Cascading two three-port circulators produces a four-port circulator [47]. In our implementation, two three-port circulators described above are connected through Port 2, resulting in a circulating one-way waveguide coupled to two two-way waveguides, as shown in Fig. 3-1(b). The ports reside at the ends of the two-way waveguides. Transmission from Port 1 to Port 2 and from Port 3 to Port 4 is mediated twice through waveguide couplers between sections of the one-way and the two-way waveguides. Transmission from Port 2 to Port 3 and from Port 4 to Port 1 takes place without interacting with the one-way waveguide. Overall, the system functions as a four-port circulator, with the ports distributed around the peripheral of the structure in an apparent counter-clock-wise direction opposite to the clock-wise circulation direction of the one-way waveguide.

At the heart of such waveguide-coupler-based circulators is a one-way waveguide where reflection is completely suppressed and full transmission occurs even at sharp corners or near large defects and scatterer. One way waveguide is the electromagnetic analogue of quantum hall effect, exhibiting the breaking of time-reversal symmetry in the most extreme situation. Two classes of one-way waveguides have been proposed: photonic chiral edge states [4,53,55] and surface magnetoplasmons [54,57,58]. Photonic chiral edge states flow at the truncated surfaces of a magneto-optical (gyromagnetic) photonic crystal in a particular frequency range where the bulk crystal features non-trivial topological properties. In contrast, surface magnetoplasmons rely on the splitting and the directional-dependence of the surface plasmon frequency in the presence of a strong external magnetic bias [54]. Although both effects are purely two-dimensional, photonic chiral edge states have been experimentally realized in three-dimensional systems [55, 59]. In this chapter, we choose to focus on photonic chiral edge states, because of the additional degree of freedom from a large number of lattice choices, a large relative bandwidth, and low absorption loss in experimental systems [55]. Nevertheless the concept and the design principle can be readily transferred to surface magnetoplasmon systems.

3.3 Waveguide coupler

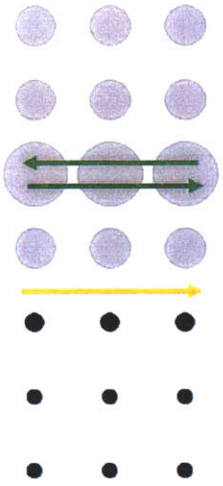

Figure 3-2: Schematics of the waveguide coupler. The lower cladding is a gyromagnetic photonic crystal supporting a one-way waveguide (marked in yellow), while the upper cladding is a dielectric photonic crystal supporting a two-way waveguide (marked in green).

In this section, we propose a concrete implementation of a directional waveguide coupler between a one-way waveguide and a two-way waveguide. Taking a typical structure supporting photonic chiral edge state [4], where light travels only in one direction at the interface between a lower cladding of a gyromagnetic photonic crystal and an upper cladding of a nonmagnetic photonic crystal, we introduce an additional two-way waveguide by creating a line defect one lattice constant away from the interface (Fig. 3-2).

The gyromagnetic photonic crystal consists of a square lattice of yttrium-iron-garnet (YIG) rods in air, with the rod radius $r_1 = 0.11a$ (a is the lattice constant). YIG exhibits strong gyromagnetic response under external magnetic bias, as the permeability tensor takes the form:

$$\mu = \begin{bmatrix} \mu_{\parallel} & i\mu_{\perp} & 0 \\ -i\mu_{\perp} & \mu_{\parallel} & 0 \\ 0 & 0 & 1 \end{bmatrix} \tag{3.1}$$

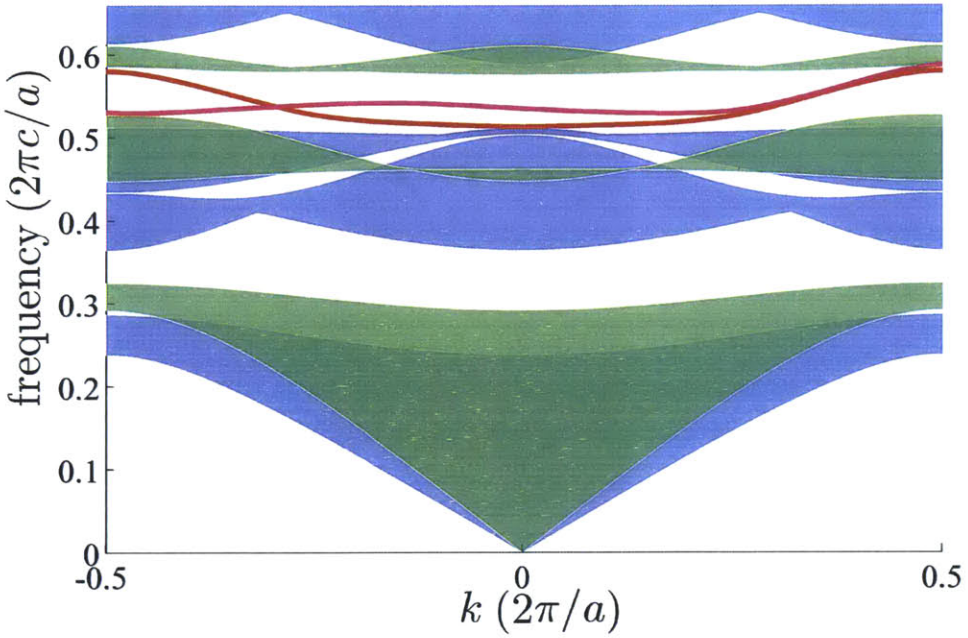

Figure 3-3: Calculated band diagram of the waveguide coupler. The green and the blue regions are the projected band diagrams of the gyromagnetic photonic crystals and the dielectric photonic crystals respectively. An overlapping bandgap, $[0.527, 0.576](2\pi c/a)$, supports a photonic chiral edge state (one-way) at the boundary between the two claddings. The top row of the lower cladding has enlarged rods to adjust the dispersion. The second lowest row of the upper cladding consists of enlarged rods to create a line-defect, serving as a two-way waveguide. The two waveguides couple strongly in the forward (left-to-right) direction. The eigenmodes of the coupled system are shown as the red and purple curves.

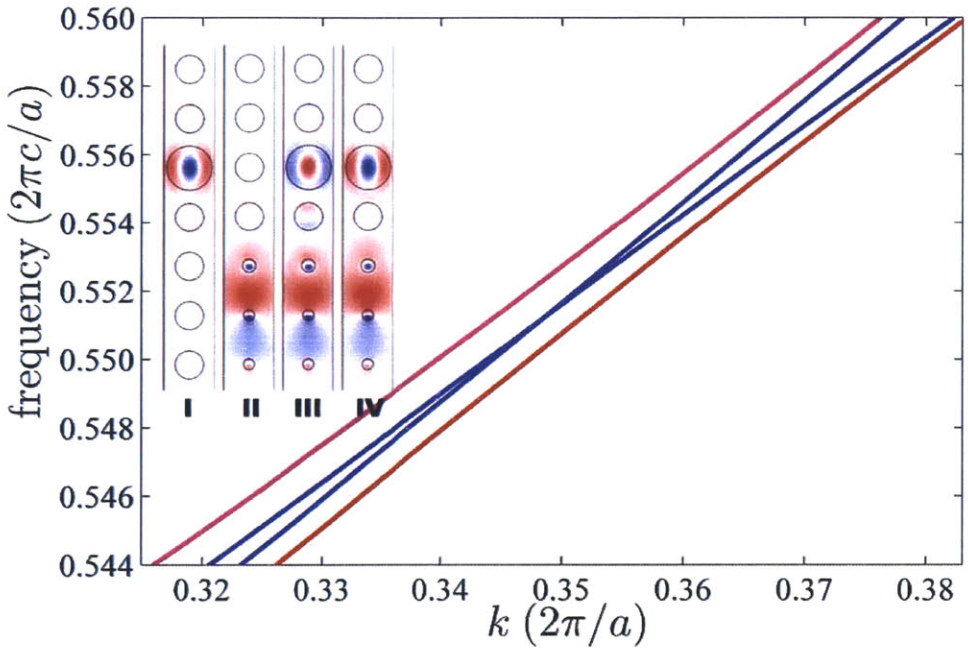

Figure 3-4: Dispersion relation in the k-space where the two forward modes are strongly coupled. The blue curves are unperturbed dispersion relations of the one-way and the two-way modes in the absence of coupling, where the mode profiles are shown in insets I and II. The red and purple curves are the dispersion relations of the compound modes in the presence of coupling (mode profiles shown in inset III and IV). The insets illustrate the calculated E-field distribution at $\omega = 0.551(2\pi c/a)$. For the entire frequency range shown, there is only one backward propagating mode as can be seen in Fig. 3-3.

where $\mu_{\parallel} = 14$, $\mu_{\perp} = 12.4$, corresponding to conditions at 4.28GHz with an external magnetic field of 1600 Gauss [4]. The dielectric constant is $\epsilon_1 = 15$. A bandgap supporting one-way chiral edge modes is found between $0.526(2\pi c/a)$ and $0.576(2\pi c/a)$ for the TM polarization (Fig. 3-3). The dielectric constant and radius of the upper cladding $\epsilon_2 = 8$ and $r_2 = 0.285a$ are chosen to maximize the size of an TM bandgap (between $0.513(2\pi c/a)$ and $0.588(2\pi c/a)$ with the identical mid-gap frequency. At the interface between the two crystals, a one-way chiral edge state emerges through the entire frequency range where the two bandgaps overlap. We added the second waveguide by increasing the rod radius in the second lowest row of the upper cladding. We increase this radius to $0.449a$ and also increase the radius of the rods in the top row of the lower cladding to $0.134a$. As a result, the dispersion relations of the two waveguides intersect at a mid-gap frequency of $0.551(2\pi c/a)$ (Fig. 3-4).

The operational bandwidth of the waveguide coupler directly determines the bandwidth of the circulator. Therefore, it is important to review the analytical theory of a waveguide coupler that guides the design of the dispersion relation of the constituent waveguides. Such an analytical theory also points towards ways to improve transfer efficiency by controlling the difference in the phase velocity between the underlying waveguides. In the weakly-coupled regime, the amplitude of the waves in two parallel waveguides can be described by the following spatial coupled mode equations [60]:

$$\begin{cases} \frac{da_1}{dz} = -j\beta_1 a_1 + \kappa_{12} a_2 \\ \frac{da_2}{dz} = -j\beta_2 a_2 + \kappa_{21} a_1 \end{cases} \tag{3.2}$$

where a_i is the field amplitude and β_i is the wave vector in waveguide i, in the absence of the coupling. The coupling coefficients are related by energy conservation as $\kappa_{12} = -\kappa_{21}^*$, since the spatial coupled-mode theory is not restricted to reciprocal systems [30]. With the coupling coefficient expressed in the absolute value $|\kappa| = |\kappa_1| = |\kappa_2|$, the two eigenmodes in the coupled system possess different propagation constants

$$k_{1,2} = \frac{\beta_1 + \beta_2}{2} \pm \sqrt{\left(\frac{\beta_1 - \beta_2}{2}\right)^2 + \kappa^2} \tag{3.3}$$

and their spatial field distributions are a linear combination of the individual waveguide modes (Fig. 3-4). Light entering into either one of the constituent waveguide simultaneously excites both eigenmodes. Because of their different propagation constants, the spatial beating between the two transfers power between the two waveguides in a back-and-forth manner [61]. Maximum power transfer is given by

$$T = \frac{\kappa^2}{\left(\frac{\beta_1 - \beta_2}{2}\right)^2 + \kappa^2} \tag{3.4}$$

and reaches 100% when $|\beta_1 - \beta_2| \ll \kappa$. The interaction distance to achieve this maximal transfer is given by:

$$L = \frac{\pi}{2\sqrt{\left(\frac{\beta_1 - \beta_2}{2}\right)^2 + \kappa^2}} \tag{3.5}$$

The operation of an ideal circulator requires the waveguide coupler to satisfy the following two conditions over a broad range of frequencies: complete power transfer between the waveguides, and an identical interaction length. Consequently, for the constituent one-way waveguide and two-way waveguide, the ideal conditions include identical dispersion relation $|\beta_1 - \beta_2| \ll \kappa$ and identical coupling constant over as broad frequency range as possible. In our design, the structure has been optimized such that both conditions are met over a relative bandwidth of $\approx 2\%$ (Fig. 3-4).

The performance of the waveguide coupler is verified using a finite-element solver (Fig. 3-5(a)). A point source excites the two-way waveguide in the upper cladding, 11 lattice constants away from the convergence point where the one-way waveguide starts to run parallel to the two-way waveguide. Towards the right side of this convergence point, the waveguide coupler transfers power from the two-way waveguide to the one-way waveguide (Fig. 3-5(b)), as indicated by the flux in each waveguide as a function of the location. At the frequency of $0.551(2\pi c/a)$ where the uncoupled dispersion relations intersect, maximum power transfer reaches 100% efficiency, consistent with the coupled mode theory. Over the frequency range between $0.545(2\pi c/a)$ and $0.554(2\pi c/a)$, the peak transfer efficiency is over above 95%, because $|\beta_1 - \beta_2| \ll \kappa$ is

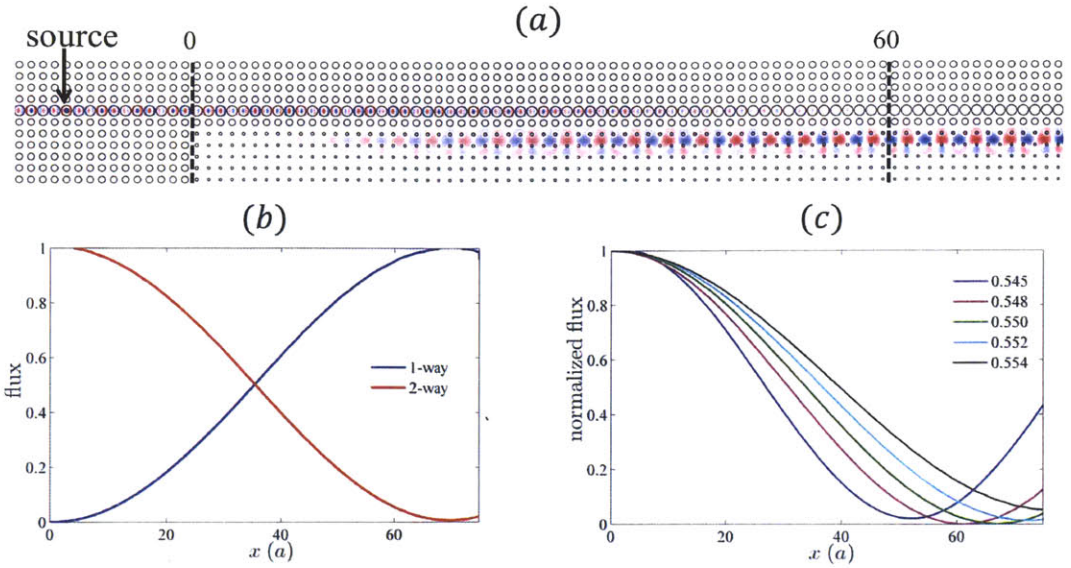

Figure 3-5: Power transport in the waveguide coupler. (a) Steady state E-field pattern at $\omega = 0.551(2\pi c/a)$, showing a complete transfer from the two-way waveguide (incident from the left) to the one-way waveguide. (b) Light is transferred between the two-way waveguide and the one-way waveguide, as indicated by the power flux. (c) Power transfer over a range of frequencies.

satisfied. A small variation in the coupling coefficient κ is observed in this range, resulting in a variation in the interaction length. Even though for a circulator one must use a fixed-length coupler for the entire operational bandwidth, we accomplished less than 1dB transmission ripple over a 2% relative bandwidth at a center frequency of $0.548(2\pi c/a)$ with a $60a$ long waveguide coupler.

3.4 Three-port circulator

Based on such a waveguide coupler, we can construct a three-port circulator as illustrated in Fig. 3-1(a). At the center frequency of $0.548(2\pi c/a)$, complete transmission can be seen from Port 1 to Port 2 (Fig. 3-6(a)) and from Port 3 to Port 1 (Fig. 3-6(b)). The transmission spectra between these ports over a range of frequencies near the center frequency are shown in Fig. 3-7. Even though the transmission from Port 1 to Port 2 decreases as the detuning from the center frequency increases, the

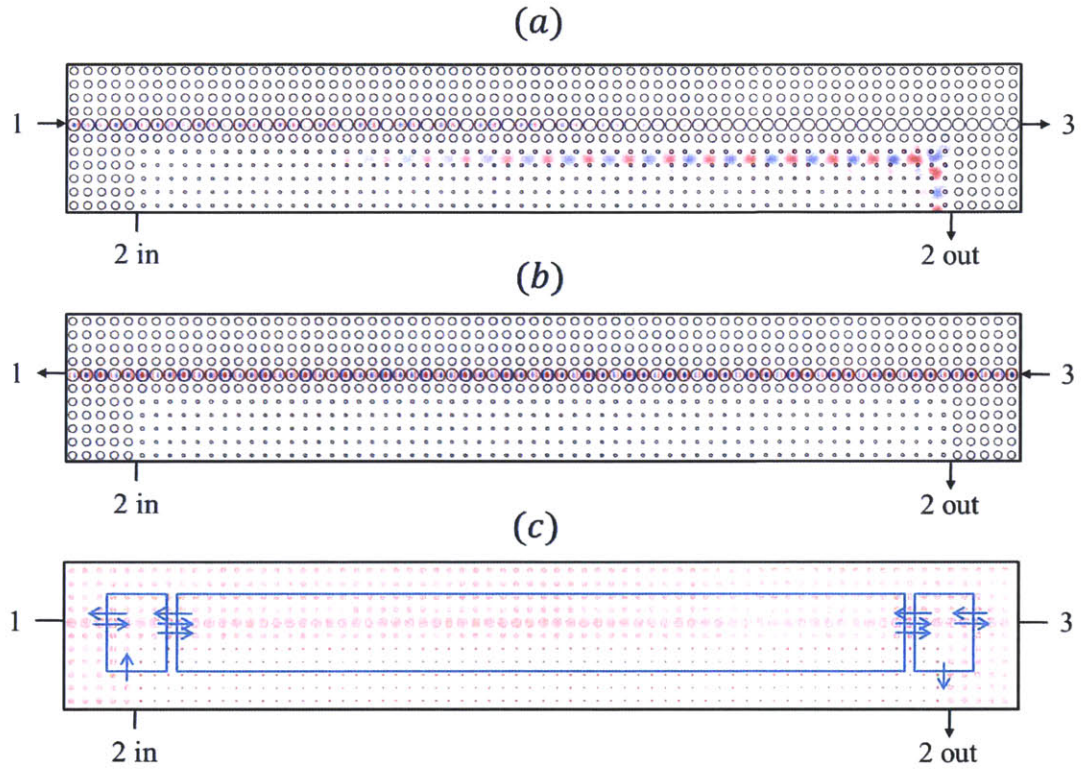

Figure 3-6: Three-port circulator. (a) Steady-state electric-field distribution of a 3-port circulator excited from Port 1 at $\omega = 0.548(2\pi c/a)$. The waveguide coupler transfers light from the two-way waveguide to the one-way waveguide, producing complete transmission at Port 2. (b) Steady-state field distribution with excitation from Port 3 at $\omega = 0.548(2\pi c/a)$, where the transmission is routed to Port 1 instead. The leakage to Port 2 amounts to 0.5% of the total incident flux. (c) The scattering matrix decomposition of the three-port circulator. Arrows indicate distinct modes at boundaries.

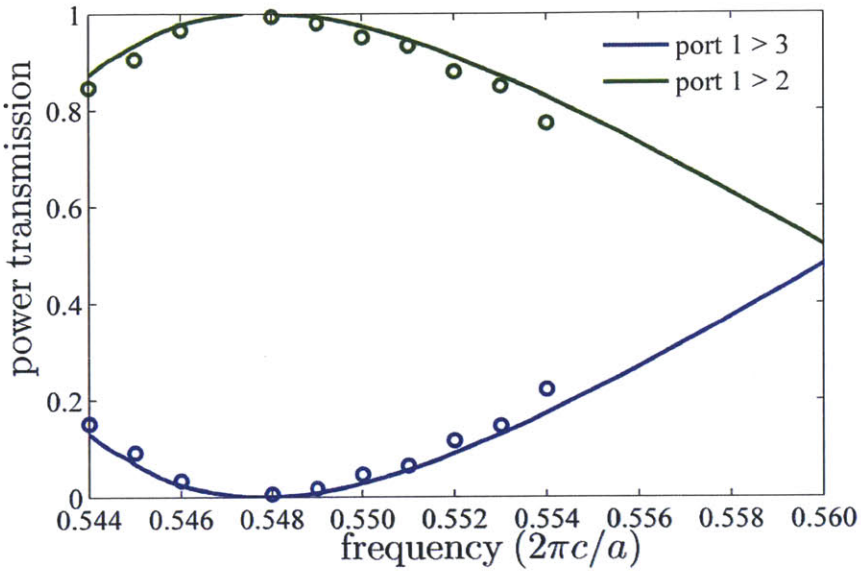

Figure 3-7: The transmission spectra of the three-port circulator excited from Port 1. The finite element simulation (solid curves) agrees well with the scattering matrix calculation (circles).

sum of the transmission to Port 2 and Port 3 remains close to 1. The minimum reflection indicates the performance of the circulator is mainly limited by the bandwidth of the waveguide coupler, rather than the discontinuities in the system. Further structural optimization should yield more optimized dispersion relations for the constituent waveguides, given the large number of degrees of freedom in photonic crystal systems. The 1dB loss bandwidth for this circulator remains 2%.

We also performed scattering matrix analysis to isolate the impact of the waveguide coupler to the overall performance of the three-port circulator and the derived structures that will be discussed later in this chapter. The three-port circulator is compartmentalized into three areas, two corner areas and a tri-mode area (a dual-mode waveguide coupler in the forward direction and a single-mode waveguide in the backward direction), as illustrated in Fig. 3-6(c). Each area has three inputs and three outputs, corresponding to a 3 by 3 scattering matrix. In particular the tri-mode area is described by a simple diagonal matrix with a phase delay $e^{ik_i L}$ on the diagonal

elements, where k_i is the propagation constant of the i^th eigenmode and can be conveniently calculated with mode solvers using plane-wave expansion or finite-element methods. The corner areas require three independent finite-element simulations to extract the matrix element of scattering matrix for each frequency. Combining the scattering matrices of all three areas, we obtain the total scattering matrix of the entire system, where: $|S_{21}|^2$ and $|S_{31}|^2$ are the transmission coefficients from Port 1 to Port 2 and from Port 1 to Port 3 respectively (Fig. 3-7). A good agreement with the finite-element calculation of the full structures suggests that the scattering matrix analysis can be reliably used to examine performance of devices built from these constituent areas, such as cascaded three-port circulators in the next section.

3.5 Four-port circulator

As outlined earlier, additional ports can be introduced by cascading multiple three-port circulators. We present a specific example of synthesizing a four-port circulator by cascading two three-port circulators illustrated in Fig. 3-1(b). This implementation shares a single magneto-optical photonic crystal, on which a circulating edge mode is coupled to two parallel two-way waveguides subsequently and contains two directional couplers. At the previously calculated optimal frequency of the waveguide coupler at $0.548(2\pi c/a)$, the four-port circulator also perform ideally in finite-element calculations: complete transmission occurs from Port 1 to Port 2 through the action of both waveguide couplers (Fig. 3-8(a)), while light incident on Port 4 is routed completely to Port 1 without interacting with the coupler (Fig. 3-8(b)). Similar transport behaviors are found between other ports as well.

At frequencies detuned from the optimal, the transmission of the four-port circulator is rather complex and we resort again to the scattering matrix formalism to understand the contributing factors. In so doing, we could efficiently compute the transmission spectra for devices with various lengths of the waveguide coupler and the vertical sections of the one-way waveguides. The four-port circulator can be decomposed into four corners and two horizontal tri-mode waveguides (coupler) and two

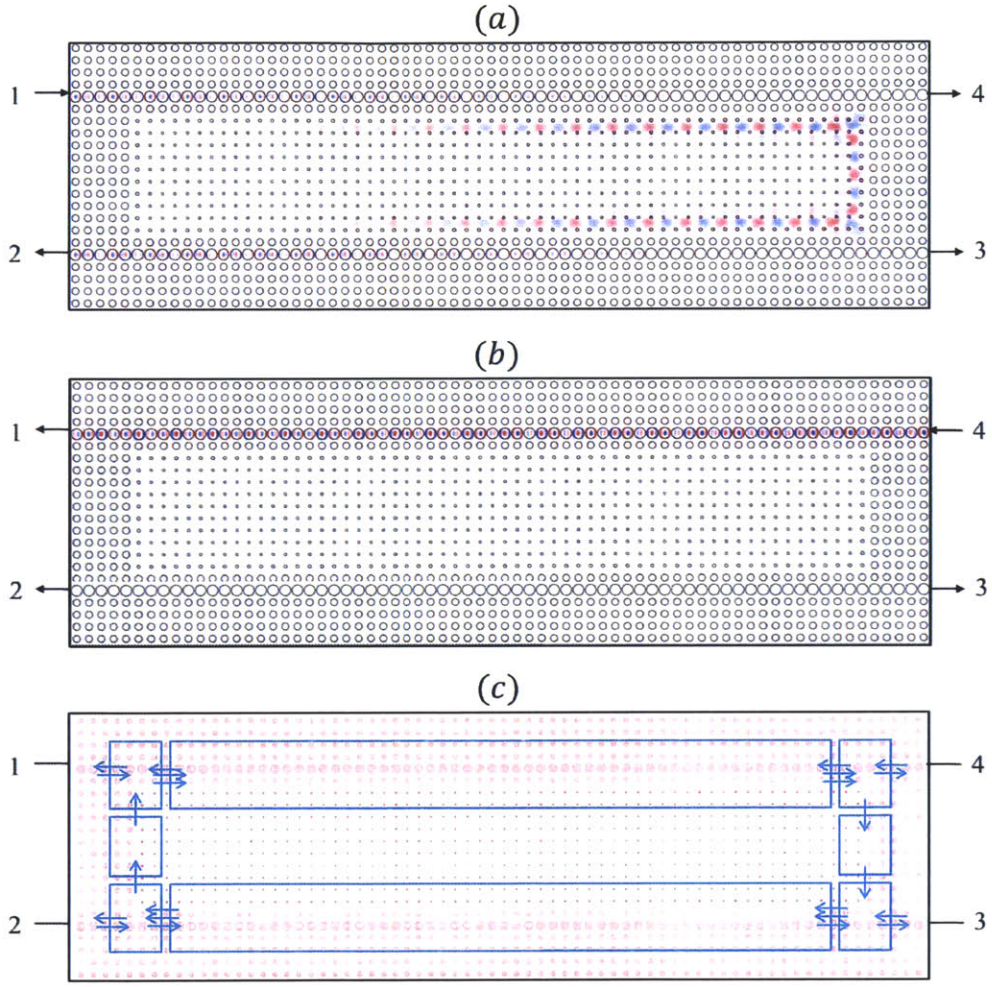

Figure 3-8: Four-port circulator. (a) Steady-state electrical-field distribution of a four-port circulator excited from Port 1 at $\omega = 0.548(2\pi c/a)$, with full transmission to Port 2. (b) Steady-state field distribution with excitation from Port 4 at $\omega = 0.548(2\pi c/a)$. Full transmission is seen at Port 1. (c) Scattering matrix decomposition of the four-port circulator.

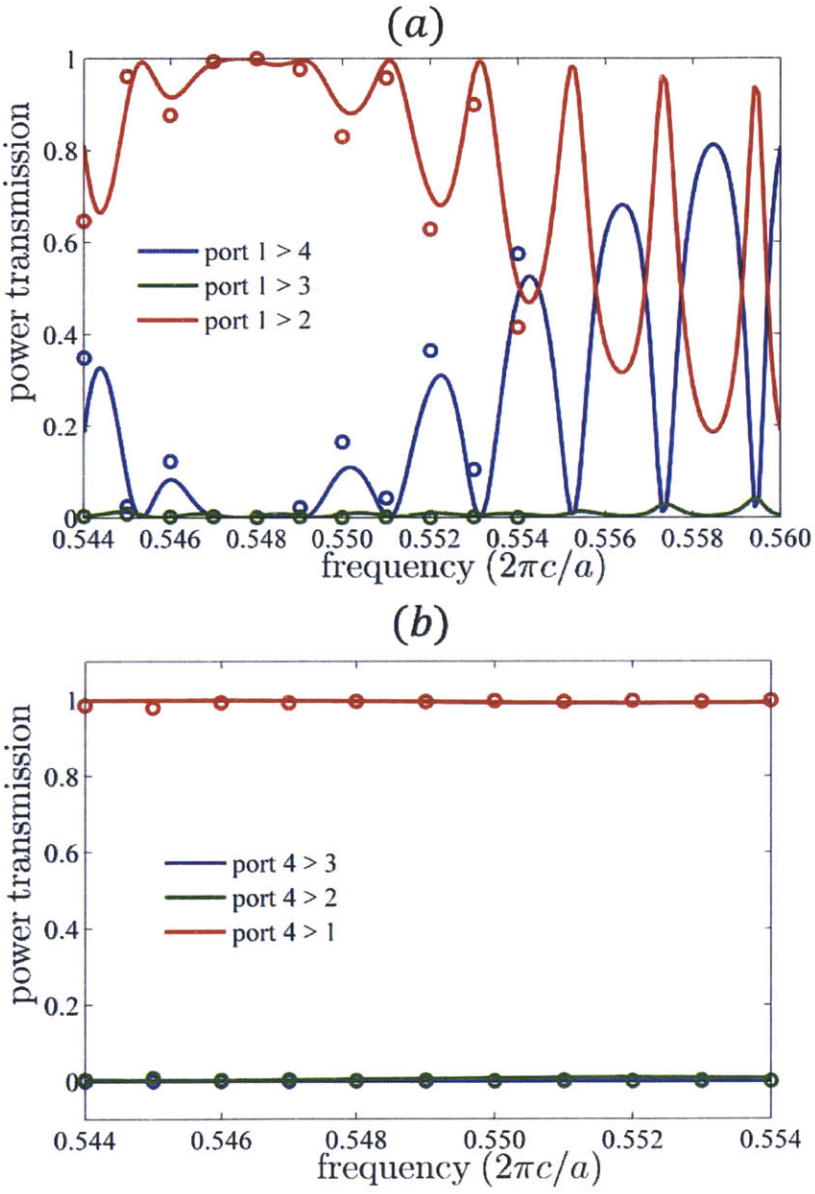

Figure 3-9: The transmission spectra of the four-port circulator. Finite element simulation (curves) shows good agreement with scattering matrix calculation (circles). The input is at Port 1 in (a) and Port 4 in (b).

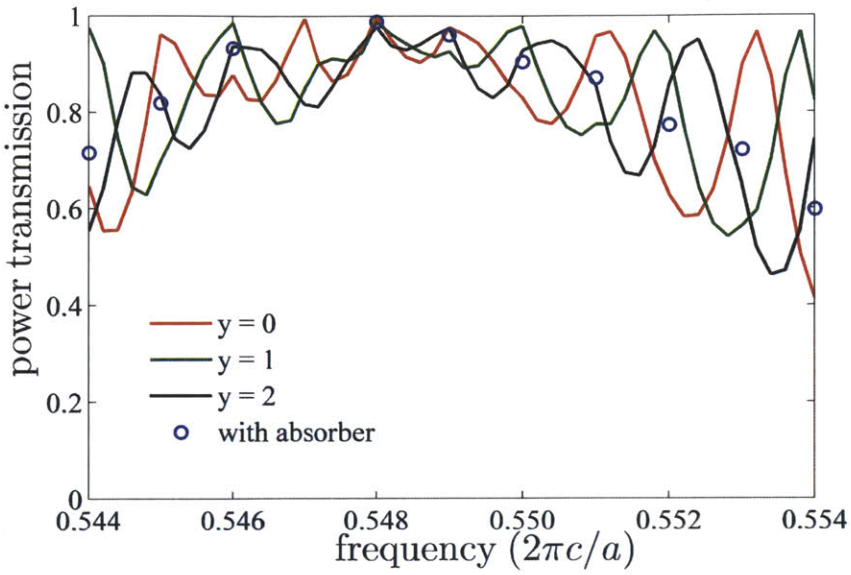

Figure 3-10: The calculated transmission spectra for three circulators with various lengths for the vertical sections of the one-way waveguide (curves) and the calculated transmission spectrum when an absorber is inserted in the one-way waveguide between Port 1 and Port 2 (circles).

vertical sections of a single-mode waveguide (one-way waveguide), as shown in Fig. 3-8(c). Since we already know the scattering matrix of the corner and the dispersion relation of the waveguide coupler from previous analysis, the total scattering matrix of the four-port circulator can be calculated analytically by simple matrix calculations.

Since the waveguide coupler provides a bandwidth of around 2%, one might expect a similar drop in power transmission between the ports when the frequency is detuned from the optimal value. The calculated transmission spectrum (Fig. 3-9(a)) indeed exhibits a relative bandwidth of 1.3%, where the pass-band ripple is found to be less than 1dB. However, large transmission still occurs at a discrete set of frequencies far detuned from the optimal, even when the waveguide couplers do not provide complete power transfer. At these frequencies, residual power exists and circulates in the one-way waveguide, in contrast to the ideal case where residual power vanishes after propagating through both waveguide couplers (Fig. 3-8(a)). With the circulating residual power, the entire stretch of the one-way waveguide functions as a ring

resonator, where complete transmission occurs when the phase accumulated through the entire one-way ring is an integer multiple of 2π. We verified this observation by changing the length of the vertical section of the one-way waveguides L_y and found the transmission peaks shift in frequency (Fig. 3-10), commensurate with ring resonator interpretation. The notable exception is found at the optimal frequency of $0.548(2\pi c/a)$, where the peak frequency is unaffected by L_y, consistent with a lack of residual power and the absence of the ring resonance. Further agreement is found in the simulation with a perfect absorber inserted in the left vertical section of the one-way waveguide (Fig. 3-10). In that case, the circulating power is shut off completely, resulting in the disappearance of the oscillation.

We note that such waveguide-coupler based circulators, in both three-port and four-port forms, can eventually provide much greater bandwidth, when one optimizes the dispersion relation of the underlying one-way and two-way waveguides. Here both the geometry of the photonic crystals and the frequency-dependent gyromagnetic tensor elements affect the dispersion. The incomplete transmission at detuned frequencies could originate from the reflection from the 90 degree bend or a non-ideal waveguide coupling. However, since the aggregated transmission to Port 2 for the three-port circulator (Fig. 3-7(a)) and the aggregated transmission to Port 2 for the four-port circulator (Fig. 3-9(a)) are both close to unity, the performance limitation is largely dominated by the waveguide coupler. There is also a trade-off between the bandwidth and the length of the waveguide coupler in this proof-of-concept structure. However, given the large degree of freedom in dispersion engineering for photonic crystals, by varying the dimension and the shape of the nearest unit cells to the waveguides, one could in principle match the uncoupled dispersion relations of the two waveguides over a much broader range of the frequency. In other words, equalizing the propagation constant and the frequency of the two waveguides could allow us to create ideal circulators over a frequency range close to the entire photonic bandgap. Moreover, increasing the coupling coefficient κ by physically merging the two-way waveguide and the one-way waveguide could reduce the interaction length, thereby reducing the overall device dimension significantly. With the emergence of

novel infrared magneto-optical materials featuring the Voigt parameter comparable to microwave ferrites [62,63] envision the experimental demonstration of such broadband circulator at optical frequencies.

3.6 Concluding remarks

In this chapter, we proposed a novel optical circulator based on directional couplers between a one-way waveguide and a two-way waveguide. We examined the bandwidth limit of such a waveguide coupler and its impact on the derived three-port circulators and four-port circulators. The bandwidth is not limited by the resonant linewidth and a three-port circulator and a four-port circulator are implemented numerically to feature a relative 1dB -bandwidth of 2% and 1.3% respectively. While our discussion has been restricted to two-dimensional structures, the operational principle and design procedures can be readily extended to three-dimensional structures at microwave, THz and optical frequencies, using out-of-plane confinement employed in experimental three-dimensional chiral edge state systems [55].

Chapter 4

A General Framework of Calculating SBS Gain

4.1 Introduction

Stimulated Brillouin Scattering (SBS) is a third order nonlinear process in which two optical modes are coupled through an elastic mode [5, 6]. In a waveguide system, the interference of pump and Stokes waves generates a time-varying optical force at the beat frequency. The optical force, while at resonance with an elastic mode at the phase-matching wavevector, excites the mechanical vibration of the waveguide, which can in turn scatter light between the pump and Stokes waves. Since its discovery, SBS has been extensively studied with a variety of applications in efficient phonon generation [64,65], optical frequency conversion [66–68], slow light [69–72], and signal processing techniques [73, 74].

The optical force that mediates SBS includes electrostriction force and radiation pressure [75, 76]. Electrostriction is an intrinsic material nonlinearity, which arises from the tendency of materials to become compressed in the region of high optical intensity. In previous studies, electrostriction is treated as a bulk nonlinearity with only electrostriction body force taken into account [5, 6]. We find that the discontinuities of optical intensities and photoelastic constants can generate electrostriction pressure on material boundaries. Radiation pressure is another boundary nonlinearity, which

arises from the interaction of light with the material boundaries with discontinuous dielectric constant [77, 78]. For nanoscale structures, radiation pressure is radically enhanced, enabling a variety of optomechanics applications [79–84]. Within nanoscale waveguides, the distributions of electrostriction force and radiation pressure are quite different. The interplay between these two effects creates new degree of freedoms of tailoring SBS process.

In translationally invariant waveguides, SBS can be categorized into forward SBS (FSBS) and backward SBS (BSBS). In FSBS, the pump and Stokes waves propagate in the same direction, generating translationally invariant optical forces, which excite standing elastic modes [67]. In BSBS, the pump and Stokes waves propagate in the counter directions, generating translationally varying optical forces, which excite traveling elastic modes.

In translationally periodic waveguides, SBS can still be categorized into FSBS and BSBS based on the Bloch wavevectors of the pump and Stokes waves. One important feature brought by the periodicity is that the optical group velocity vanishes at the Brillouin zone boundary [1]. Within this slow light regime, photon-phonon interaction becomes extremely strong, creating a giant enhancement of SBS nonlinearity.

SBS can also occur between distinct optical modes [85–89]. The interplay between optical modes with distinct polarizations, symmetries, and distributions enrich the tailorability of SBS nonlinearities. Intermode SBS has been used in optical signal isolation and Brillouin cooling of mechanical devices.

The strength of SBS nonlinearity is characterized by the SBS gain. There have been many theoretical studies on calculating SBS gain through some forms of overlap integral between optical and elastic eigen-modes [5,6,67,85,88–92]. These treatments, while accurate for microscale waveguides, suffer from two drawbacks for nanoscale waveguides. First, most previous treatments are based on nonlinear polarization current. The calculated SBS gain only captures electrostriction body forces, but doesn't account for boundary nonlinearities such as electrostriction pressure and radiation pressure. This issue becomes significant for nanoscale waveguides where the boundary effect is radically enhanced. Second, some previous studies assume the optical

mode is linearly polarized, while some studies describe the elastic modes by the density modulation rather than the displacement vector. For nanoscale waveguides, the vector nature of optical and elastic modes has to be fully evaluated.

In this chapter, we propose a general method of calculating SBS gains via the overlap integral between optical and elastic eigen-modes. Within this formalism, all kinds of optical forces are taken into account, with bulk and boundary nonlinearities formulated as bulk and boundary integrals over the waveguide cross-section. In addition, both the optical and elastic modes are treated as vector fields, allowing for the most general forms of dielectric and elastic tensors.

Armed with this formalism, we study the SBS process of a silicon rectangular waveguide. We will show that all the optical forces in FSBS are transverse, and the constructive combination of electrostriction force and radiation pressure can generate large FSBS gain for certain elastic modes. In contrast, the optical force in BSBS is largely longitudinal, and the maximal BSBS gain among all the elastic modes approaches the conventional BSBS gain. We further apply this formalism to intermode SBS. By coupling optical modes with distinct symmetries, optical forces with all possible symmetries can be generated, and the elastic modes with the same symmetry can be excited. We also study the FSBS process when the silicon waveguide is put on top of a silica substrate. Both the frequency response calculation and leaky eigen-mode analysis reveal that the coupling to the radiative modes of the substrate introduces a large radiative loss which significantly reduces the SBS gain of the structure.

Based on the understanding of SBS gains of a rectangular waveguide, in this chapter, we proceed to study the SBS process of a translationally periodic waveguide. We demonstrate that SBS gain can be further enhanced at the Brillouin zone boundary where the decreased group velocity of light significantly magnifies photon-phonon interaction. In addition, we find that the geometric symmetry plane perpendicular to the propagation axis plays an important role in both FSBS and BSBS. This plane separates standing elastic modes into even and odd modes. For FSBS, only even modes have nonzero SBS gains. For BSBS, the SBS gain of even modes approaches to infinity, while the SBS gain of odd modes approaches to a constant.

4.2 An overlap integral formula of SBS gains

To start with, we develop a general framework of calculating the SBS gain. Consider a translationally invariant waveguide in x direction. In a typical SBS process, the pump wave $\mathbf{E}_p e^{i(k_p x - \omega_p t)}$ and the Stokes wave $\mathbf{E}_s e^{i(k_s x - \omega_s t)}$ generate optical forces at the phase-matching wavevector $q = k_p - k_s$ and the beat frequency $\Omega = \omega_p - \omega_s$. This optical force can excite mechanical vibrations which enables the parametric conversion between pump and Stokes waves. This process can be describe by the following relation [5]:

$$\frac{dP_s}{dx} = gP_pP_s - \alpha_s P_s \tag{4.1}$$

Here, P_p and P_s are the guided power of the pump and Stokes waves, and g is the SBS gain. Through particle flux conservation, SBS gain is given by the following formula [76]:

$$g(\Omega) = \frac{\omega_s}{2\Omega P_p P_s} \Re \left\langle \mathbf{f}, \frac{d\mathbf{u}}{dt} \right\rangle \tag{4.2}$$

where $\mathbf{f}$ is the optical force generated by pump and Stokes waves, and $\mathbf{u}$ is the elastic response of the waveguide induced by $\mathbf{f}$. The overlap integral is defined over the waveguide cross-section. The optical power of an invariant waveguide is given by $P = v_g \langle \mathbf{E}, \epsilon \mathbf{E} \rangle / 2$, where v_g is the optical group velocity. Therefore,

$$g(\Omega) = \frac{2\omega_s}{v_{gp} v_{gs}} \frac{\Im \langle \mathbf{f}, \mathbf{u} \rangle}{\langle \mathbf{E}_p, \epsilon \mathbf{E}_p \rangle \langle \mathbf{E}_s, \epsilon \mathbf{E}_s \rangle} \tag{4.3}$$

To further simply (4.3), we have to consider the equation governing the elastic response $\mathbf{u}e^{-i\Omega t}$ under external forces $\mathbf{f}e^{-i\Omega t}$. When elastic loss are ignored, we have [93]:

$$-\rho \Omega^2 u_i = \frac{\partial}{\partial x_j} c_{ijkl} \frac{\partial u_l}{\partial x_k} + f_i \tag{4.4}$$

where ρ is the mass density, and c_{ijkl} is the elastic tensor. c_{ijkl} has two important properties. First, it is symmetric about the first two and last two indies: $c_{ijkl} = c_{jikl}$, $c_{ijlk} = c_{ijkl}$. Second, the interchange of the first two indies and the last two does not affect the value of c_{ijkl}: $c_{klij} = c_{ijkl}$ [93]. Without $\mathbf{f}$, the equation above is the elastic

eigen-equation:

$$-\Omega^2 \rho u_i = \frac{\partial}{\partial x_j} c_{ijkl} \frac{\partial u_l}{\partial x_k} \tag{4.5}$$

Using the symmetry properties of c_{ijkl}, we can show that the operator in the right hand side of the eigen-equation is Hermitian. Therefore, the eigen-mode $\mathbf{u}_m e^{-i\Omega_m t}$ satisfies orthogonality condition:

$$\langle \mathbf{u}_m, \rho \mathbf{u}_n \rangle = \delta_{mn} \langle \mathbf{u}_m, \rho \mathbf{u}_m \rangle \tag{4.6}$$

When $\mathbf{f}$ is present, $\mathbf{u}$ can be decomposed in terms of eigen-modes $\mathbf{u} = \sum_m b_m \mathbf{u}_m$. Using the orthogonality condition, we have:

$$b_m = \frac{\langle \mathbf{u}_m, \mathbf{f} \rangle}{\langle \mathbf{u}_m, \rho \mathbf{u}_m \rangle} \frac{1}{\Omega_m^2 - \Omega^2} \tag{4.7}$$

Now we add elastic loss to this system. The commonly encountered elastic loss mechanism are air damping, thermoelastic dissipation, and clamping losses [94]. The first order effect of loss can be captured by changing Ω_m to $\Omega_m - i\Gamma_m/2$. Assuming quality factor $Q_m = \Omega_m/\Gamma_m$ is well above 1, we have,

$$b_m = \frac{\langle \mathbf{u}_m, \mathbf{f} \rangle}{\langle \mathbf{u}_m, \rho \mathbf{u}_m \rangle} \frac{1}{\Omega_m \Gamma_m} \frac{\Gamma_m/2}{\Omega_m - \Omega - i\Gamma_m/2} \tag{4.8}$$

Inserting (4.8) into (4.3), we can see that the total SBS gain is the sum of SBS gains of individual elastic modes.

$$g(\Omega) = \sum_m G_m \frac{(\Gamma_m/2)^2}{(\Omega - \Omega_m)^2 + (\Gamma_m/2)^2} \tag{4.9}$$

The SBS gain of a single elastic mode has a Lorentian shape and a peak value:

$$G_m = \frac{2\omega Q_m}{\Omega_m^2 v_{gp} v_{gs}} \frac{|\langle \mathbf{f}, \mathbf{u}_m \rangle|^2}{\langle \mathbf{E}_p, \epsilon \mathbf{E}_p \rangle \langle \mathbf{E}_s, \epsilon \mathbf{E}_s \rangle \langle \mathbf{u}_m, \rho \mathbf{u}_m \rangle} \tag{4.10}$$

where we have used the fact that $\Omega \ll \omega_p, \omega_s$ and $\omega_p \approx \omega_s = \omega$.

For translationally periodic waveguides with axial periodicity a, (4.2) becomes:

$$g(\Omega) = \frac{\omega_s}{2\Omega P_p P_s a} \Re \left\langle \mathbf{f}, \frac{d\mathbf{u}}{dt} \right\rangle \tag{4.11}$$

Where the overlap integral is defined over the unit cell rather the waveguide cross-section. The optical power of a periodic waveguide is given by $P = v_g \langle \mathbf{E}, \epsilon \mathbf{E} \rangle / 2a$. Following same steps as invariant waveguides, we can show that (4.9) still holds. The maximal gain of individual modes becomes:

$$G_m = \frac{2\omega Q_m a}{\Omega_m^2 v_{gp} v_{gs}} \frac{|\langle \mathbf{f}, \mathbf{u}_m \rangle|^2}{\langle \mathbf{E}_p, \epsilon \mathbf{E}_p \rangle \langle \mathbf{E}_s, \epsilon \mathbf{E}_s \rangle \langle \mathbf{u}_m, \rho \mathbf{u}_m \rangle} \tag{4.12}$$

(4.10) and (4.12) provide a general method to calculate the SBS gain of a waveguide with arbitrary cross-section. Specifically, given the optical frequency ω, we can use finite element method to solve for the wavevectors and modal profiles of pump and Stokes waves. Then, we use finite element method to solve for the elastic modes at the phase-matching wavevector $q = k_p - k_s$. The SBS of each elastic mode can be calculated by taking the overlap integral between optical forces and elastic displacement. For translationally invariant waveguides, body forces and pressures form 2D and 1D integration respectively. For translationally periodic waveguides, body forces and pressures form 3D and 2D integration respectively.

(4.10) and (4.12) shows that the SBS gain is determined by the frequency ratio, the elastic loss factor, the optical group velocities, and the overlap integral between optical forces and elastic eigen-modes. In addition, (4.10) and (4.12) provide a way to separate the effects of various optical forces. Specifically, the overlap integral is the sum of all optical forces:

$$\langle \mathbf{f}, \mathbf{u}_m \rangle = \sum_n \langle \mathbf{f}_n, \mathbf{u}_m \rangle \tag{4.13}$$

The amplitudes of individual overlap integrals determine contributions from different optical forces, while their relative phases determine the interference effect.

4.3 Calculation of optical forces

A key step of applying (4.10) and (4.12) is to calculate optical forces from pump and Stokes waves. Throughout the study, we consider electrostriction force and radiation pressure. In this section, we summarize the calculation of these optical forces for both translationally invariant and periodic waveguides. Note that we are interested in the time-varying optical forces. The computed optical force is the complex amplitude which encodes the strength and phase distribution. This is different from static optical force which is always real.

4.3.1 Electrostriction force

Electrostriction forces are derived from electrostriction tensor. The instantaneous electrostriction tensor is given by:

$$\sigma_{ij} = -\frac{1}{2}\epsilon_0 n^4 p_{ijkl} E_k E_l \tag{4.14}$$

where n is the refractive index, and p_{ijkl} is the photoelastic tensor [95].

For translationally invariant waveguides, the total electric field is given by

$$\mathbf{E} = (\mathbf{E}_p e^{i(k_p x - \omega_p t)} + \mathbf{E}_s e^{i(k_s x - \omega_s t)})/2 + c.c \tag{4.15}$$

Inserting this expression to (4.14), and filtering out the components with frequency Ω, we get the time-harmonic electrostriction tensor $\sigma_{ij} e^{i(qx - \Omega t)}$:

$$\sigma_{ij} = -\frac{1}{4}\epsilon_0 n^4 p_{ijkl}(E_{pk} E^*_{sl} + E_{pl} E^*_{sk}) \tag{4.16}$$

For simplicity, we assume that the crystal structure of the waveguide material is symmetric about $x = 0$, $y = 0$, and $z = 0$. Therefore, p_{ijkl} is zero if it contains odd

number of a certain component. In compact notation, (4.16) can be written as:

$$\begin{bmatrix} \sigma_{xx} \\ \sigma_{yy} \\ \sigma_{zz} \\ \sigma_{yz} \\ \sigma_{xz} \\ \sigma_{xy} \end{bmatrix} = -\frac{1}{2}\epsilon_0 n^4 \begin{bmatrix} p_{11} & p_{12} & p_{13} & & & \\ p_{12} & p_{22} & p_{23} & & & \\ p_{13} & p_{23} & p_{33} & & & \\ & & & p_{44} & & \\ & & & & p_{55} & \\ & & & & & p_{66} \end{bmatrix} \begin{bmatrix} E_{px}E_{sx}^* \\ E_{py}E_{sy}^* \\ E_{pz}E_{sz}^* \\ E_{py}E_{sz}^* + E_{pz}E_{sy}^* \\ E_{px}E_{sz}^* + E_{pz}E_{sx}^* \\ E_{px}E_{sy}^* + E_{py}E_{sx}^* \end{bmatrix} \tag{4.17}$$

Electrostriction force is given by the divergence of electrostriction tensor. In a system consisting of homogeneous materials, electrostriction forces can exist inside each material (electrostriction body force) and on the interfaces (electrostriction pressure). Electrostriction body force is $\mathbf{f}^{ES}e^{i(qx-\Omega t)}$:

$$\begin{aligned} f_x^{ES} &= -iq\sigma_{xx} - \partial_y\sigma_{xy} - \partial_z\sigma_{xz} \\ f_y^{ES} &= -iq\sigma_{xy} - \partial_y\sigma_{yy} - \partial_z\sigma_{yz} \\ f_z^{ES} &= -iq\sigma_{xz} - \partial_y\sigma_{zy} - \partial_z\sigma_{zz} \end{aligned} \tag{4.18}$$

Electrostriction pressure on the interface between material 1 and 2 is given by $\mathbf{F}^{ES}e^{i(qx-\Omega t)}$ (normal vector n points from 1 to 2):

$$F_i^{ES} = (\sigma_{1ij} - \sigma_{2ij})n_j \tag{4.19}$$

Under a particular phase, the optical mode of the waveguide $\mathbf{E}e^{i(kx-\omega t)}$ have imaginary E_x and real $E_{y,z}$. From (4.17), we can see that σ_{xx}, σ_{yy}, σ_{zz}, and σ_{yz} are real while σ_{xy} and σ_{xz} are imaginary. From (4.18) and (4.19), we can see that for both electrostriction body force and electrostriction pressure, the transverse component is real while the longitudinal component is imaginary.

For translationally periodic waveguides, the total electric field is given by

$$\mathbf{E} = (\mathbf{E}_p e^{-i\omega_p t} + \mathbf{E}_s e^{-i\omega_s t})/2 + c.c \tag{4.20}$$

Inserting this expression to (4.14), and taking out the components with frequency Ω, we get the time-harmonic electrostriction tensor $\sigma_{ij}e^{-i\Omega t}$:

$$\sigma_{ij} = -\frac{1}{4}\epsilon_0 n^4 p_{ijkl}(E_{pk}E^*_{sl} + E_{pl}E^*_{sk}) \tag{4.21}$$

Similar to invariant waveguides, electrostriction body force is given by $\mathbf{f}^{ES}e^{-i\Omega t}$:

$$f_i^{ES} = -\partial_j \sigma_{ij} \tag{4.22}$$

Electrostriction pressure is given by $\mathbf{F}^{ES}e^{-i\Omega t}$:

$$F_i^{ES} = (\sigma_{1ij} - \sigma_{2ij})n_j \tag{4.23}$$

Electrostriction pressure can have tangent components on the interface.

4.3.2 Radiation pressure

Radiation pressure is derived from Maxwell Stress Tensor (MST). For a dielectric system ($\mu = 1$) without free charges ($\rho = 0, J = 0$), radiation pressure is localized where the gradient of ϵ is nonzero [96, 97]. For a system consisting of homogeneous materials, radiation pressure only exists on the interfaces. The dielectric part of instantaneous MST is:

$$T_{ij} = \epsilon_0 \epsilon (E_i E_j - \frac{1}{2}\delta_{ij}E^2) \tag{4.24}$$

The instantaneous pressure on the interface between material 1 and 2 is:

$$F_i^{RP} = (T_{2ij} - T_{1ij})n_j \tag{4.25}$$

By decomposing the electric field into its normal and tangent components $\mathbf{E} = E_n\mathbf{n} + E_t\mathbf{t}$, and using the boundary condition $\epsilon_1 E_{1n} = \epsilon_2 E_{2n} = D_n$ and $E_{1t} = E_{2t} = E_t$, we can show that:

$$\mathbf{F}^{RP} = -\frac{1}{2}\epsilon_0 E_t^2(\epsilon_2 - \epsilon_1)\mathbf{n} + \frac{1}{2}\epsilon_0^{-1} D_n^2(\epsilon_2^{-1} - \epsilon_1^{-1})\mathbf{n} \tag{4.26}$$

For translationally invariant waveguides, the time-harmonic radiation pressure is $\mathbf{F}^{RP}e^{i(qx-\Omega t)}$:

$$\mathbf{F}^{RP} = -\frac{1}{2}\epsilon_0 E_{pt}E^*_{st}(\epsilon_2 - \epsilon_1)\mathbf{n} + \frac{1}{2}\epsilon_0^{-1}D_{pn}D^*_{sn}(\epsilon_2^{-1} - \epsilon_1^{-1})\mathbf{n} \tag{4.27}$$

(4.27) shows that radiation pressure is transverse and real.

For translationally periodic waveguides, the time-harmonic radiation pressure is $\mathbf{F}^{RP}e^{-i\Omega t}$ with $\mathbf{F}^{RP}$ given by (4.27). Radiation pressure is always in the normal direction.

4.3.3 Convergence to the conventional BSBS gain

Combining (4.10) and (4.12) with the calculation of optical forces, we are ready to explore the SBS nonlinearity of nanoscale waveguides. Before that, it is instructive to compare (4.10) with the conventional BSBS gain [6]. We can show that (4.10) converges to the conventional BSBS gain under plane-wave approximations for both optical and elastic modes. Specifically, consider the coupling between two counter propagating optical plane-waves through an elastic plane-wave. The optical plane-wave is linearly polarized in y direction. The elastic plane-wave is pure longitudinal traveling at velocity V_L. Under this setup, nonzero optical forces include the longitudinal electrostriction body force, and the transverse components of electrostriction pressure and radiation pressure. Only the longitudinal electrostriction body force contributes nonzero overlap integral:

$$f_x^{ES} = -iq\sigma_{xx} = \frac{1}{2}iq\epsilon_0 n^4 p_{12}E_y^2 \tag{4.28}$$

Inserting this expression into (4.10), and using the fact that $\Omega = qV_L$ and $q = 2k$, we can show that:

$$G_0 = \frac{\omega^2 n^7 p_{12}^2}{c^3 \rho V_L \Gamma}\frac{1}{A} \tag{4.29}$$

Where A is the cross-sectional area of the waveguide. This is exactly the conventional BSBS gain. For microscale waveguides, the plane-wave approximation is valid,

and (4.10) converges to G_0. For nanoscale waveguides, (4.10) can deviate from G_0 significantly because of the vector nature of optical and elastic modes as well as the enhanced boundary nonlinearities.

4.4 Translationally invariant waveguides

4.4.1 Silicon rectangular waveguides

In this section, we apply the general formalism to study the SBS process of a translationally invariant waveguide. Consider a silicon rectangular waveguide suspended in air (Fig. 4-1 insert). The cross-section is a by $0.9a$. For silicon, we use refractive index $n = 3.5$, Young's modulus $E = 170 \times 10^9$ Pa, Poisson's ratio $\nu = 0.28$, and density $\rho = 2329\text{kg/m}^2$. In addition, we assume that the [100], [010], and [001] symmetry direction of this crystalline silicon coincide with the x, y, and z axis respectively. Under this orientation, the photo-elastic tensor p_{ijkl} in contracted notation is $[p_{11}, p_{12}, p_{44}] = [-0.09, 0.017, -0.051]$ [98]. The structure has two symmetry plane $y = 0$ and $z = 0$. Both optical modes and elastic modes have fixed parities about these planes.

The fundamental optical modes are E_{y11} and E_{z11} (Fig. 4-1(a)). E_{y11} is even about $z = 0$ and odd about $y = 0$ with a large E_y component. E_{z11} has the opposite parities and slightly higher frequencies. Throughout the study, we assume the pump wavelength is 1.55μm. So a is the product of 1.55μm and ω in unit of $2\pi c/a$, and different operating point in the dispersion diagram corresponds to different a. For FSBS and BSBS, we assume that pump and Stokes waves come from E_{y11}. Since $\Omega/\omega \approx V_L/c$ is on the order of 10^{-4}, pump and Stokes waves approximately corresponds to the same mode $\mathbf{E}e^{i(kx-\omega t)}$. The optical force induced by intramode coupling is always symmetric about both $y = 0$ and $z = 0$.

We only consider elastic modes with the same parities (Fig. 4-1(b)). Here, E-modes are the actual eigen-modes, while P-modes (S-modes) are the constrained eigen-modes with pure longitudinal (transverse) displacement. At $q = 0$, the geo-

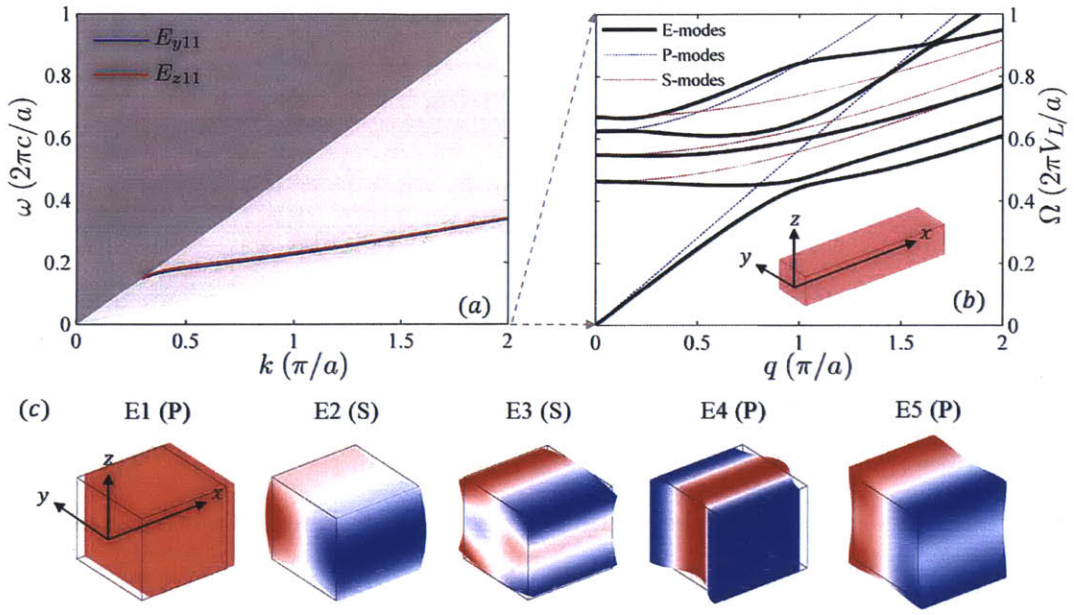

Figure 4-1: The optical and elastic modes of a silicon rectangular waveguide. Optical frequency is in unit of $2\pi c/a$, while elastic frequency is in unit of $2\pi V_L/a$. $V_L = \sqrt{E/\rho} = 8.54 \times 10^3$m/s is the longitudinal sound velocity of silicon. (a) Dispersion diagram of optical modes E_{y11} and E_{z11}. (b) Dispersion diagram of elastic modes which are even about both $y = 0$ and $z = 0$. E-modes (black lines) are the actual eigen-modes. P-modes (blue lines) are the constrained eigen-modes with only longitudinal movements. S-modes (red lines) are the constrained eigen-modes with only transverse movement. At $q = 0$, E-modes are either P-modes or S-modes. (c) The modal profiles of E1 through E5 at $q = 0$. The deformation is proportional to the displacement. The color represents u_y for S-modes and u_x for P-modes. Blue, white, and red correspond negative, zero, and positive values respectively. E1 corresponds to a longitudinal shift.

metric symmetry plane $x = 0$ is recovered. Elastic modes that are odd (even) about this plane only have longitudinal (transverse) movement. Therefore, elastic modes at $q = 0$ are pure P-modes or S-modes (Fig. 4-1(c)). Elastic modes at nonzero q are hybrid. Similar to the optical mode, we can choose a proper phase so that u_x is imaginary while $u_{y,z}$ are real.

4.4.2 Forward SBS

In FSBS, $\mathbf{E}_p = \mathbf{E}_s = \mathbf{E}$ and $q = 0$. (4.17) can be simplified to:

$$\begin{bmatrix} \sigma_{xx} \\ \sigma_{yy} \\ \sigma_{zz} \\ \sigma_{yz} \\ \sigma_{xz} \\ \sigma_{xy} \end{bmatrix} = -\frac{1}{2}\epsilon_0 n^4 \begin{bmatrix} p_{11} & p_{12} & p_{13} & & & \\ p_{12} & p_{22} & p_{23} & & & \\ p_{13} & p_{23} & p_{33} & & & \\ & & & p_{44} & & \\ & & & & p_{55} & \\ & & & & & p_{66} \end{bmatrix} \begin{bmatrix} |E_x|^2 \\ |E_y|^2 \\ |E_z|^2 \\ 2\Re(E_y E_z^*) \\ 0 \\ 0 \end{bmatrix} \tag{4.30}$$

Therefore, $\sigma_{xy} = \sigma_{xz} = 0$. From (4.18) and (4.19), we can see that $f_x^{ES} = F_x^{ES} = 0$. So both electrostriction force and radiation pressure in FSBS are transverse. We pick an operating point at $\omega = 0.203(2\pi c/a)$, $k = 0.75(\pi/a)$ with $a = 315$nm, and compute the force distribution (Fig. 4-2(a)). Electrostriction body force is largely in y direction. This is because E_y is the dominant component in electric field and $|p_{11}|$ is about five times larger than $|p_{12}|$. Electrostriction pressure points inwards. Radiation pressure points outwards. Radiation pressure is about five times larger than electrostriction pressure.

The transverse nature of optical force combined with the fact that elastic modes are either P-modes or S-modes at $q = 0$ indicates that only S-modes have nonzero FSBS gains. We compute the corresponding FSBS gains using a quality factor $Q = 1000$ for all the elastic modes (Fig. 4-2(b)). As expected, only S-modes E2, E3, and E5 have nonzero gains. E2 has the largest gain of $1.72 \times 10^4 \mathrm{m}^{-1}\mathrm{W}^{-1}$, which comes from a constructive combination of electrostriction force ($0.42 \times 10^4 \mathrm{m}^{-1}\mathrm{W}^{-1}$) and radiation

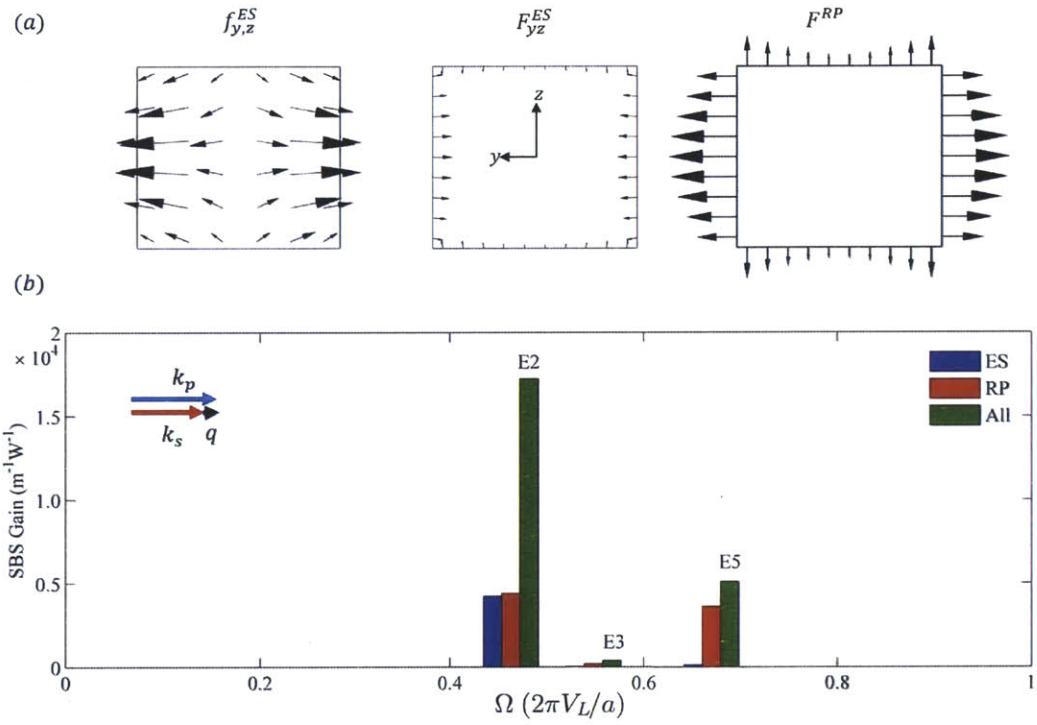

Figure 4-2: Detailed analysis of FSBS. For (a) and (b), the operating point is $\omega = 0.203(2\pi c/a)$, $k = 0.75(\pi/a)$, and $q = 0$ with $a = 315$nm. (a) The distribution of optical forces. All optical forces are transverse. (b) FSBS gains calculated from overlap integral using $Q = 1000$. Blue, red, and green bars represent FSBS gains from electrostriction force, radiation pressure, and both. Only S-modes have non-zero gains. (c) The scaling of FSBS gains as a varies from 0.25μm to 2.5μm. Solid and dotted lines represent E2 and E5 respectively.

pressure ($0.44 \times 10^4 \mathrm{m}^{-1}\mathrm{W}^{-1}$). E5 has a total gain of $0.51 \times 10^4 \mathrm{m}^{-1}\mathrm{W}^{-1}$, which mainly comes from radiation pressure ($0.36 \times 10^4 \mathrm{m}^{-1}\mathrm{W}^{-1}$).

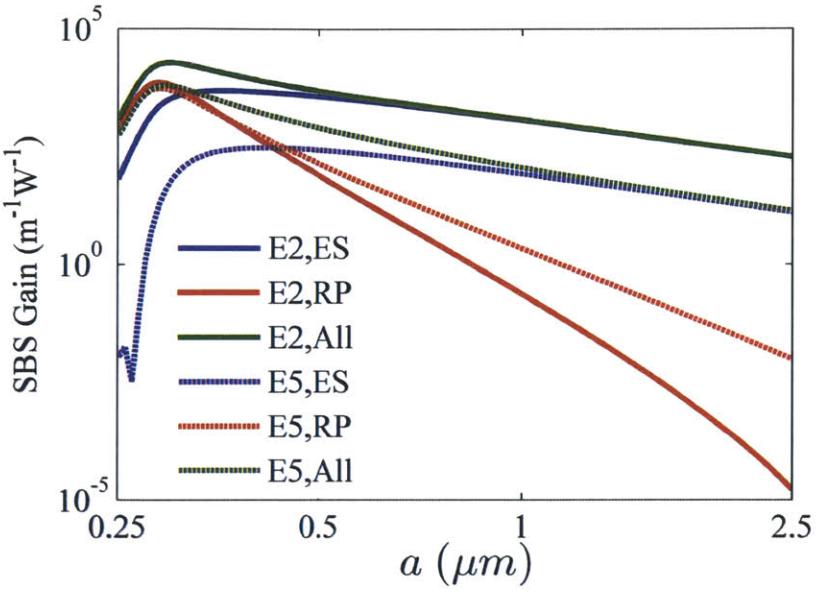

Figure 4-3: The scaling of FSBS gains as a varies from 0.25μm to 2.5μm. Solid and dotted lines represent E2 and E5 respectively.

Next, we vary a from 250nm to 2.5μm by lifting the operating point at the optical dispersion diagram from $0.16(2\pi c/a)$ to $1.61(2\pi c/a)$ and compute the corresponding FSBS gains for E2 and E5 (Fig. 4-3). For both E2 and E5, electrostriction FSBS gain scales as $1/a^2$ for large a. This can be understood by a detailed analysis of (4.10). Under normalization condition $\langle \mathbf{E}, \epsilon \mathbf{E} \rangle = 1$, the electrostriction tensor scales as $1/a^2$. Since electrostriction force is essentially the divergence of electrostriction tensor, the total electrostriction force that apply to the right half of the waveguide scales as $1/a^3$. Under normalization condition $\langle \mathbf{u}, \rho \mathbf{u} \rangle = 1$, $\mathbf{u}$ scales as $1/a$. So the overlap integral scales as $1/a^2$. Under a fixed Q, the electrostriction FSBS gain scales as $1/a^2$. The radiation pressure FSBS gain scales as $1/a^8$ for E2 and $1/a^6$ for E5. This can also be understood from a breakdown of (4.10). Given the input power, the sum of average pressure on the top and side boundaries of the rectangular waveguide is proportional to $(n_g - n_p)/A$, where n_g (n_p) is the group (phase) index, and A is the waveguide cross-section [78]. When the waveguide is scaled up with a fixed aspect ratio, $n_g - n_p$

shrinks in the order of $1/A$. So the sum of average radiation pressure scales as $1/a^4$, and the radiation pressure FSBS gains should scales as $1/a^6$. For E2, the radiation pressure on the side and top boundaries have opposite effects. So it is the difference rather than the sum between side and top radiation pressures that determines the overlap integral. This is why the radiation pressure induced FSBS gain of E2 decays faster.

4.4.3 Backward SBS

In BSBS, $\mathbf{E}_p = \mathbf{E}$, $\mathbf{E}_s = \mathbf{E}^*$, and $q = 2k$. (4.17) can be simplified to:

$$\begin{bmatrix} \sigma_{xx} \\ \sigma_{yy} \\ \sigma_{zz} \\ \sigma_{yz} \\ \sigma_{xz} \\ \sigma_{xy} \end{bmatrix} = -\frac{1}{2}\epsilon_0 n^4 \begin{bmatrix} p_{11} & p_{12} & p_{13} & & & \\ p_{12} & p_{22} & p_{23} & & & \\ p_{13} & p_{23} & p_{33} & & & \\ & & & p_{44} & & \\ & & & & p_{55} & \\ & & & & & p_{66} \end{bmatrix} \begin{bmatrix} E_x^2 \\ E_y^2 \\ E_z^2 \\ 2E_yE_z \\ 2E_xE_z \\ 2E_xE_y \end{bmatrix} \tag{4.31}$$

All components of σ_{ij} are nonzero, generating electrostriction force with both longitudinal and transverse components. We pick an operating point at $\omega = 0.203(2\pi c/a)$, $k = 0.75(\pi/a)$ with $a = 315$nm, and compute the force distribution (Fig. 4-4(a)). Electrostriction body force has large longitudinal component over the waveguide cross-section, which mainly comes from the $-iq\sigma_{xx}$ term in f_x^{ES}.

The hybrid nature of optical forces combined with the fact that all elastic modes are hybrid at nonzero q indicates that all elastic modes have nonzero gains. We compute the corresponding BSBS gains using a quality factor $Q = 1000$ for all the elastic modes (Fig. 4-4(b)). For E1 and E2, electrostriction force and radiation pressure add up destructively, resulting small BSBS gains of $0.089 \times 10^4 \text{m}^{-1}\text{W}^{-1}$ and $0.086 \times 10^4 \text{m}^{-1}\text{W}^{-1}$ respectively.

Next, we vary a from 250nm to 2.5μm and compute the corresponding BSBS gains for E1 and the conventional BSBS gain G_0 (Fig. 4-5). The electrostriction

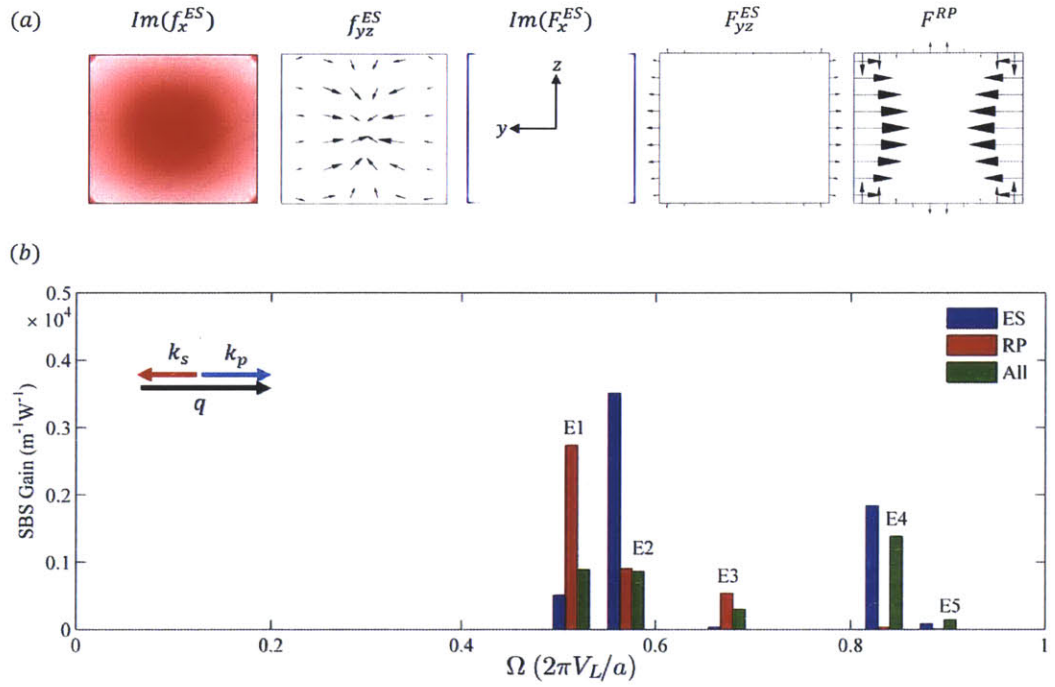

Figure 4-4: Detailed analysis of BSBS. For (a) and (b), the operating point is $\omega = 0.203(2\pi c/a)$, $k = 0.75(\pi/a)$, and $q = 1.5(\pi/a)$ with $a = 315$nm. (a) The distribution of optical forces. Electrostriction forces have both longitudinal and transverse components. Radiation pressure has only transverse component. (b) BSBS gains calculated from overlap integral using $Q = 1000$. Blue, red, and green bars represent BSBS gains from electrostriction force, radiation pressure, and both. (c) The scaling of BSBS gains as a varies from 0.25μm to 2.5μm. Blue, red, and green lines represents different BSBS gains of E1. Solid black line represents the conventional BSBS gain. Dotted black line represents the electrostriction BSBS gain of P1. Black dots represents the maximal electrostriction BSBS gain of all E-modes.

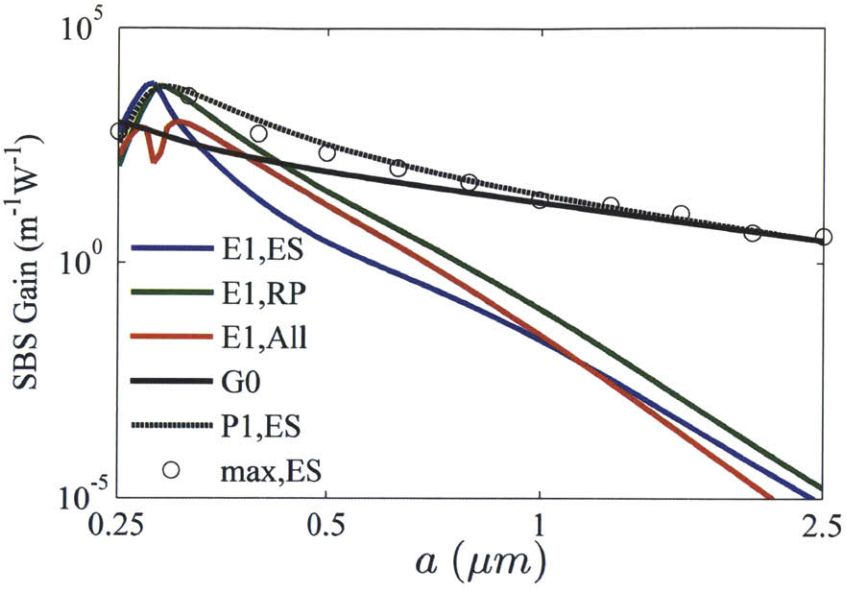

Figure 4-5: The scaling of BSBS gains as a varies from 0.25μm to 2.5μm. Blue, red, and green lines represents different BSBS gains of E1. Solid black line represents the conventional BSBS gain. Dotted black line represents the electrostriction BSBS gain of P1. Black dots represents the maximal electrostriction BSBS gain of all E-modes.

BSBS gain of E1 decays very fast. In contrast, G_0 scales as $1/a^2$ as indicated by (4.29). This difference comes from the fact that the conventional BSBS gain corresponds to the longitudinal plane wave, but E1 quickly deviates from longitudinal plane wave as the dimensionless q increases (Fig. 4-1(b)). There are two ways to recover the conventional BSBS gain from (4.10). First, we consider the constrained longitudinal modes (P-modes) in Fig. 4-1(b). P1 is just the longitudinal plane wave. The computed electrostriction BSBS for P1 converges to G_0 as a increases (Fig. 4-5). Second, the dispersion curve of P1 pass through different E-modes as the dimensionless q increases. The E-modes at the intersection points become P1-like with large longitudinal movement over the waveguide cross-section. These modes should have a large electrostriction BSBS gain close to that of P1. We compute the electrostriction BSBS gains for E1 through E500 for different a (Fig. 4-5). The maximal gain among all the modes converges to G_0 as expected.

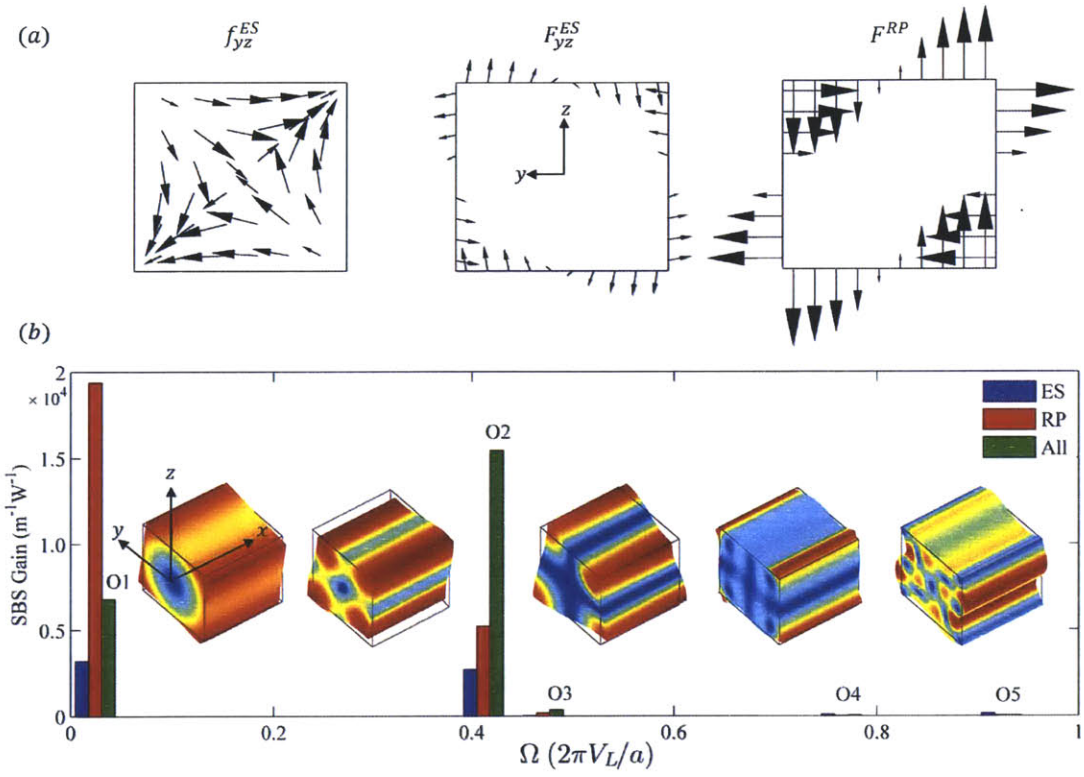

Figure 4-6: Detailed analysis of intermode coupling between E_{y11} (pump) and E_{z11} (Stokes). The operating point is $\omega = 0.203(2\pi c/a)$, $k_p = 0.750(\pi/a)$, $k_s = 0.665(\pi/a)$, and $q = 0.085(\pi/a)$ with $a = 315$nm. (a) The distribution of optical forces. The longitudinal forces (not shown here) are much smaller than the transverse forces. All optical forces are anti-symmetric about $y = 0$ and $z = 0$, exciting elastic modes with the same parities (O-modes). (b) Intermode SBS gains calculated from overlap integral using $Q = 1000$. The modal profiles of O1 through O5 at $q = 0.085(\pi/a)$ are inserted. The deformation is proportional to the displacement. The color represents the amplitude of total displacement with blue and red corresponding to zero and the maximal value.

4.4.4 Intermode coupling

In the discussion of FSBS and BSBS, pump and Stokes waves come from the same optical modes (intramode coupling). Now we apply our formalism to intermode coupling of the same silicon rectangular waveguide. For intramode coupling, the optical force is always symmetric about $y = 0$ and $z = 0$, exciting elastic modes with the same parities (E-modes). For intermode coupling, however, optical forces with all possible symmetries can be generated, and elastic modes with all possible symmetries can be excited. For instance, we consider the coupling between E_{y11} (pump) and E_{z11} (Stokes). The operating point is $\omega = 0.203(2\pi c/a)$, $k_p = 0.750(\pi/a)$, $k_s = 0.665(\pi/a)$, and $q = 0.085(\pi/a)$ with $a = 315$nm. Because E_{y11} and E_{z11} have the opposite symmetries about both $y = 0$ and $z = 0$, the induced optical force is anti-symmetric about both planes (Fig. 4-6(a)). Both electrostriction body force and radiation pressure try to pull the waveguide in one diagonal and push the waveguide in the other diagonal. Electrostriction pressure has the opposite effect, but is much weaker than the radiation pressure.

Under such optical force, elastic modes which are odd about both $y = 0$ and $z = 0$ (O-modes) can be excited. We calculated the SBS gains of O1 through O5 using a quality factor $Q = 1000$ for all the modes (Fig. 4-6(b)). O1 represents a rotation around x axis. So the overlap integral is proportional to the torque. The y component and z component of the optical forces generate torques with opposite signs, which significantly reduces the overlap integral. O1 still has a sizable SBS gain because of the small elastic frequency $\Omega = 0.024(2\pi V_L/a)$. O2 represents a breathing motion along the diagonal. Its modal profile coincides quite well with the optical force distribution, and the constructive combination between electrostriction force and radiation pressure results in total gain of $1.54 \times 10^4 \mathrm{m}^{-1}\mathrm{W}^{-1}$. O3 only have small SBS gains since it is largely longitudinal while the optical forces are largely transverse. The SBS gains of O4, O5 and higher order modes are close to zero because the complicated modal profiles cancel out the overlap integrals to a large extent.

4.4.5 Substrate effect

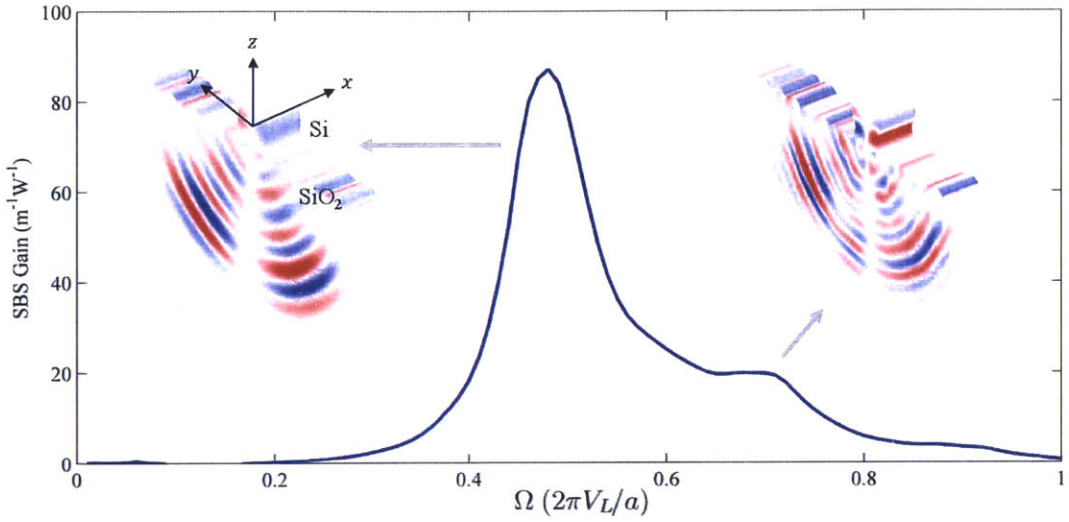

Figure 4-7: FSBS gains of a silicon waveguide on top of a silica substrate calculated from frequency response. For silica, we use refractive index $n = 1.45$, Young's modulus $E = 72.5 \times 10^9$ Pa, Poisson's ratio $\nu = 0.17$, and density $\rho = 2200\text{kg/m}^2$. The operating point is $\omega = 0.201(2\pi c/a)$, $k = 0.75(\pi/a)$, and $q = 0$ with $a = 311\text{nm}$. The inserts show the leaky elastic modes which give rise to the two resonant peaks. The deformation is proportional to the displacement. The color represents displacement component u_y.

In the discussion above, the silicon waveguide is suspended in air, which provides tight optical guidance and nearly perfect elastic guidance because of the huge elastic impedance mismatch between silicon and air. When the waveguide is put on top of a substrate with smaller refractive index, the optical guidance is still good, but the elastic guidance needs to be carefully examined. For BSBS, $q = 2k$ is not zero. If the phonon travels faster in the substrate than the waveguide, traveling elastic mode that is localized around the waveguide can be formed, enabling the on-chip realization of BSBS process [68]. For FSBS, q is close to zero, and phonon travels transversely. No matter whether phonon travels faster or slower in the substrate, the transverse vibration of the waveguide will always excite the radiative modes of the substrate. Therefore, elastic modes become leaky modes. The quality factor of such modes can be written as $Q_{tot}^{-1} = Q_{abs}^{-1} + Q_{rad}^{-1}$, where Q_{abs} corresponds to the dissipative losses,

and Q_{rad} corresponds to leakage into the substrate. Because of the large contact area and strong coupling between the waveguide and substrate, Q_{rad} can be quite small, putting a cap on Q_{tot} and reducing the FSBS gain of the whole structure.

To further illustrate the substrate effect, we put the silicon rectangular waveguide on a silica substrate and calculate the FSBS gains at operating point $\omega = 0.201(2\pi c/a)$ and $k = 0.75(\pi/a)$ with $a = 311$nm (Fig. 4-7). For leaky modes with strong coupling to external channels, the orthogonality condition (4.6) is not exact, and normalization factor $\langle \mathbf{u}, \rho\mathbf{u} \rangle$ can not be exactly determined. Therefore, we computed the FSBS gains using frequency response formula (4.3) rather than the eigen-mode formula (4.10). To model $Q_{abs} = 1000$, we used a bulk loss factor of 0.001 for the silicon waveguide. To model Q_{rad} into the substrate, we divide the substrate into two regions. The central region is lossless. The surrounding region has a bulk loss factor which increases quadratically from the inner radius to the outer radius. This region serves as a perfect matching layer (PML) which absorb outgoing elastic waves with minimal reflection [81]. The calculated FSBS gain spectrum has two peaks (Fig. 4-7). The leaky modes that give rise to these two peaks are similar to E2 and E5 of the suspended waveguide. However, these leaky modes have much smaller quality factor and much smaller peak FSBS gains. For instance, the leaky mode at $\Omega = 0.48(2\pi V_L/a)$ has $Q_{tot} = 5.6$ and a maximal FSBS gain of $87\text{m}^{-1}\text{W}^{-1}$, both of which are about 200 times smaller than the corresponding values of E2 under a hypothetical quality factor of 1000. The modal profiles of these leaky modes clearly demonstrate that the coupling between waveguide core and substrate is quite strong, and the radiative modes in the substrate are efficiently excited.

4.5 Translationally periodic waveguides

4.5.1 Silicon periodic waveguide

Based on the understanding of translationally invariant waveguides, we proceed to study the SBS process of a periodic waveguide. Throughout the study, we consider a suspended silicon waveguide with periodic cylindrical holes (Fig. 4-8(a) insert). The periodicity in x direction is a, the cross-section in yz plane is a by $0.4a$, and the radius of the cylindrical air hole is $0.25a$. The waveguide has three geometric symmetry planes $x = 0$, $y = 0$, and $z = 0$. We assume that the crystal structure of the material is also symmetric about these three planes so that the anisotropy in optical, elastic, and photo-elastic constants doesn't break these mirror symmetries. This condition is clearly satisfied for silicon in the current orientation.

First, we analyze the optical modes of the waveguide. The optical modes are categorized into yeven/yodd (zeven/zodd) according to the parity about $y = 0$ ($z = 0$). The fundamental mode is yodd and zeven with E_y as the dominant component of electric field. As k increases from $0.5(\pi/a)$ to π/a, the frequency of the fundamental mode increases from $0.228(2\pi c/a)$ to $0.280(2\pi c/a)$ (Fig. 4-8(a)). We fix the pump wavelength at 1.55μm. So the corresponding a varies from 354nm to 434nm. The optical mode $\mathbf{E}$ doesn't have fixed parity about $x = 0$ since k breaks this mirror symmetry. Actually, the reflection of $\mathbf{E}$ about $x = 0$ corresponds the the eigen-mode at $-k$, which is also the complex conjugate of $\mathbf{E}$. Under a properly chosen phase, the reflection of $\mathbf{E}$ is exactly $\mathbf{E}^*$. Therefore,

$$E_i(-x, y, z) = E_i^*(x, y, z)s_i \tag{4.32}$$

where $s_x = -1$, and $s_{y,z} = 1$. The subscript in s does not induce summation when encountered with repeated indices.

Next, we analyze the elastic modes of the waveguide. Again, the elastic modes are categorized into yeven/yodd (zeven/zodd) according to the parity about $y = 0$ ($z = 0$). Since optical modes are either even or odd about these two planes, and

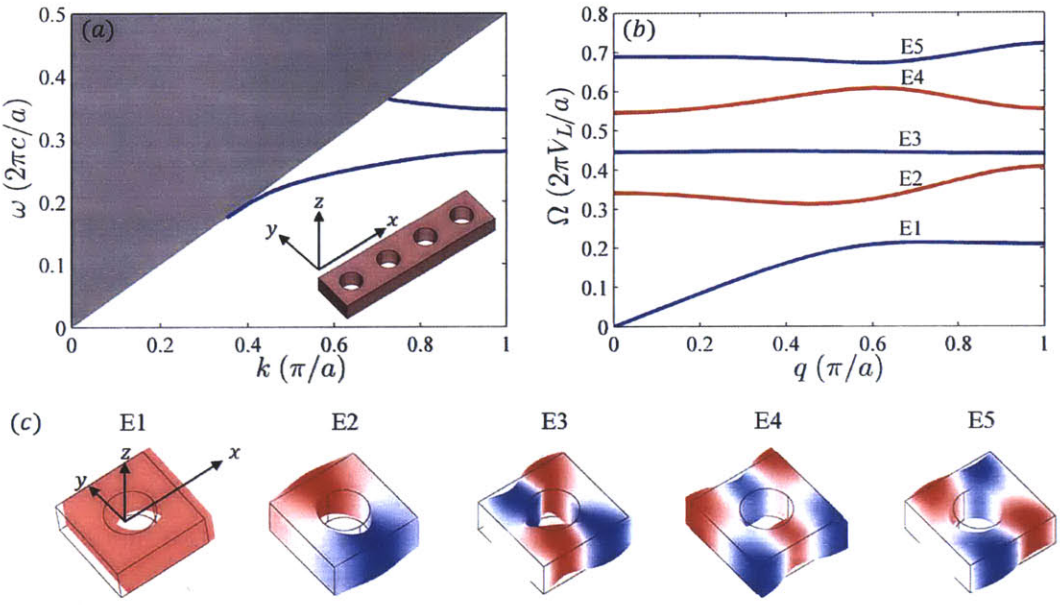

Figure 4-8: The optical and elastic modes of a periodic silicon waveguide. (a) The dispersion diagram of the fundamental optical mode which is yodd and zeven. The area shaded in gray represents light cone of air. (b) The dispersion diagram of elastic modes which are yeven and zeven. Xeven and xodd modes at $q = 0$ are colored in red and blue respectively. (c) Elastic modal profiles at $q = 0$. The deformation is proportional to the displacement $\mathbf{u}$. The colored surface represents displacement component u_y. Red, white and blue correspond to positive, zero, and negative values respectively. Mode E1 is a parallel shift along x direction.

optical forces is quadratic in electric field, optical force is always symmetric these two planes. So we only consider elastic modes that are both yeven and zeven (Fig. 4-8(b)). At $q = 0$, the symmetry about $x = 0$ is recovered. The eigen-mode $\mathbf{u}$ can be taken to be real field, and be categorized into xeven and xodd (Fig. 4-8(c)). At nonzero q, the eigen-mode $\mathbf{u}$ is a complex field without fixed parity about $x = 0$. However, similar to the optical modes, we can choose a proper phase of $\mathbf{u}$ so that:

$$u_i(-x, y, z) = u_i^*(x, y, z)s_i \tag{4.33}$$

4.5.2 Forward SBS

In FSBS, pump and Stokes waves have approximately the same wavevector k and excite standing elastic modes at $q = 0$. To study the distributions of different optical forces, we select an operating point at $k = 0.75(\pi/a)$, $\omega = 0.265(2\pi c/a)$ and $q = 0$ with $a = 420$nm. The amplitude of optical forces in FSBS is real (Fig. 4-9(a)). The dominant component of electrostriction body force is f_y^{ES}, which comes from the fact that the dominant component of electric field is E_y and the fact that p_{11} is about five times larger than p_{12}. In addition, electrostriction pressure points inwards and radiation pressure point outwards. Radiation pressure is about five times larger than electrostriction pressure.

One important feature about the optical force distribution is that all optical forces are symmetric about $x = 0$ although the electric field doesn't have this symmetry. This can be formerly proven by examining the symmetry of electrostriction tensor and MST. The electrostriction tensor in FSBS is given by:

$$\sigma_{ij} = -\frac{1}{2}\epsilon_0 n^4 p_{ijkl}\Re(E_k E_l^*) \tag{4.34}$$

Because the crystal structure of the waveguide material is symmetric about $x = 0$, the photoelastic tensor is zero when there is odd number of x in the subscript: $p_{ijkl} =$

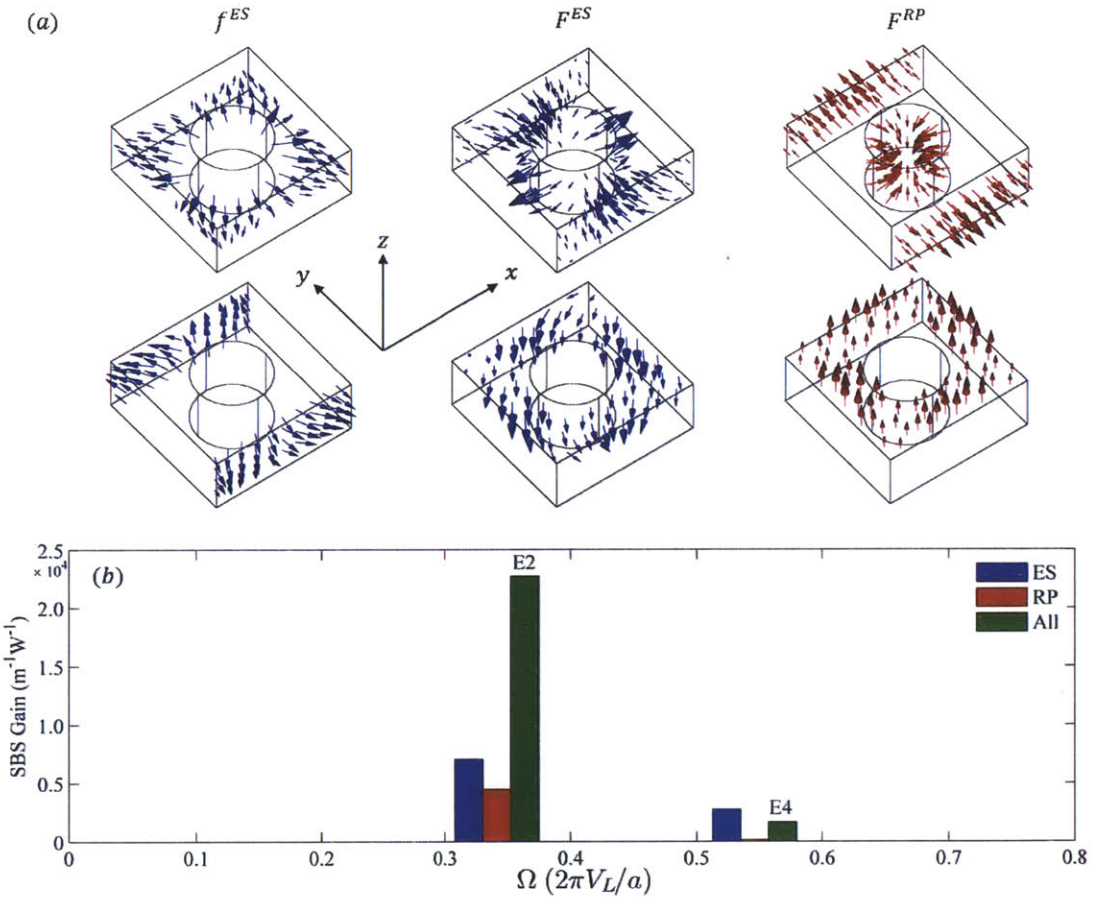

Figure 4-9: Detailed analysis of FSBS at $\omega = 0.265(2\pi c/a)$, $k = 0.75(\pi/a)$, and $q = 0$ with $a = 420$nm. (a) Distributions of optical forces. For electrostriction body force, the two subplots show the body force on cross-sections $z = 0$ and $y = \pm 0.4a$. For electrostriction pressure and radiation pressure, the two subplots show the pressure on the lateral surfaces and the top surface. Electrostriction pressure is multiplied by 5 so that it can be plotted on the same scale as radiation pressure. All the optical forces are symmetric about to $x = 0$. (b) The FSBS gains of individual elastic modes using $Q = 1000$. Blue, red, and green bars represent the FSBS gains from electrostriction force, radiation pressure, and both effects respectively.

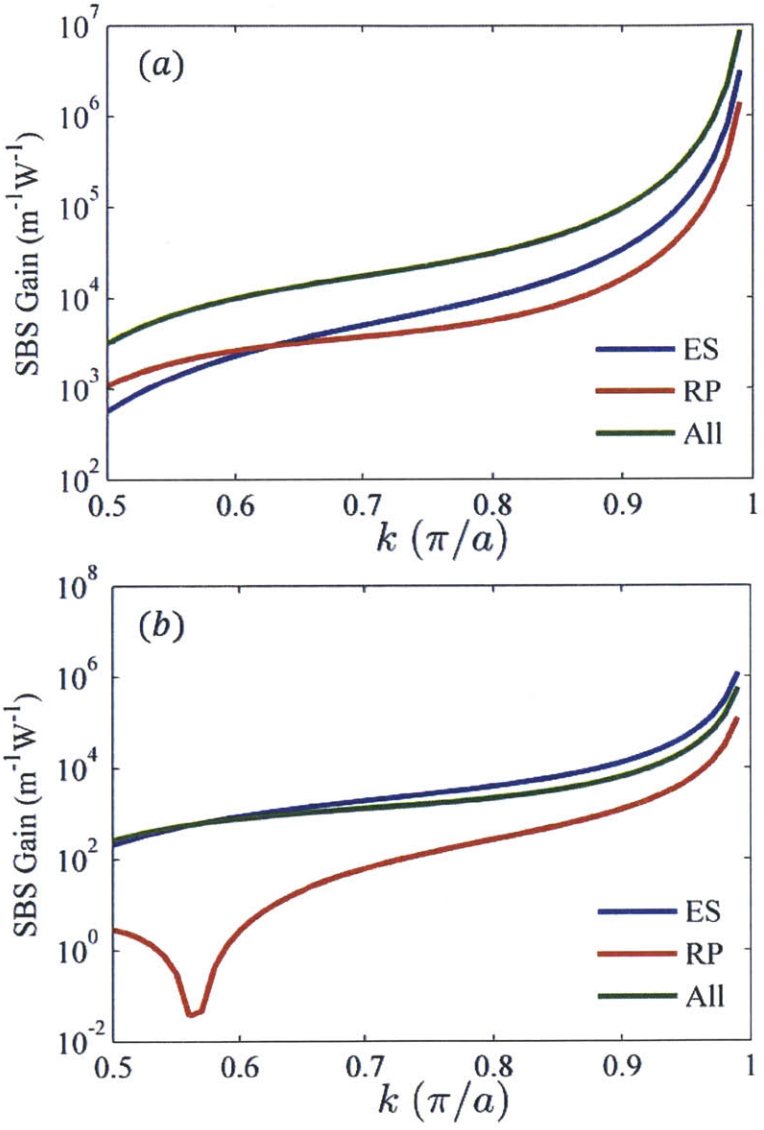

Figure 4-10: Calculated FSBS gains for (a) E2 and (b) E4 as k varies from $0.5(\pi/a)$ to π/a, and a varies from 354nm to 434nm. For both E2 and E4, the FSBS gain approaches to infinity as $1/\Delta k^2$ at the Brillouin zone boundary.

$p_{ijkl}s_is_js_ks_l$. Combining this property with (4.32) and $s_i^2 = 1$, we have

$$\begin{aligned}\sigma_{ij}(-x,y,z) &= -\frac{1}{2}\epsilon_0 n^4 p_{ijkl}\Re(E_k(-x,y,z)E_l^*(-x,y,z)) \\ &= -\frac{1}{2}\epsilon_0 n^4 p_{ijkl}\Re(E_k^*(x,y,z)E_l(x,y,z))s_is_js_ks_ls_ks_l \\ &= \sigma_{ij}(x,y,z)s_is_j \end{aligned} \tag{4.35}$$

The MST in FSBS is given by:

$$T_{ij} = \frac{1}{2}\epsilon_0\epsilon(E_iE_j^* + E_i^*E_j - \delta_{ij}\mathbf{E}\cdot\mathbf{E}^*) \tag{4.36}$$

Using (4.32) and $\delta_{ij} = \delta_{ij}s_is_j$, we have

$$\begin{aligned}T_{ij}(-x,y,z) &= \frac{1}{2}\epsilon_0\epsilon(2\Re(E_i(-x,y,z)E_j^*(-x,y,z)) - \delta_{ij}|\mathbf{E}(-x,y,z)|^2) \\ &= \frac{1}{2}\epsilon_0\epsilon(2\Re(E_i(x,y,z)E_j^*(x,y,z)) - \delta_{ij}|\mathbf{E}(x,y,z)|^2)s_is_j \\ &= T_{ij}(x,y,z)s_is_j \end{aligned} \tag{4.37}$$

Combining (4.35) and (4.37) with the fact that optical force is given by the divergence of the corresponding tensor, we conclude that both the electrostriction force and radiation pressure are symmetric about $x = 0$ in FSBS.

The symmetry of optical forces combined with the fact that elastic modes have fixed parity about $x = 0$ at $q = 0$ indicates that only xeven modes have nonzero FSBS gains. We calculate the FSBS gain using a quality factor $Q = 1000$ for all the elastic modes (Fig. 4-9(b)). Only xeven modes E2 and E4 have nonzero FSBS gains, which confirms the symmetry analysis. Mode E2 is essentially a transverse mode with large displacement in y direction and small displacement in z direction. This modal profile agrees well with electrostriction body force f_y^{ES} and the radiation pressure on the outer lateral surfaces, generating large FSBS gains from electrostriction ($0.71 \times 10^4 \mathrm{m^{-1}W^{-1}}$) and radiation pressure ($0.44 \times 10^4 \mathrm{m^{-1}W^{-1}}$). Furthermore, these two effect add up constructively, resulting a total FSBS gain as large as $2.27 \times 10^4 \mathrm{m^{-1}W^{-1}}$. Model E4 has a small FSBS gain of $0.17 \times 10^4 \mathrm{m^{-1}W^{-1}}$ because (1) the nodal planes of u_y

reduce the overlap integral of electrostriction body force and (2) radiation pressures on the outer and inner lateral surfaces have opposite effects which result in a very small FSBS gain from radiation pressure.

Next, we study how the FSBS gain varies as the operating point moves from Brillouin zone interior to boundary (Fig. 4-10). For Mode E2, electrostriction force and radiation pressure always add up constructively, creating a large FSBS gain. For Mode E4, the SBS gain from radiation pressure vanishes around $k = 0.57(\pi/a)$ because of the cancellation of radiation pressures on different surfaces. For both E2 and E4, when the operating point approaches Brillouin zone boundary, the overlap integrals approaches to a constant while the optical group velocity approaches to zero as Δk ($\Delta k = |k - \pi/a|$). As a result, the SBS gains approach to infinity as $1/\Delta k^2$. For instance, the total SBS gain for E2 is $9.7 \times 10^4 \mathrm{m}^{-1}\mathrm{W}^{-1}$ at $k = 0.90(\pi/a)$ and $8.7 \times 10^6 \mathrm{m}^{-1}\mathrm{W}^{-1}$ at $k = 0.99(\pi/a)$. Therefore, SBS nonlinearity can be significantly enhanced in the slow light regime.

4.5.3 Backward SBS

In BSBS, pump and Stokes waves travel in the opposite directions, exciting elastic modes at $q = 2k$. To study the distribution of optical forces, we select an operating point at $k = 0.75(\pi/a)$, $\omega = 0.265(2\pi c/a)$ and $q = 1.5(\pi/a)$ with $a = 420\mathrm{nm}$. The amplitude of optical forces in BSBS is complex and dependent on the phase of the electric field. Under condition (4.32), the real part of optical forces is symmetric about $x = 0$ while the imaginary part is anti-symmetric about $x = 0$ (Fig. 4-11(a)). This can be formerly proven by examining the electrostriction tensor and MST in BSBS. The electrostriction tensor in BSBS is:

$$\sigma_{ij} = -\frac{1}{2}\epsilon_0 n^4 p_{ijkl} E_k E_l \tag{4.38}$$

MST in BSBS is:

$$T_{ij} = \frac{1}{2}\epsilon_0 \epsilon (2E_i E_j - \delta_{ij}\mathbf{E}\cdot\mathbf{E}) \tag{4.39}$$

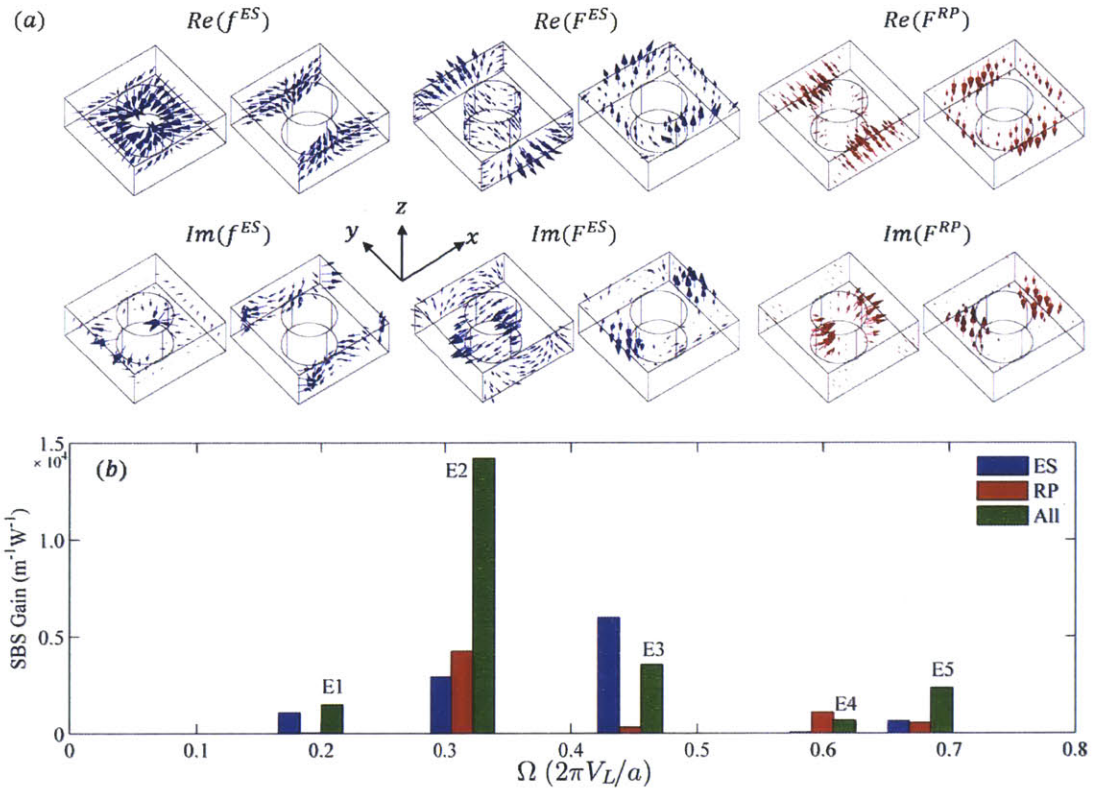

Figure 4-11: Detailed analysis of BSBS at $k = 0.75(\pi/a)$, $\omega = 0.265(2\pi c/a)$ and $q = 1.5(\pi/a)$ with $a = 420$nm. (a) Distributions of the real and imaginary parts of optical forces. For electrostriction body force, the two subplots show the body force on cross-sections $z = 0$ and $y = \pm 0.4a$. For electrostriction pressure and radiation pressure, the two subplots show the pressure on the lateral surfaces and the top surface. Electrostriction pressure is multiplied by 5 so that it can be plotted in the same scale as radiation pressure. The real part of all the optical forces is symmetric about $x = 0$, while the imaginary part of all the optical forces is anti-symmetric about $x = 0$. (b) The BSBS gains of individual elastic modes calculated from overlap integrals. Blue, red, and green bars represent the BSBS gains from electrostriction force, radiation pressure, and both effects respectively.

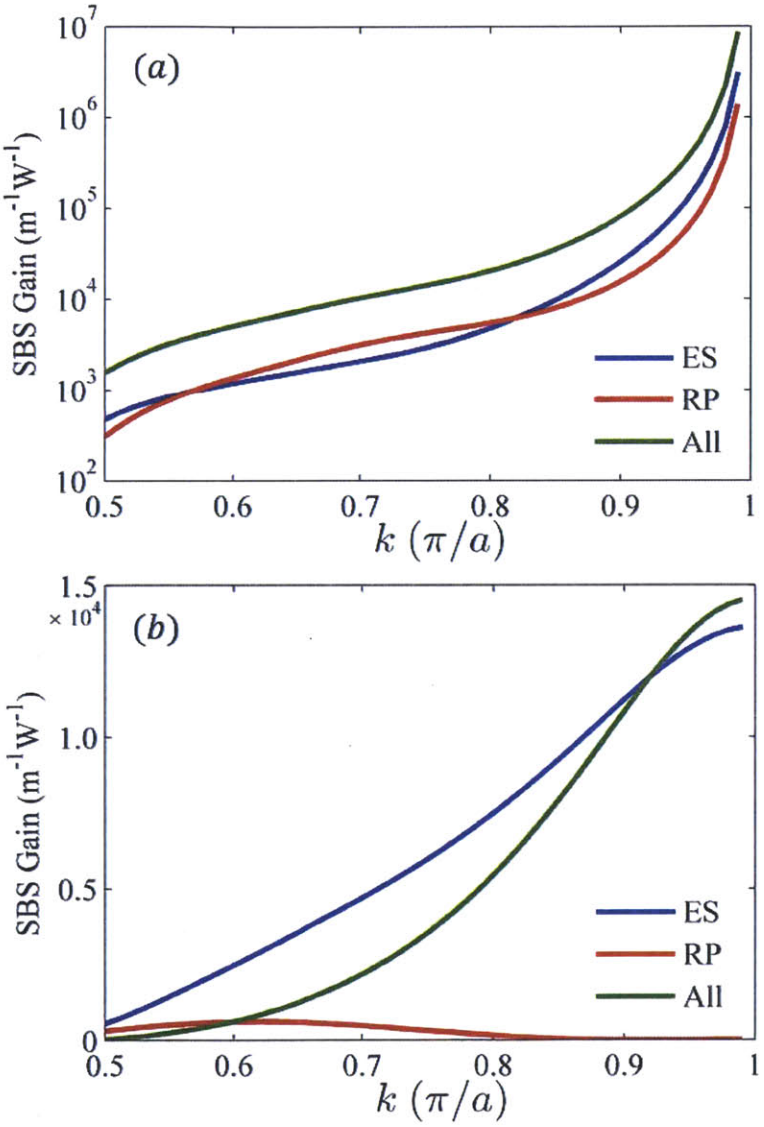

Figure 4-12: Calculated BSBS gains for (a) E2 and (b) E3 as k varies from $0.5(\pi/a)$ to π/a and a varies from 354nm to 434nm. For E2, the BSBS gain approaches to infinity as $1/\Delta k^2$. For E3, the BSBS gain approaches to a constant at the Brillouin zone boundary.

Following similar derivations as FSBS, we can show that both tensors have the following properties:

$$\sigma_{ij}(-x,y,z) = \sigma_{ij}^{*}(x,y,z)s_i s_j \tag{4.40}$$

$$T_{ij}(-x,y,z) = T_{ij}^{*}(x,y,z)s_i s_j \tag{4.41}$$

Taking the real and imaginary parts of the expressions above, we can see that the real part of optical forces is symmetric about $x = 0$ and the imaginary part is anti-symmetric about $x = 0$. On the other hand, (4.33) shows that the real part of elastic displacement is even about $x = 0$, and the imaginary part is odd about $x = 0$. Therefore, the overlap integrals between optical forces and elastic displacements are real, which indicates that the contributions from different optical forces add up either constructively or destructively:

$$G_{all} = (\sqrt{G_{ES}} \pm \sqrt{G_{RP}})^2 \tag{4.42}$$

We calculate the BSBS gain using the a quality factor $Q = 1000$ for all the elastic modes (Fig. 4-11(b)). Mode E2 has the largest BSBS gain ($1.42 \times 10^4 \mathrm{m^{-1}W^{-1}}$), which comes from a constructive combination of electrostriction force ($0.29 \times 10^4 \mathrm{m^{-1}W^{-1}}$) and radiation pressure ($0.42 \times 10^4 \mathrm{m^{-1}W^{-1}}$). Mode E3 have the second largest BSBS gain ($0.35 \times 10^4 \mathrm{m^{-1}W^{-1}}$), which mainly comes from electrostriction body force.

Next, we scan the operating point from $k = 0.5(\pi/a)$ to $k = \pi/a$ and calculate the corresponding BSBS for Mode E2 and E3 (Fig. 4-12). For Mode E2, electrostriction force and radiation pressure always add up constructively although their relative strength varies for different k. In the slow light regime, the BSBS gain approaches to infinity as $1/\Delta k^2$ as the optical group velocity vanishes as Δk. On contrast, the BSBS gain of Mode E3 approaches to a constant at the Brillouin zone boundary. This comes from two properties associated with $k = \pi/a$. At $k = \pi/a$, BSBS is equivalent to FSBS, and optical forces are symmetric about $x = 0$. When k is slightly way from this point, the BSBS optical force can still be decomposed into symmetric and

anti-symmetric components with the anti-symmetric component in the order of Δk. In addition, at $k = \pi/a$, $q = 2k = 2\pi/a$, which is equivalent to $q = 0$. So the phase-matching elastic modes recover their parities about $x = 0$, and Mode E3 is odd about $x = 0$. When k is slightly away from this point, Mode E3 can be decomposed into odd and even components with the even component in the order of Δk. Therefore, the overlap integral between backward optical forces and the modal profile of Mode E3 vanishes as Δk. Because both the overlap integral and optical group velocity vanishes as Δk, the SBS gain approaches to a constant in the slow light region.

4.6 Concluding remarks

In this chapter, we propose a general framework of calculating the SBS gain via the overlap integral between optical forces and elastic eigen-modes. Our method is based on the frequency response representation of SBS gains [76]. By decomposing the frequency response into elastic eigen-modes, we show that the SBS gain is the sum of many Lorentian components which center at elastic eigen-frequencies. The SBS gain spectrum is completely determined by the quality factor and maximal gain of individual elastic modes. Therefore, our method is conceptually clearer and computationally more efficient than the frequency response method.

Through the study of a silicon waveguide, we demonstrate that our method can be applied to both FSBS and BSBS, both intramode and intermode coupling, both nanoscale and microscale waveguides. Both analytial expressions and numerical examples show that SBS nonlinearity is tightly connected to the symmetry, polarization, and spatial distributions of optical and elastic modes.

In addition, we analyze the SBS process of a suspended periodic waveguide. The suspended geometry provides nearly perfect lateral confinement for elastic modes [76]. The periodic structure slows down the group velocity of optical modes. The combination of these two effects creates a giant enhancement of SBS nonlinearity over conventional nonlinear fibers [91]. We also show the importance of mode symmetry in both FSBS and BSBS processes. Our analysis doesn't rely on the specific

waveguide geometry or the crystal structure of silicon. The conclusion about the relation between mode symmetry and SBS gain is valid as long as the waveguide has a symmetry plane perpendicular to the propagation axis and the crystal structure of the underlying material doesn't break this symmetry. Our results can be readily applied to simpler structures such as translationally invariant waveguides and more complicated structures such as photonic/phononic dual crystal waveguides.

Because electrostriction force and radiation pressure have distinct distributions and material dependence, SBS nonlinearity can be further tailored and optimized through material selection and structural design. For example, the direction of electrostriction force depends on the sign of photoelastic tensors. For silicon, $p_{11} < 0$ and $p_{12} > 0$. When the electric field has a large y component, the FSBS electrostriction force points outward in y direction and inward in z direction. Under such force distribution, the "breathing" mode E2 has the largest FSBS gain in most circumstances. For GaAs and germanium, $p_{11} < 0$ and $p_{12} < 0$. The FSBS electrostriction force points outwards in both y and z direction. Such electrostriction force add constructively with radiation pressure, generating large FSBS gain for the "expanding" mode E5. For another example, the SBS gain of a periodic waveguide discussed above can be further tailored by varying the size of the air rod and the height of the slab. In short, the overlap integral representation of SBS gains developed in this chapter provides the guidelines of tailoring and optimizing SBS nonlinearity.

Chapter 5

A Novel Class of Hybrid Photon-Phonon Waveguides

5.1 Introduction

In the previos chapter, we developed a general framework of calculating SBS gains. Through the studies of various SBS processes, we can see that SBS can create highly efficient photon-phonon coupling over a wide frequency range, which can be applied to a variety of hybrid signal processing schemes. For instances, SBS processes have yielded wide bandwidth pulse compression [99], pulse and waveform synthesis [100], coherent frequency comb generation [101], variable bandwidth optical amplifiers [102], reconfigurable filters [103], and coherent beam combining schemes [104].

The simple waveguide structures studied in the previous chapter, while clearly demonstrate the essential features of SBS processes, entangle the design of optical and elastic modes. In this chapter, we collaborated with researchers in Sandia to propose a novel class of hybrid photon-phonon waveguides which allow for the independent control of optical and elastic modes. By applying the framework developed in the previous chapter, we theoretically characterize various features of the hybrid waveguide, including optical force distributions, elastic modal profiles, and FSBS gains. In addition, we develop a set of coupled amplitude equations which can be used to extract resonant frequency, quality factor, and FSBS gains from nonlinear

response of the real structures fabricated by our collaborators in Sandia. Both the theoretical analysis and experimental results demonstrate that the hybrid waveguide can create highly efficient and tunable photon-phonon coupling over a very wide frequency range.

5.2 Hybrid photon-phonon waveguides

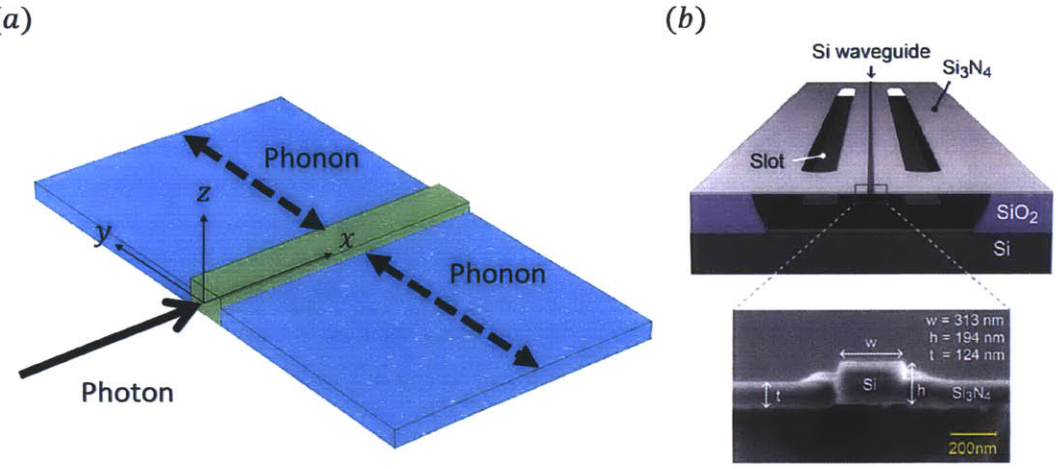

Figure 5-1: Structure of the hybrid photon-phonon waveguide. (a) Schematics of the waveguide. A silicon waveguide is embedded in a suspended silicon nitride membrane. In FSBS, photon travels in the longitudinal direction, generating transverse optical forces, and exciting transverse phonons. (b) Structure of the fabricated waveguide. There are two air slots in the silicon nitride membrane. The segment between two slots forms the target structure in (a). The lower figure shows the SEM cross-section of the silicon waveguide core within the silicon nitride membrane.

For the waveguides studied in the previous chapter, both the optical and elastic modes are determined by the waveguide geometry. A change in the waveguide cross-section or unit cell structures will impact optical and elastic modes simultaneously. To separate the control over optical and elastic modes, we collaborated with researchers in Sandia to propose a membrane-waveguide structure as shown in Fig. 5-1(a). In this structure, a silicon waveguide is embedded in a suspended silicon nitride membrane. In forward SBS, photon travels longitudinally within the core due to the total internal

reflection between silicon and silicon nitride boundaries. Phonon travels transversely along the membrane due to the phase matching condition in forward process. The lateral boundaries of the membrane provides nearly perfect reflections to transverse phonons, forming a Fabry-Perot resonator, and generating a series of discrete elastic modes. The spacing between neighboring elastic modes is inversely proportional to the membrane width.

Compared to the waveguide structure in the previous chapter, the current structure has two advantages. First, in the current structure, the optical mode is largely determined by the core, while the elastic mode is largely determined by the membrane. This separation significantly increases the tunability of the whole structure. Second, elastic modes are extended over the entire membrane, making it possible to integrate other photonic/phononic components into the membrane. In this hybrid photon-phonon systems, phonons are no longer the by-product of stimulated brillouin scattering. Instead, phonons traveling in the membrane become the carrier of information, creating new forms of coherent signal processing schemes.

Figure 5-1(b) shows the experimental structure fabricated by our collaborators in Sandia. The structure includes an embedded silicon waveguide and a silicon nitride membrane sitting on top of silica substrate. There are two air slots in the silicon nitride membrane, the segment between which forms the suspended structure. By varying the edge to edge distance d between two air slots, we can change the width of the suspended membrane conveniently. As shown in the SEM image, the waveguide core is 313nm by 194nm. The thickness of the membrane is 124nm. Four different waveguides with $d = [0.8,\ 1.8,\ 2.8,\ 3.8]\mu m$ were fabricated. We will use these values in the following analysis.

5.3 Theoretical analysis

In this section, we use the framework developed in the previous chapter to analyze the forward SBS process of $d = 3.8\mu m$ waveguide.

The optical modes are tightly confined in the silicon core due to the large index

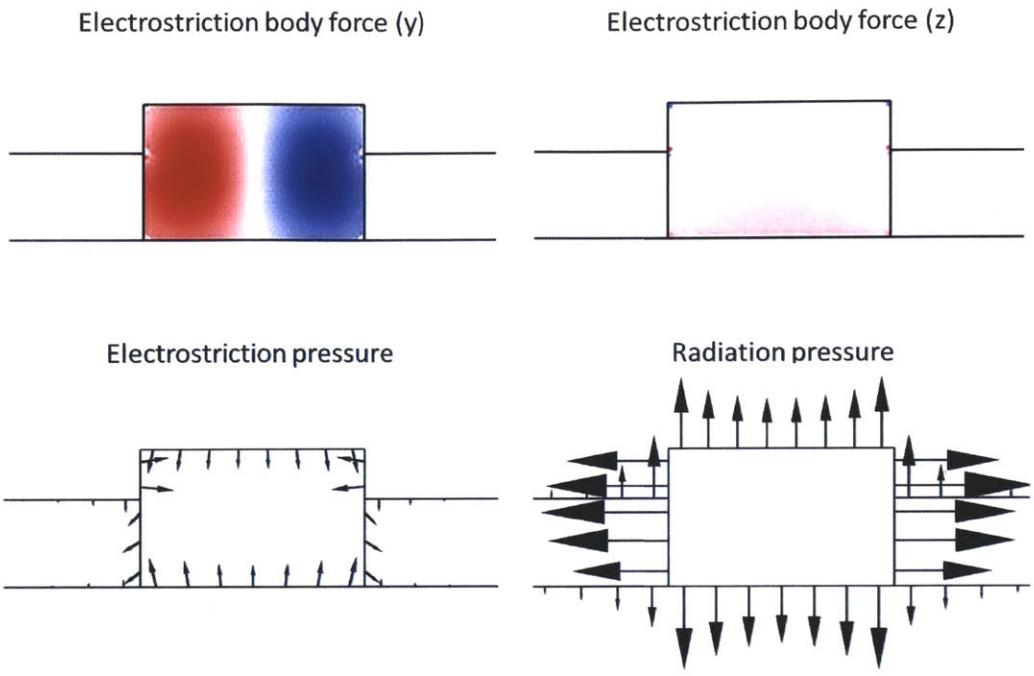

Figure 5-2: Optical force distributions of $d = 3.8\mu m$ waveguide.

contrast between silicon ($n = 3.5$) and silicon nitride ($n = 2.0$). The fundamental optical mode is E_{y11} with a dominant E_y component. Assuming the incident wavelength is $1.55\mu m$, the optical mode has a phase index $n_p = 1.78$ and a group index $n_g = 4.30$. We calculate the optical force distribution in FSBS (Fig. 5-2). As demonstrated in the previous chapter, all optical forces in FSBS are transverse. Electrostriction body force is mainly in y direction. Radiation pressure is much larger than electrostriction pressure. There are large radiation pressures on the internal boundary due to the jump of refractive index.

The elastic modes extend over the entire membrane. In FSBS, $q = 0$. Elastic modes are either pure longitudinal with displacement in x direciton, or pure transverse with displacement in yz plane. Since optical forces are transverse. only the transverse elastic modes can be excited. For an infinite membrane, transverse elastic modes are called Lamb waves [93]. The fundamental Lamb wave has zero cut-off and an approximately linear dispersion relation $\Omega \approx Vk_y$. For a membrane with finite

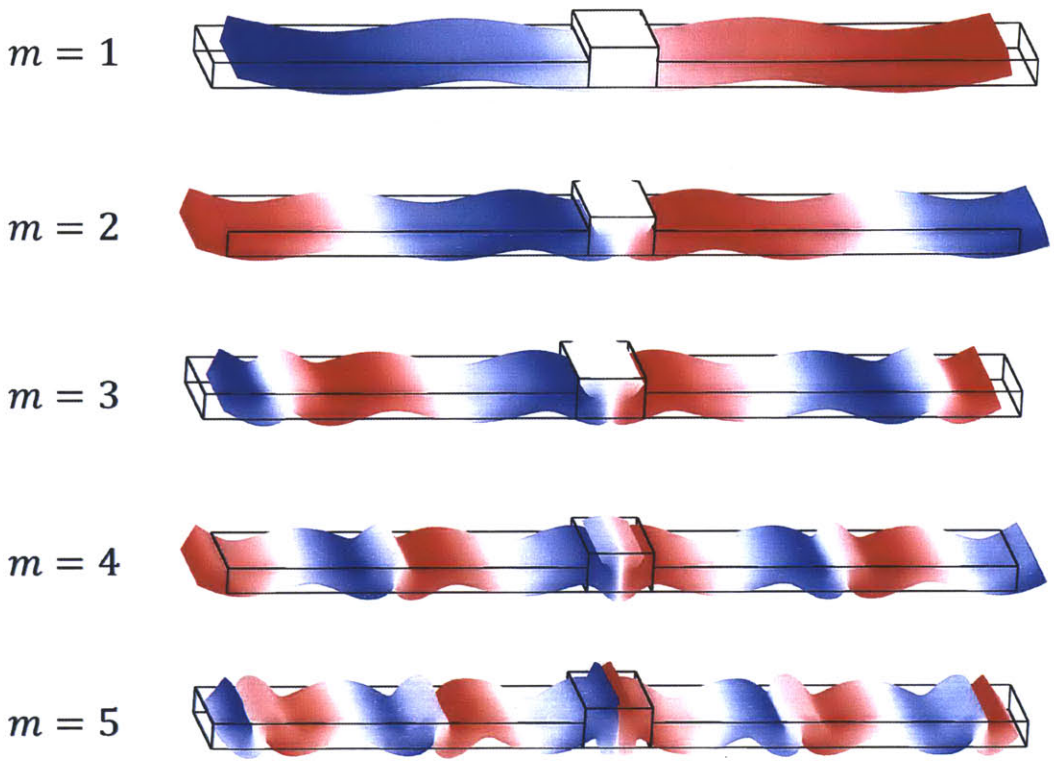

Figure 5-3: Elastic modal profiles of $d = 3.8\mu m$ waveguide. The color represents displacement in y direction with blue, white and red corresponding to negative, zero, and positive values. The deformation is proportional to displacement.

width d, Lamb waves are reflected at the lateral boundaries, creating discrete elastic resonances. The resonant condition is:

$$k_y \approx (2m-1)\frac{\pi}{d} \tag{5.1}$$

The $2m-1$ term comes from the fact that the optical force is symmetric about $y = 0$. Applying the approximately linear dispersion relation, we can see that resonant frequencies are approximately equally spaced.

$$\Omega_m \approx (2m-1)\frac{\pi V}{d} \tag{5.2}$$

Figure 5-3 plots the profiles of the first five elastic modes. Mode 1 has large u_y and small u_z. As m increases, the relative size of u_z increases.

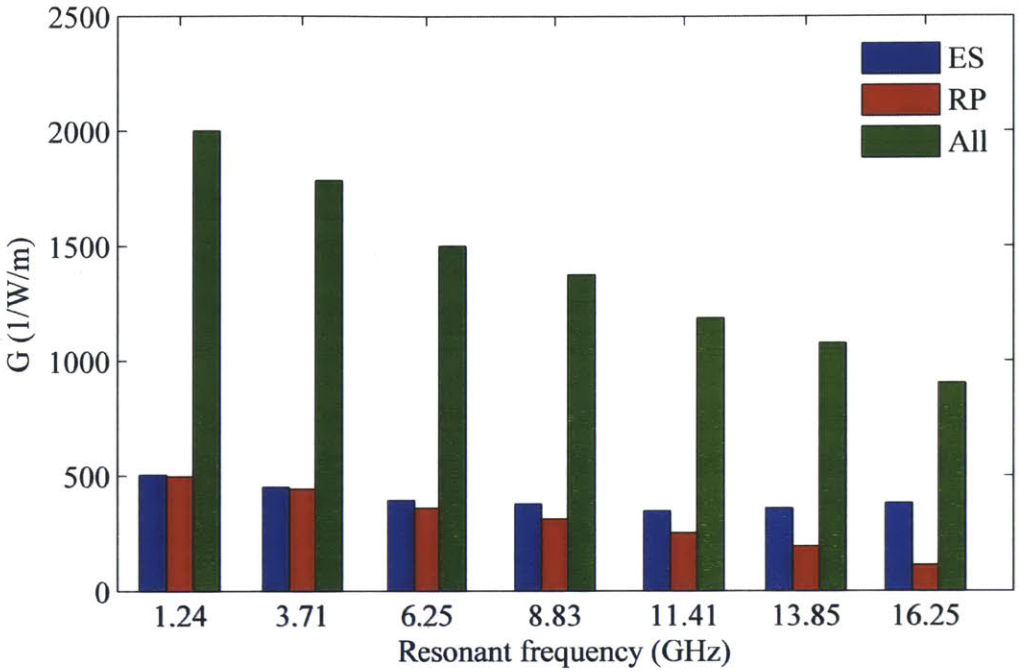

Figure 5-4: Calculated FSBS gains of $d = 3.8\mu m$ waveguide using a hypothetical quality factor $Q = 1000$. The blue, red, and green bars correspond to FSBS gains from electrostriction, radiation pressure, and both.

Combining optical force distribution and elastic modal profiles, we proceed to calculate the FSBS gains using a hypothetical quality factor $Q = 1000$ (Fig. 5-4). For all elastic modes, electrostriction force and radiation pressure add up constructively. The FSBS gain from radiation diminishes faster than that from electrostriction for two reasons. First, electrostriction force is distributed over the waveguide cross-section, while radiation pressure focuses on the waveguide boundary. Therefore, radiation pressure has lower spatial frequency and diminishes faster as m increases. Second, radiation pressure on the top and bottom (F_z^{RP}) is destructive to radiation pressure on the internal boundaries (F_y^{RP}). As m increases, the displacement in z direction becomes more significant, amplifying the cancellation between F_z^{RP} and F_y^{RP}. The total FSBS gains decreases slowly as m increases, producing efficient photon-phonon

coupling over a wide frequency range.

5.4 Data analysis

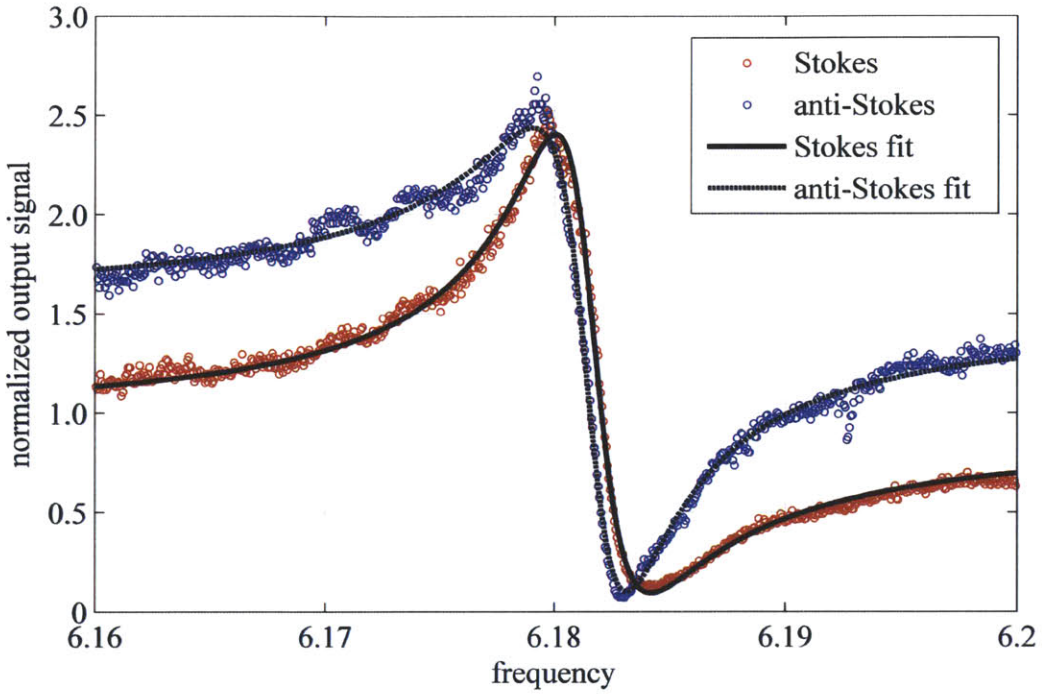

Figure 5-5: Output signals for the $m = 3$ resonance of $d = 3.8\mu m$ waveguide. Dots and lines correspond to measurement and least square fit to (5.6) respectively.

Experimental studies of SBS nonlinearity were performed by our collaborators in Sandia, yielding direct measurement of FSBS gains of the device. Through four-wave-mixing (FWM) experiments, modulated pump (1556 nm) and continuous-wave probe (1536 nm) signals are injected into the device. The modulated pump drives the excitation of Brillouin-active phonons over a wide range of frequencies as the pump modulation frequency is swept. The powers of stokes and Anti-stokes sidebands of the probe beam are measured to determine the nonlinear response of the system.

The output signal as a function of modulation frequency has a Fano-like lineshape (Fig. 5-5). This comes from the coherent combination of SBS and background non-linearity. We develop a set of spatial coupled amplitude equations to understand this

process quantitatively. Let A_1 and A_2 be the amplitude of double pumps, A_4 be the amplitude of the probe, A_3 and A_5 be the amplitudes of Stokes and anti-Stokes sidebands. The coupled amplitude equation with both SBS and background third order susceptbility is:

$$\begin{aligned}
\frac{dA_1}{dx} &= i\gamma_B^*|A_2|^2A_1 + i\gamma_{K1}(|A_1|^2 + 2|A_2|^2 + 2|A_4|^2)A_1 \\
\frac{dA_2}{dx} &= i\gamma_B|A_1|^2A_2 + i\gamma_{K1}(|A_2|^2 + 2|A_1|^2 + 2|A_4|^2)A_1 \\
\frac{dA_4}{dx} &= i\gamma_{K1}(|A_4|^2 + 2|A_1|^2 + 2|A_2|^2)A_4 \\
\frac{dA_3}{dx} &= i(\gamma_B^* + 2\gamma_{K2}^*)A_1A_2^*A_4 \\
\frac{dA_5}{dx} &= i(\gamma_B + 2\gamma_{K2})A_1^*A_2A_4
\end{aligned} \tag{5.3}$$

In the equation above, γ_B is SBS susceptbility. By applying power conservation and KK relation, we can show that γ_B is connected to SBS gain through the following relation [91]:

$$\gamma_B(\Omega) = \frac{G}{2}\frac{\Gamma/2}{\Omega_0 - \Omega - i\Gamma/2} \tag{5.4}$$

γ_{K1} represents the background third order susceptbility involving two optical frequencies. The real part of γ_{K1} represents Kerr effect, while the imaginary part of γ_{K1} represents two photon absorption (TPA). γ_{K2} represents the background third order susceptbility in four wave mixing (FWM). Thre real part of γ_{K2} represents Kerr effect, while the imaginary part of γ_{K2} represents any loss or gain processes in FWM. Within the narrow frequency window around each resonance, background susceptilities are essentially frequency independent. Assuming powers of the pump and probe beams don't decrease much along the propagation, we have:

$$P_3(\Omega) = P_5(\Omega) = |\gamma_B(\Omega) + 2\gamma_{K2}|^2P_1P_2P_4L^2 \tag{5.5}$$

(5.5) shows that the output signal is the coherent combination of SBS and background nonlinearities. (5.5) also indicates that the background susceptiblity should be symmetric for Stokes and anti-Stokes sidebands. The experimental data shows that the

background susceptiblities of Stokes and anti-Stokes lines are slightly different. To capture this asymmetry, (5.5) is modified to:

$$\begin{cases} P_3(\Omega) = |\gamma_B(\Omega) + 2\gamma_{K2,S}|^2 P_1 P_2 P_4 L^2 \\ P_5(\Omega) = |\gamma_B(\Omega) + 2\gamma_{K2,A}|^2 P_1 P_2 P_4 L^2 \end{cases} \tag{5.6}$$

By fitting Stokes and anti-Stokes responses jointly to (5.6), we can extract the resonant frequency, the quality factor, and the relative FSBS gain of each resonance. In addition, we find that the fitted $\gamma_{K2,S}$ and $\gamma_{K2,A}$ converge to the same value γ_{K2} as m increases. We assume that this γ_{K2} corresponds to the Kerr effect of silicon. Employing the full vectorial method for computing Kerr susceptibility [105], γ_{K2} was computed to be 188 $m^{-1}W^{-1}$. We can use this value to calibrate the response curve and determine the absolute value of FSBS gains.

5.5 Measurement vs calculation

In this section, we compare the measured nonlinearity of the hybrid waveguide with finite element calculations.

The first feature to compare is the resonant frequency (Fig. 5-6). Waveguides with four different d were fabricated. The resonant signatures in the nonlinear response agree well with the calculated elastic eigen-frequencies. Fig. 5-6 shows that the resonant frequencies of the hybrid waveguide can be easily tuned over 1-18GHz by varying the distance between two slots.

The second feature to compare is the resonant strength (Fig. 5-7). Using the fitting method described in the previous section, we extract the quality factor and FSBS gains of the $d = 3.8\mu m$ waveguide. The measured quality factors are in the range of 1000 to 2000. These quality factors are combined with Fig. 5-4 to get the calculated FSBS gains. The measured FSBS gains agree well with the calculation. The maximal measured FSBS gain of $2322 m^{-1}W^{-1}$ is more than 1000 times larger than recent demonstration of FSBS gain in fibres [91]. The relatively flat gain spectra demonstrates efficient photon-phonon coupling over a wide frequency range.

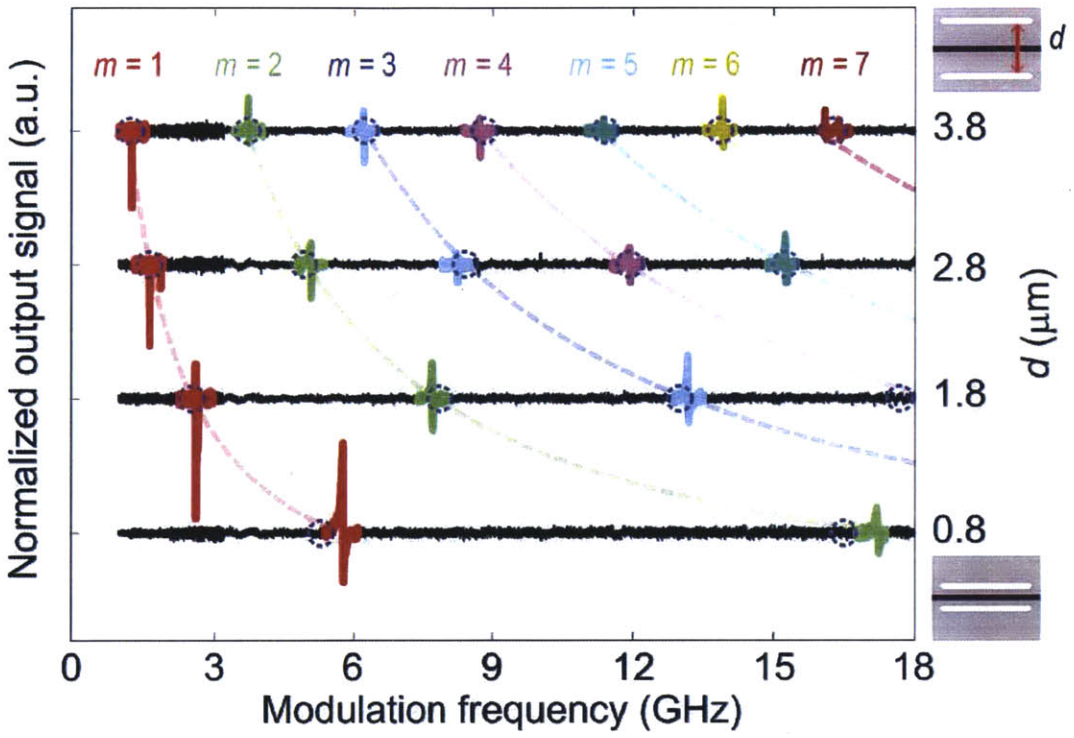

Figure 5-6: Elastic resonant frequencies for different d. The four horizontal curves are the measured nonlinear Brillouin spectra for waveguides with $d = [0.8,\ 1.8,\ 2.8,\ 3.8]\mu m$. The dashed lines are from finite element calculation as d varies continuously.

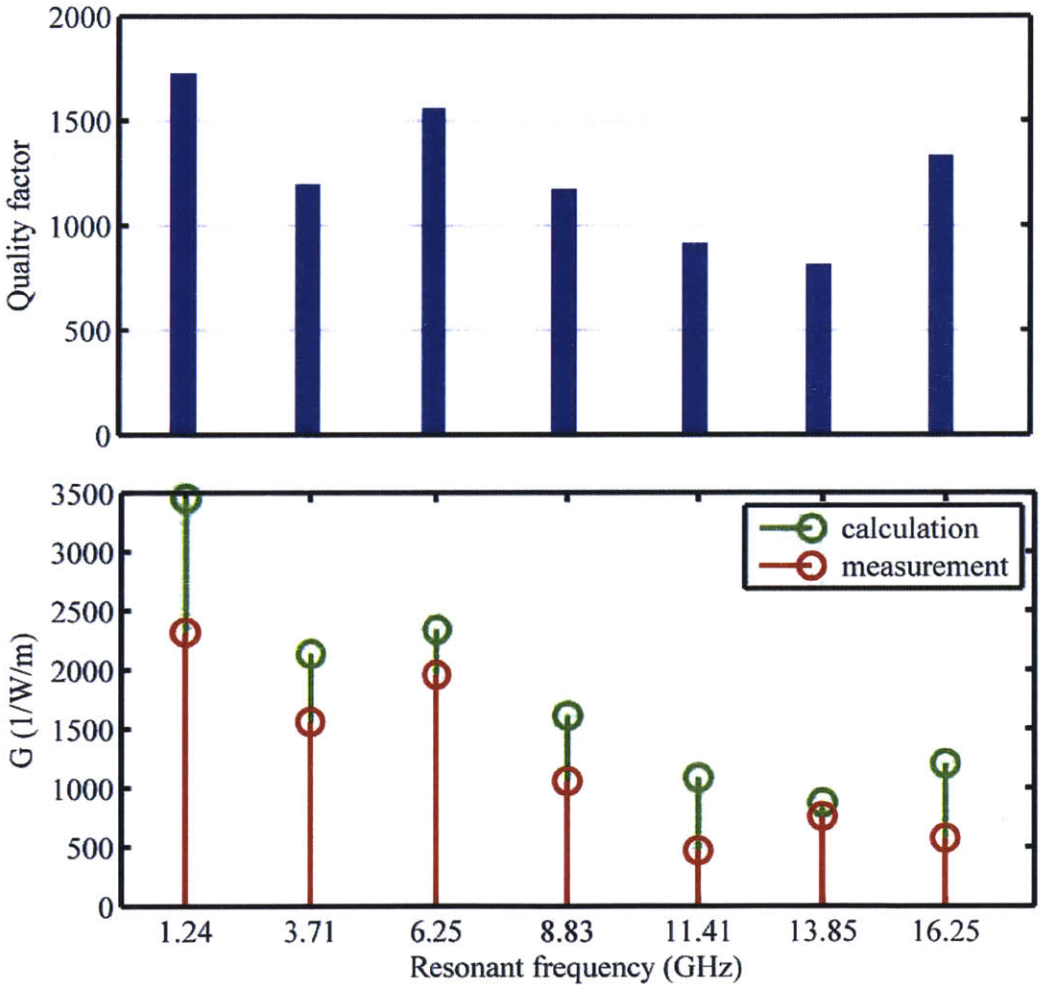

Figure 5-7: Measured and calculated FSBS gains of $d = 3.8\mu m$ waveguide. The top figure shows measured quality factors of different elastic modes. In the lower figure, the green dots correspond to the measured FSBS gains. The blue dots correspond to the calculated FSBS gains using the measured quality factor.

5.6 Concluding remarks

In this chapter, we proposed a novel class of hybrid photon-phonon waveguides. Numerical simulations reveal that such a structure has strong FSBS nonlinearities over a series of equally spaced transverse phonon modes spanning between 1 - 18GHz. The large FSBS gains are produced by the constructive combination of electrostrictive force and radiatoin pressure. Analysis of the measurement results on the real structures shows that these transverse phonon modes have consistently large mechanical quality factors (≈ 1000), creating a relatively flat gain spectrum over a wide frequency range. The integration of such hybrid photon-phonon waveguides with on-chip silicon photonics, MEMS, and CMOS could provide a host of new coherent signal processing schemes.

Chapter 6

Conclusion

In this thesis, we theoretically studied three nanophotonic phenomena which enable strong light-matter interaction.

We first propose an optimization based theoretical approach to tailor the optical response of multilayer silver/silica nanospheres over a wide frequency range. Our result shows that within silver/silica material systems, a simple bilayer structure with a silver shell is always optimal in providing the largest normalized cross-sections. Future directions include exploring other material systems and nonspherical geometries. For instance, J-aggregates with strong absorption peaks in visible spectrum can be coated to nanoparticles. The excitons in J-aggreates can couple to surface plasmon resnance to generate new peaks and transparency windows in visible spectrum. The calculation of optical cross-sections of nonspherical geometries will need new computational tools such as finite element method and boundary element method. Our approach can also be used to design nanoparticles for specific applications by constructing appropriate objective functions.

We next design a new class of optical circulators based on the directional coupling between one-way waveguide and two-way waveguide. In our implementation, the 1dB loss bandwidth for three-port and four-port circulators is found to be 2% and 1.3% respectively. The main factor that limits the bandwidth is the frequency dependent coupling coefficient in the asymmetric coupler. The bandwidth of such circulators can be further enhanced by making the coupling coefficient essentially frequency

independent through band structure engineering.

Next, we move to the field of traveling wave optomechanics via Stimulated Brillouin Scattering, and develop a general framework of calculating SBS gains via the overlap integral between optical and elastic eigen-modes. By applying this method to a silicon rectangular waveguide, we demonstrate how the method can be applied to forward SBS, backward SBS, and inter-mode coupling. By applying this method to a silicon periodic waveguide, we show that SBS gains can be furthered enhanced on Brillouin zone boundaries. One direction of future research is to study the dependence of SBS gains on waveguide materials. Another direction of future research is tailoring SBS gains through structural engineering. Our results on traveling wave optomechanics via SBS also have implications for the widely studied cavity optomechanics. In previous studies of cavity optomechanics, only radiation pressure is considered with the coupling coefficient expressed as a surface integral of radiation pressures. Our results indicate that electrostriction force should also be taken into account, and the coupling coefficient should be expressed as the integral of all optical forces.

Finally, we propose a novel class of hybrid photon-phonon waveguides. Numerical calculation and data analysis of realistic structures both reveal that such structure provides highly efficient and highly tailorable photon-phonon coupling over a wide frequency range. One direction of future research is to integrate other photonic/phononic elements into the membrane. For instance, we could put another parallel optical waveguide in the membrane so that the phonon activated by one optical waveguide can be picked up by the other optical waveguide. The coherent phonon emission extending in the entire membrane now becomes a new form of coherent information transduction. The hybridization of such Brillouin active structure with silicon photonics, CMOS, and MEMS could provide a host of new coherent signal processing schemes.

Bibliography

[1] Marin Soljačić and J. D. Joannopoulos. Enhancement of nonlinear effects using photonic crystals. *Nature Materials*, 3:211–219, 2004.

[2] Shuming Nie and Steven R. Emory. Probing single molecules and single nanoparticles by surface-enhanced raman scattering. 275:1102–1106, 1997.

[3] Prashant K. Jain, Kyeong Seok Lee, Ivan H. El-Sayed, and Mostafa A. El-Sayed. Calculated absorption and scattering properties of gold nanoparticles of different size, shape, and composition: Applications in biological imaging and biomedicine. *J. Phys. Chem. B*, 110:7238–7248, 2006.

[4] Zheng Wang, Y. D. Chong, John D. Joannopoulos, and Marin Soljačić. Reflection-free one-way edge modes in a gyromagnetic photonic crystal. *Phys. Rev. Lett.*, 100:013905, 2008.

[5] R. Boyd. *Nonlinear Optics.* Academic Press, 3rd edition, 2009.

[6] G. Agrawal. *Nonlinear Fiber Optics.* Academic Press, 4th edition, 2006.

[7] Ye Pu, Rachel Grange, Chia-Lung Hsieh, and Demetri Psaltis. Nonlinear optical properties of core-shell nanocavities for enhanced second-harmonic generation. *Phys. Rev. Lett.*, 104:207402, 2010.

[8] Xiaohua Huang, Svetlana Neretina, and Mostafa A. El-Sayed. Gold nanorods: From synthesis and properties to biological and biomedical applications. *Adv. Mater.*, 21:4880–4910, 2009.

[9] Cecilia Noguez. Surface plasmons on metal nanoparticles: the influence of shape and physical environment. *J. Phys. Chem. C*, 111:3806–3819, 2007.

[10] S. Alyones, C.W. Bruce, and A.K. Buin. Numerical methods for solving the problem of electromagnetic scattering by a thin finite conducting wire. *IEEE Trans. Antennas Propag.*, 55:1856–1861, 2007.

[11] Charles W. Bruce and Sharhabeel Alyones. Extinction efficiencies for metallic fibers in the infrared. *Appl. Opt.*, 48:5095–5098, 2009.

[12] Jian Zhu, J. Li, and J. Zhao. Tuning the wavelength drift between resonance light absorption and scattering of plasmonic nanoparticle. *Appl. Phys. lett.*, 99:101901, 2011.

[13] Carlos E. Román-Velázquez and Cecilia Noguez. Designing the plasmonic response of shell nanoparticles: Spectral representation. *J. Chem. Phys.*, 134:044116, 2011.

[14] S.J Oldenburg, R.D Averitt, S.L Westcott, and N.J Halas. Nanoengineering of optical resonances. *Chem. Phys. Lett.*, 288:243 – 247, 1998.

[15] E. Prodan and P. Nordlander. Structural tunability of the plasmon resonances in metallic nanoshells. *Nano Lett.*, 3:543–547, 2003.

[16] E. Prodan, C. Radloff, N. J. Halas, and P. Nordlander. A hybridization model for the plasmon response of complex nanostructures. *Science*, 302:419–422, 2003.

[17] Rizia Bardhan, Nathaniel K. Grady, Tamer Ali, and Naomi J. Halas. Metallic nanoshells with semiconductor cores: Optical characteristics modified by core medium properties. *ACS Nano*, 4:6169–6179, 2010.

[18] Rizia Bardhan, Shaunak Mukherjee, Nikolay A. Mirin, Stephen D. Levit, Peter Nordlander, and Naomi J. Halas. Nanosphere-in-a-nanoshell: A simple nanomatryushka. *J. Phys. Chem. C*, 114:7378–7383, 2010.

[19] Rafif E. Hamam, Aristeidis Karalis, J. D. Joannopoulos, and Marin Soljačić. Coupled-mode theory for general free-space resonant scattering of waves. *Phys. Rev. A*, 75:053801, 2007.

[20] Zhichao Ruan and Shanhui Fan. Superscattering of light from subwavelength nanostructures. *Phys. Rev. Lett.*, 105:013901, 2010.

[21] Zhichao Ruan and Shanhui Fan. Temporal coupled-mode theory for fano resonance in light scattering by a single obstacle. *J. Phys. Chem. C*, 114:7324–7329, 2010.

[22] Zhichao Ruan and Shanhui Fan. Design of subwavelength superscattering nanospheres. *Appl. Phys. lett.*, 98:043101, 2011.

[23] H. C. van de Hulst. *Light Scattering by Small Particles.* Dover, 1981.

[24] Craig Bohren and Donald Huffman. *Absorption and Scattering of Light by Small Particles.* John Wiley & Songs, 1983.

[25] E. D. Palik. *Handbook of Optical Constants of Solids.* Academic Press, New York, 1985.

[26] S. G. Johnson. The nlopt nonlinear optimization package, http://ab-initio.mit.edu/nlopt.

[27] Sergei Kucherenko and Yury Sytsko. Application of deterministic low-discrepancy sequences in global optimization. *Comput. Optim. Appl.*, 30:297–318, 2005.

[28] M. J. D. Powell. The bobyqa algorithm for bound constrained optimization without derivatives. Technical report, Department of Applied Mathematics and Theoretical Physics, Cambridge England, 2009.

[29] Nche T. Fofang, Tae-Ho Park, Oara Neumann, Nikolay A. Mirin, Peter Nordlander, and Naomi J. Halas. Plexcitonic nanoparticles: Plasmonexciton coupling in nanoshell j-aggregate complexes. *Nano Lett.*, 8:3481–3487, 2008.

[30] Akihito Yoshida and Noritsugu Kometani. Effect of the interaction between molecular exciton and localized surface plasmon on the spectroscopic properties of silver nanoparticles coated with cyanine dye j-aggregates. *J. Chem. Phys. C*, 114:2867–2872, 2010.

[31] Vladimir S Lebedev, A S Medvedev, D N Vasil'ev, D A Chubich, and Alexey G Vitukhnovsky. Optical properties of noble-metal nanoparticles coated with a dye j-aggregate monolayer. *Quantum Electron.*, 40:246–248, 2010.

[32] R J Potton. Reciprocity in optics. *Reports on Progress in Physics*, 67:717, 2004.

[33] Hiroyuki Takeda and Sajeev John. Compact optical one-way waveguide isolators for photonic-band-gap microchips. *Phys. Rev. A*, 78:023804, 2008.

[34] Alexander B. Khanikaev, Alexander V. Baryshev, Mitsuteru Inoue, and Yuri S. Kivshar. One-way electromagnetic tamm states in magnetophotonic structures. *Applied Physics Letters*, 95:011101, 2009.

[35] Alexander B. Khanikaev, S. Hossein Mousavi, Gennady Shvets, and Yuri S. Kivshar. One-way extraordinary optical transmission and nonreciprocal spoof plasmons. *Phys. Rev. Lett.*, 105:126804, 2010.

[36] Dirk Jalas, Alexander Petrov, Michael Krause, Jan Hampe, and Manfred Eich. Resonance splitting in gyrotropic ring resonators. *Opt. Lett.*, 35:3438–3440, 2010.

[37] Jesse Zheng. Optical frequency-modulated continuous-wave interferometers. *Appl. Opt.*, 45:2723–2730, 2006.

[38] Mitsuteru Inoue, Ken'ichi Arai, Toshitaka Fujii, and Masanori Abe. Magneto-optical properties of one-dimensional photonic crystals composed of magnetic and dielectric layers. *Journal of Applied Physics*, 83:6768–6770, 1998.

[39] M. Levy, I. Ilic, R. Scarmozzino, Jr. Osgood, R.M., R. Wolfe, C.J. Gutierrez, and G.A. Prinz. Thin-film-magnet magnetooptic waveguide isolator. *Photonics Technology Letters, IEEE*, 5:198 –200, 1993.

[40] Z. Wang and S. Fan. Magneto-optical defects in two-dimensional photonic crystals. *Applied Physics B: Lasers and Optics*, 81:369–375, 2005.

[41] Zheng Wang and Shanhui Fan. Optical circulators in two-dimensional magneto-optical photonic crystals. *Opt. Lett.*, 30:1989–1991, 2005.

[42] Zheng Wang and Shanhui Fan. Suppressing the effect of disorders using time-reversal symmetry breaking in magneto-optical photonic crystals: An illustration with a four-port circulator. *Photonics and Nanostructures - Fundamentals and Applications*, 4:132 – 140, 2006.

[43] Wojciech Śmigaj, Javier Romero-Vivas, Boris Gralak, Liubov Magdenko, Béatrice Dagens, and Mathias Vanwolleghem. Magneto-optical circulator designed for operation in a uniform external magnetic field. *Opt. Lett.*, 35:568–570, Feb 2010.

[44] Haibin Zhu and Chun Jiang. Optical isolation based on nonreciprocal micro-ring resonator. *Lightwave Technology, Journal of*, 29:1647 –1651, 2011.

[45] Kazuo Yayoi, Kazuma Tobinaga, Yusuke Kaneko, Alexander V. Baryshev, and Mitsuteru Inoue. Optical waveguide circulators based on two-dimensional magnetophotonic crystals: Numerical simulation for structure simplification and experimental verification. *Journal of Applied Physics*, 109:07B750, 2011.

[46] E. A. Ohm. A broad-band microwave circulator. *Microwave Theory and Techniques, IRE Transactions on*, 4:210–217, 1956.

[47] J. Helszajn. *Nonreciprocal Microwave Junctions and Circulators.* Wiley, 1975.

[48] Manfred Lohmeyer, Mikhail Shamonin, and Peter Hertel. Integrated optical circulator based on radiatively coupled magneto-optic waveguides. *Optical Engineering*, 36:889–895, 1997.

[49] N. Sugimoto, T. Shintaku, A. Tate, H. Terui, M. Shimokozono, E. Kubota, M. Ishii, and Y. Inoue. Waveguide polarization-independent optical circulator. *Photonics Technology Letters, IEEE*, 11:355 –357, 1999.

[50] Junichiro Fujita, Reinald Gerhardt, and Louay A. Eldada. Hybrid-integrated optical isolators and circulators. *Optoelectronic Interconnects, Integrated Circuits, and Packaging*, 4652:77–85, 2002.

[51] N. Hanashima, K. Hata, R. Mochida, T. Oikawa, T. Kineri, Y. Satoh, and S. Iwatsuka. Hybrid optical circulator using garnet-quartz composite embedded in planar waveguides. *Photonics Technology Letters, IEEE*, 16:2269 –2271, 2004.

[52] D. M. Pozar. *Ferrite Circulators.* John Wiley, 2005.

[53] F. D. M. Haldane and S. Raghu. Possible realization of directional optical waveguides in photonic crystals with broken time-reversal symmetry. *Phys. Rev. Lett.*, 100:013904, 2008.

[54] Zongfu Yu, Georgios Veronis, Zheng Wang, and Shanhui Fan. One-way electromagnetic waveguide formed at the interface between a plasmonic metal under a static magnetic field and a photonic crystal. *Phys. Rev. Lett.*, 100:023902, 2008.

[55] J. D. Joannopoulos Z. Wang, Y. D. Chong and Marin Soljačić. Observation of unidirectional backscattering-immune topological electromagnetic states. *Nature*, 461:772–775, 2009.

[56] Qiong Wang, Zhengbiao Ouyang, and Qiang Liu. Multiport photonic crystal circulators created by cascading magneto-optical cavities. *J. Opt. Soc. Am. B*, 28:703–708, 2011.

[57] K. W. Chiu and J. J. Quinn. Magnetoplasma surface waves in polar semiconductors: Retardation effects. *Phys. Rev. Lett.*, 29:600–603, 1972.

[58] R. F. Wallis, J. J. Brion, E. Burstein, and A. Hartstein. Theory of surface polaritons in anisotropic dielectric media with application to surface magnetoplasmons in semiconductors. *Phys. Rev. B*, 9:3424–3437, 1974.

[59] Yin Poo, Rui-xin Wu, Zhifang Lin, Yan Yang, and C. T. Chan. Experimental realization of self-guiding unidirectional electromagnetic edge states. *Phys. Rev. Lett.*, 106:093903, 2011.

[60] A. Yariv. Coupled-mode theory for guided-wave optics. *IEEE J. Quantum Electron*, 9:919–933, 1973.

[61] H. A. Haus. *Waves and Fields In Optoelectronics.* Prentice-Hall, 1984.

[62] Iris Crassee, Julien Levallois, Andrew Walter, Markus Ostler, Aaron Bostwick, Eli Rotenberg, Thomas Seyller, Dirk Marel, and Alexey Kuzmenko. Giant faraday rotation in single and multilayer graphene. *Nature Physics*, 4:48–51, 2011.

[63] Marinko Jablan, Hrvoje Buljan, and Marin Soljačić. Plasmonics in graphene at infrared frequencies. *Phys. Rev. B*, 80:245435, 2009.

[64] R. Y. Chiao, C. H. Townes, and B. P. Stoicheff. Stimulated brillouin scattering and coherent generation of intense hypersonic waves. *Phys. Rev. Lett.*, 12:592–595, 1964.

[65] P. Dainese, P. Russell, N. Joly, J. Knight, G. Wiederhecker, H. Fragnito, V. Laude, and A. Khelif. Stimulated brillouin scattering from multi-ghz-guided acoustic phonons in nanostructured photonic crystal fibres. *Nature Phys.*, 2:388–392, 2006.

[66] Andrey Kobyakov, Michael Sauer, and Dipak Chowdhury. Stimulated brillouin scattering in optical fibers. *Adv. Opt. Photon.*, 2:1–59, 2010.

[67] M. S. Kang, A. Nazarkin, A. Brenn, and P. St. J. Russell. Tightly trapped acoustic phonons in photonic crystal fibres as highly nonlinear artificial raman oscillators. *Nature Phys.*, 5:276–280, 2009.

[68] Ravi Pant, Christopher G. Poulton, Duk-Yong Choi, Hannah Mcfarlane, Samuel Hile, Enbang Li, Luc Thevenaz, Barry Luther-Davies, Stephen J. Madden, and Benjamin J. Eggleton. On-chip stimulated brillouin scattering. *Opt. Express*, 19:8285–8290, 2011.

[69] Kwang Yong Song, Miguel Herráez, and Luc Thévenaz. Observation of pulse delaying and advancement in optical fibers using stimulated brillouin scattering. *Opt. Express*, 13:82–88, 2005.

[70] Kwang Yong Song, Kazi S. Abedin, Kazuo Hotate, Miguel González Herráez, and Luc Thévenaz. Highly efficient brillouin slow and fast light using as2se3 chalcogenide fiber. *Opt. Express*, 14:5860–5865, 2006.

[71] Yoshitomo Okawachi, Matthew S. Bigelow, Jay E. Sharping, Zhaoming Zhu, Aaron Schweinsberg, Daniel J. Gauthier, Robert W. Boyd, and Alexander L. Gaeta. Tunable all-optical delays via brillouin slow light in an optical fiber. *Phys. Rev. Lett.*, 94:153902, Apr 2005.

[72] Ravi Pant, Michael D. Stenner, Mark A. Neifeld, and Daniel J. Gauthier. Optimal pump profile designs for broadband sbs slow-light systems. *Opt. Express*, 16:2764–2777, 2008.

[73] Matthew Tomes and Tal Carmon. Photonic micro-electromechanical systems vibrating at x-band (11-ghz) rates. *Phys. Rev. Lett.*, 102:113601, Mar 2009.

[74] Zhaoming Zhu, Daniel J. Gauthier, and Robert W. Boyd. Stored light in an optical fiber via stimulated brillouin scattering. *Science*, 318(5857):1748–1750, 2007.

[75] Peter T. Rakich, Paul Davids, and Zheng Wang. Tailoring optical forces in waveguides through radiation pressure and electrostrictive forces. *Opt. Express*, 18:14439–14453, 2010.

[76] Peter T. Rakich, Charles Reinke, Ryan Camacho, Paul Davids, and Zheng Wang. Giant enhancement of stimulated brillouin scattering in the subwavelength limit. *Phys. Rev. X*, 2:011008, 2012.

[77] Michelle L. Povinelli, Marko Loncar, Mihai Ibanescu, Elizabeth J. Smythe, Steven G. Johnson, Federico Capasso, and John D. Joannopoulos. Evanescent-wave bonding between optical waveguides. *Opt. Lett.*, 30:3042–3044, 2005.

[78] Peter T. Rakich, Zheng Wang, and Paul Davids. Scaling of optical forces in dielectric waveguides: rigorous connection between radiation pressure and dispersion. *Opt. Lett.*, 36:217–219, 2011.

[79] T. J. Kippenberg and K. J. Vahala. Cavity optomechanics: Back-action at the mesoscale. *Science*, 321(5893):1172–1176, 2008.

[80] Matt Eichenfield, Christopher P. Michael, Raviv Perahia, and Oskar Painter. Actuation of micro-optomechanical systems via cavity-enhanced optical dipole forces. *Nature Photonics*, 1:416–422, 2007.

[81] Matt Eichenfield, Jasper Chan, Amir H. Safavi-Naeini, Kerry J. Vahala, and Oskar Painter. Modeling dispersive coupling andlosses of localized optical andmechanical modes in optomechanicalcrystals. *Opt. Express*, 17:20078–20098, 2009.

[82] Peter T. Rakich, Milo A. Popovi, Marin Soljačić, and Erich P. Ippen. Trapping, corralling and spectral bonding of optical resonances through optically induced potentials. *Nature Photonics*, 1:658–665, 2007.

[83] Mo Li, W. H. P. Pernice, and H. X. Tang. Tunable bipolar optical interactions between guided lightwaves. *Nature Photonics*, 3:464–468, 2009.

[84] Joris Roels, Iwijn De Vlaminck, Liesbet Lagae, Bjorn Maes, Dries Van Thourhout, and Roel Baets. Tunable optical forces between nanophotonic waveguides. *Nature Nanotechnology*, 4:510–513, 2009.

[85] M. S. Kang, A. Brenn, and P. St.J. Russell. All-optical control of gigahertz acoustic resonances by forward stimulated interpolarization scattering in a photonic crystal fiber. *Phys. Rev. Lett.*, 105:153901, 2010.

[86] Gaurav Bahl, Matthew Tomes, Florian Marquardt, and Tal Carmon. Observation of spontaneous brillouin cooling. *Nature Phys.*, 8:203–207, 2012.

[87] Zongfu Yu and Shanhui Fan. Complete optical isolation created by indirect interband photonic transitions. *Nature Photonics*, 3:91–94, 2008.

[88] Xinpeng Huang and Shanhui Fan. Complete all-optical silica fiber isolator via stimulated brillouin scattering. *J. Lightwave Technol.*, 29:2267–2275, 2011.

[89] M. S. Kang, A. Butsch, and P. St. J. Russell. Reconfigurable light-driven optoacoustic isolators in photonic crystal fibre. *Nature Photonics*, 5:549–553, 2011.

[90] J. Botineau, E. Picholle, and D. Bahloul. Effective stimulated brillouin gain in singlemode optical fibres. *Electronics Letters*, 31:2032 –2034, 1995.

[91] Jing Wang, Yunhui Zhu, Rui Zhang, and Daniel J. Gauthier. Fsbs resonances observed in a standard highly nonlinear fiber. *Opt. Express*, 19:5339–5349, 2011.

[92] Alan H. McCurdy. Modeling of stimulated brillouin scattering in optical fibers with arbitrary radial index profile. *J. Lightwave Technol.*, 23:3509, 2005.

[93] D. Royer and E. Dieulesaint. *Elastic Wvaes in Solids I: Free and Guided Propagation.* Springer, 2000.

[94] S.A. Chandorkar, M. Agarwal, R. Melamud, R.N. Candler, K.E. Goodson, and T.W. Kenny. Limits of quality factor in bulk-mode micromechanical resonators. In *Micro Electro Mechanical Systems, 2008. MEMS 2008. IEEE 21st International Conference on*, pages 74 –77, jan. 2008.

[95] E. Dieulesaint and D. Royer. *Elastic Wvaes in Solids II: Generation, Acousto-Optic Interaction, Applications.* Springer, 2000.

[96] James P. Gordon. Radiation forces and momenta in dielectric media. *Phys. Rev. A*, 8:14–21, Jul 1973.

[97] Steven G. Johnson, M. Ibanescu, M. A. Skorobogatiy, O. Weisberg, J. D. Joannopoulos, and Y. Fink. Perturbation theory for maxwell's equations with shifting material boundaries. *Phys. Rev. E*, 65:066611, Jun 2002.

[98] L. S. Hounsome, R. Jones, M. J. Shaw, and P. R. Briddon. Photoelastic constants in diamond and silicon. *physica status solidi A*, 203:3088–3093, 2006.

[99] M. J. Damzen and M. H. R. Hutchinson. High-efficiency laser-pulse compression by stimulated brillouin scattering. *Opt. Lett.*, 8:313–315, 1983.

[100] Thomas Schneider, Markus Junker, and Kai-Uwe Lauterbach. Theoretical and experimental investigation of brillouin scattering for the generation of millimeter waves. *J. Opt. Soc. Am. B*, 23:1012–1019, 2006.

[101] Danielle Braje, Leo Hollberg, and Scott Diddams. Brillouin-enhanced hyperparametric generation of an optical frequency comb in a monolithic highly nonlinear fiber cavity pumped by a cw laser. *Phys. Rev. Lett.*, 102:193902, 2009.

[102] Taiji Sakamoto, Takashi Yamamoto, Kazuyuki Shiraki, and Toshio Kurashima. Low distortion slow light in flat brillouin gain spectrum by using optical frequency comb. *Opt. Express*, 16:8026–8032, 2008.

[103] Takuo Tanemura, Yuichi Takushima, and Kazuro Kikuchi. Narrowband optical filter, with a variable transmission spectrum, using stimulated brillouin scattering in optical fiber. *Opt. Lett.*, 27:1552–1554, 2002.

[104] Blake C. Rodgers, Timothy H. Russell, and Won B. Roh. Laser beam combining and cleanup by stimulated brillouin scattering in a multimode optical fiber. *Opt. Lett.*, 24:1124–1126, 1999.

[105] Shahraam Afshar V. and Tanya M. Monro. A full vectorial model for pulse propagation in emerging waveguides with subwavelength structures part i: Kerr nonlinearity. *Opt. Express*, 17:2298–2318, 2009.